

FABRICATION AND PROPERTIES OF NANOSCALE MULTIFERROIC  
HETEROSTRUCTURES FOR APPLICATION IN  
MAGNETO-ELECTRIC RANDOM ACCESS MEMORY (MERAM) DEVICES

by

GUNWOO KIM

ARUNAVA GUPTA, COMMITTEE CHAIR

ROBERT W. SCHARSTEIN  
JEFF JACKSON  
SUSHMA KOTRU  
GREGORY B. THOMPSON

A DISSERTATION

Submitted in partial fulfillment of the requirements  
for the degree of Doctor of Philosophy  
in the Department of Electrical and Computer Engineering  
in the Graduate School of  
The University of Alabama

TUSCALOOSA, ALABAMA

2012

Copyright Gunwoo Kim 2012  
ALL RIGHTS RESERVED

## ABSTRACT

Magnetoelectric random access memory (MERAM) has emerged as a promising new class of non-volatile solid-state memory device. It offers nondestructive reading along with low power consumption during the write operation. A common implementation of MERAM involves use of multiferroic tunneling junctions (MFTJs), which besides offering non-volatility are both electrically and magnetically tunable. Fundamentally, a MFTJ consists of a heterostructure of an ultrathin multiferroic or ferroelectric material as the active tunneling barrier sandwiched between ferromagnetic electrodes. Thereby, the MFTJ exhibits both tunnel electroresistance (TER) and tunnel magnetoresistance (TMR) effects with application of an electric and magnetic field, respectively.

In this thesis work, we have developed two-dimensional (2D) thin-film multiferroic heterostructure METJ prototypes consisting of ultrathin ferroelectric  $\text{BaTiO}_3$  (BTO) layer and a conducting ferromagnetic  $\text{La}_{0.67}\text{Sr}_{0.33}\text{MnO}_3$  (LSMO) electrode. The heteroepitaxial films are grown using the pulsed laser deposition (PLD) technique. This oxide heterostructure offers the opportunity to study the nano-scale details of the tunnel electroresistance (TER) effect using scanning probe microscopy techniques. We performed the measurements using the MFP-3D (Asylum Research) scanning probe microscope. The ultrathin BTO films (1.2 – 2.0 nm) grown on LSMO electrodes display both ferro- and piezo-electric properties and exhibit large tunnel resistance effect.

We have explored the growth and properties of one-dimensional (1D) heterostructures,

referred to as multiferroic nanowire (NW) heterostructures. The ferromagnetic/ferroelectric composite heterostructures are grown as sheath layers using PLD on lattice-matched template NWs, e.g. MgO, that are deposited by chemical vapor deposition utilizing the vapor-liquid-solid (VLS) mechanism. The one-dimensional geometry can substantially overcome the clamping effect of the substrate present in two-dimensional structures because of the reduced volume of the template. This leads to minimum constraint of displacements at the interface and thereby significantly enhances the magnetoelectric (ME) effect. We characterized the nanostructures using scanning electron microscopy (SEM) and transmission electron microscopy (TEM).

The results of our studies utilizing multiferroic 2-D thin films and 1-D NW architectures clearly demonstrate the potential of these heterostructures for future device applications, such as in MERAM, data storage, magneto-electric field sensors, etc.

## DEDICATION

## SCRIPTURE

*His Strength*

*Isaiah 41:10*

*So do not fear, for I am with you,*

*do not be dismayed, for I am your God.*

*I will strengthen you and help you,*

*I will uphold you with my righteous right hand.*

## LIST OF ABBREVIATIONS AND SYMBOLS

$R_p$	Parallel magnetization
$R_{ap}$	Antiparallel magnetization
$\chi$	Magnetic susceptibility
$T_C$	Curie Temperature
$T_N$	Neel Temperature
K	Kelvin Temperature
$\vec{B}$	Magnetic induction
$\vec{H}$	Magnetic field
$\vec{E}$	Electric field
$M_r$	Remanent magnetic polarization
$P_r$	Remanent electric polarization
$M_s$	Saturation magnetic moment
$\alpha_E$	Magnetoelectric voltage coefficient
f.u	Formula unit
$\mu C$	micro Coulomb
$\psi$	Psi angle ranging from $0^\circ$ to $90^\circ$
$\phi$	Phi angle ranging from $0^\circ$ to $360^\circ$
$\lambda$	Wavelength of X-ray (Equal to 1.5405 Å for Cu K $\alpha$ X-ray)

$\mu_B$  Bohr magneton (Equal to  $0.927 \times 10^{-20}$  erg/Oe)

Torr Non-Si unit of pressure (760 Torr = 1 atmosphere)

## ACKNOWLEDGMENTS

I am heartily thankful to my advisor, Professor Arunava Gupta, whose wisdom, supervision and support from the preliminary to the concluding level enabled me to develop an understanding of the research subjects. When I experienced a serious medical issue, he had kept in touch with me and given me an opportunity to continue pursuing my Ph.D program. Without his encouragement, I would not have been able to complete my degree. I am sincerely grateful to my co-advisor Professor Robert W. Scharstein, for his guidance throughout my dissertation writing. I am truly thankful to my committee members, Professor Jackson, Professor Kotru and Professor Thompson. They truly prayed for my recovery and guided me to complete my degree with their invaluable support and input. I sincerely thank Professor Subhadra Gupta for her warm heartedness. I am also thankful to Professor Haskew for his prayers for my recovery. I am especially thankful to Professor Bruce Kim. He offered me an opportunity to seek the Ph.D degree program at The University of Alabama.

I would like to thank former and present group members; Dr. Prahallad Padhan, Dr. Dipanjan Mazumdar, Dr. Vilas Shelke, Dr. Ningzhong Bao, Dr Liming Zhen, Dr. Krishna Chetry, Dr. Yu-Hsiang A. Wang, Neha Pachauri and Mehmet Yurtisigi who gave me valuable help and support for my research. I am obliged to the staff at the Center for Materials for Information Technology (MINT). They gave me their endless support, love and prayers.

I also thank church members in Korean Presbyterian Church at Tuscaloosa. They stayed overnight with me at the hospital and prayed for my recovery.

I would also specially thank Professor Lee, Kyoo-Hyung at the Asan medical center in Korea. Without his medical care, I could not complete this degree program and even not able to be alive.

I am truly thankful to my parents for their endless love and care. My mother, KyungHa Kim, donated her bone marrow to her son and gave me life twice. My father, WonSik Kim, made many sacrifices to save his son.

Finally, I am truly and heartily thankful to my wife, Gimin Nam. Without the support of Gimin, I could not have survived and this work would never have been possible. She never stopped her sacrifice and encouraging me to persist. I love Gimin so much. I will be truly forever thankful to you. I am also thankful to my daughter, Christine Chae-Min Kim. She grew up without my support for a few years but she became a great child. I love you, Chae-Min.

Lastly, I thank God. He never gave me up when I had walked through the darkest valley and showed me His love through my salvation.

## CONTENTS

ABSTRACT .....	ii
DEDICATION .....	iv
LIST OF ABBREVIATIONS AND SYMBOLS .....	v
ACKNOWLEDGMENTS .....	vii
LIST OF TABLES .....	xii
LIST OF FIGURES .....	xiii
1. INTRODUCTION .....	1
2. LITERATURE REVIEW .....	7
2.1 Memory devices .....	7
2.1.1 Ferroelectric memory .....	7
2.1.2 Ferromagnetic memory .....	10
2.1.3 Magneto-Electric Random Access Memory (MERAM) .....	13
2.2 Multiferroic compositions .....	16
2.3 Multiferroic nanowires .....	21
3. FABRICATION AND CHARACTERIZATION TECHNIQUES AND REVIEW OF SELECTED MATERIALS .....	23
3.1 Fabrications .....	23
3.1.1 Pulsed laser Deposition (PLD) .....	23
3.1.2 Chemical Vapor Deposition (CVD) .....	24
3.1.3 Electron beam (E-beam) lithography .....	26

3.2 Characterizations .....	28
3.2.1 X-ray diffraction (XRD).....	28
3.2.2 Transmission electron microscopy (TEM).....	30
3.2.3 Piezoresponse force microscopy (PFM) .....	32
3.2.4 Conducting atomic force microscopy (C-AFM) .....	33
3.2.5 Other characterization methods.....	35
3.3 Review of selected materials .....	36
3.3.1 Barium titanate ( $\text{BaTiO}_3$ , BTO) .....	36
3.3.2 Nickel ferrite ( $\text{NiFe}_2\text{O}_4$ , NFO) .....	37
3.3.3 Lanthanum strontium manganite ( $\text{LaSrMnO}_3$ , LSMO) .....	39
<b>4. MAGNESIUM OXIDE (<math>\text{MgO}</math>) and MULTIFERROIC NANOWIRES (NWs).....</b>	<b>40</b>
4.1 Introduction .....	40
4.2 Random arrangement of NWs on $\text{MgO}$ and Si substrates.....	41
4.2.1 Morphologies.....	41
4.2.2 Histograms of $\text{MgO}$ NWs and gold nanoparticles .....	45
4.3 Systematic pattern array of $\text{MgO}$ NW on $\text{MgO}$ substrate .....	47
4.3.1 Square cross-section pattern.....	47
4.3.2 Single dot pattern.....	49
4.4 Multiferroic nanowires .....	53
4.4.1 Thin $\text{BaTiO}_3$ and $\text{NiFe}_2\text{O}_4$ films.....	55
4.4.2 Single phase $\text{BaTiO}_3$ or $\text{NiFe}_2\text{O}_4$ coated NWs .....	58
4.5 Summary .....	63

5. NANOSCALE ELECTRORESISTANCE PROPERTIES OF ALL-OXIDE MAGNETO-ELECTRIC TUNNEL JUNCTION WITH ULTRA-THIN BARIUM TITANATE BARRIER .....	64
5.1 Introduction .....	64
5.2 Experimental results and discussion.....	67
5.2.1 Piezoelectric properties of the ultrathin BaTiO <sub>3</sub> films.....	67
5.2.2 Conductive properties of the ultrathin BaTiO <sub>3</sub> films.....	71
5.3 Summary .....	79
6. CONCLUSION AND FUTURE WORK .....	80
7. REFERENCES .....	83
BIBLIOGRAPHY.....	89
APPENDIX A.....	90

## LIST OF TABLES

2.2.1 Multiferroic compositions.....	20
4.3.1 Tabulation of the absolute number and density of the grown nanowires at different patterned area, along with the number of gold catalyst particles formed at the growth temperature. (Reproduced with permission from ref. [81]).....	51
4.4.1 Lattice parameter ( $a$ ) and lattice mismatches (%) for each material.	53
5.1.1 Comparison of properties of three different conductive tips. ....	66
5.2.1 Theoretical values calculated by Brinkman equation fit using three different conductive tips. .....	78

## LIST OF FIGURES

2.1 (a) Perovskite structure of BaTiO <sub>3</sub> where a small cation (O) at the center of an octahedron of oxygen anions with large cations (Ba) at the unit cell corners, and (Ti <sup>4+</sup> ) metal ions placed at a center of the unit cell. (b) and (c) illustration of a transition phase after Ti <sup>4+</sup> movements, Up/Down. Typical hysteresis loop is shown between (b) and (c) (Adapted from ref. [3]). .....	8
2.2 Schematic of the principle concept of ferroelectric tunnel junction (FTJ) and three fundamental mechanisms (a-c) that can lead to electric tunnel resistance. (Reproduced with permission from ref. [32]) .....	9
2.3 Schematic illustration of density of states in different metal oxide materials. 3d and 4s densities in first-row transition metals and electron spin up and down densities of states. The horizontal lines indicate the Fermi levels in ferrite materials, Zn, Cu, Ni, Co, Fe, and Mn. (Adapted from ref. [37]) .....	11
2.4 Schematic illustrating principle of magnetoresistance (MR) due to the combination of electro spins. (a) Low resistance state with parallel spins direction of the two ferromagnetic layers. (b) High resistance state with anti-parallel spins direction of the two ferromagnetic layers.....	12
2.5 Two fundamental layer structures to configure MERAM. (a) Single FE layer is sandwiched by two FM layers. (b) Two FM layers are separated by a single-phase multiferroic with combined properties of ferroelectricity (FE) and ferromagnetism (FM)/antiferromagnetism (AFM). ....	14
2.6 Schematic of the layer structures of MERAM. (a) Two ferromagnetic layers (blue color) are aligned. Low or high resistance state owing to the magnetization configuration (parallel or antiparallel) of the ferromagnetic layers. (b) A bottom ferromagnetic layer is on the multiferroic layer. If magnetoelectric coupling (ME <sub>H</sub> ) is strong enough by the ferroelectric polarization in the multiferroic layer the electron spins rotates to reset the magnetization configuration change of the bottom ferromagnetic layer, resulting parallel to antiparallel combination of the two ferromagnetic electrodes (Reproduced with permission from ref. [13]).....	16

3.1.1 Schematic of a PLD system used in this study. It consists of a high vacuum-high vessel combined with a load lock and process chamber, a circular disk for rotating multiple targets, a load arm to insert a substrate into the process chamber, heating elements, gas delivery ports, optical lens and quartz window to guide Excimer laser beam into the process chamber.	24
3.1.2 Schematic of a typical CVD system for synthesizing nanowires (NWs). It consists of a quartz reaction tube, a furnace to provide required high temperature, gas inlet/outlet ports, precursor source and a substrate where NWs are grown.	25
3.1.3 Schematic diagram illustrating the growth sequence of MgO nanowires. The square gold regions are patterned using e-beam lithography. Gold nanoparticles are formed within the square region at a critical annealing temperature (925°C). Single free-standing MgO NWs are grown on the substrate with the gold particles being lifted up. Reproduced with permission from ref. [81])	26
3.1.4 Schematic illustrating the process of E-beam Lithography. Two kinds of patterning processes are described depending on properties of resists, positive and negative films as shown in case (I) and (II). As an initial preparation, E-beam resist is spin coated on silicon wafer as shown in the middle figure. (a) E-beam penetrates through the pattern mask. (b) Exposed resist changes chemical structure to become more soluble in the developer. (c) After developing, exposed region is removed in the case of positive resist and retained in the case of negative resist. (d) Thin gold film is deposited using e-beam evaporator. (e) After stripping to remove unexposed resist, final patterns with gold thin film remains.	27
3.2.1 Schematic diagram illustrating Bragg's law, where n is an integer, $\lambda$ is the wavelength of X-ray, d is the lattice spacing, and $\theta$ is the diffraction angle.	28
3.2.2 Theoretical method to determine the film thickness using X-ray reflectivity (XRR) technique. (a) Oscillation curves (b) Symbols indicate the calculated data points using Eq. (2). Linear fit is applied to determine the value of slope, providing the film thickness	29
3.2.3 Schematic providing a view of tilt and rotation angles for pole figure measurement. Here tilt, psi ( $\psi$ ) ranges from $0^\circ$ to $90^\circ$ , and rotation phi ( $\phi$ ), ranges from $0^\circ$ to $360^\circ$ . $\theta$ is an incident angle of X-ray beam with respect to substrate surface.....	30
3.2.4 Schematic of the TEM image modes. (a) Bright-field image mode, (b) Dark-field image mode. (Adapted from ref. [72])	32

3.2.5 Schematic of typical PFM measurement system. The phase deformation of a sample is occurred by biased initial tip scans. Then the AFM tip (dashed and solid) indicates the electromechanical displacement while scanning over the surface and visualizes the phase image through imaging processes. ....	33
3.2.6 Schematic diagram for conducting AFM measurement. A conductive tip senses the different conductivity and detects current while scanning the surface of a sample.....	34
3.2.7 Schematic of the basic configuration of a RHEED system. An incident electron beam at a shallow angle is diffracted from the sample surface and projects diffraction patterns on the screen. A sample is placed in an ultrahigh vacuum vessel and can be rotated 360 degrees, leading to various diffraction patterns owing to different crystal orientations.....	36
3.3.1 Schematic of BaTiO <sub>3</sub> (BTO) crystal structure. The BTO material is deformed from cubic to tetragonal structure by an application of an applied electric field at room temperature. .....	37
3.3.2 Schematic of inverse spinel NiFe <sub>2</sub> O <sub>4</sub> structure consisting of 'tetrahedral A' sites and 'octahedral B' sites. The cubic structure is configured by combining these two sites in a FCC oxygen lattice. (Adapted from ref. [37]). .....	38
4.2.1 (a) SEM images showing the growth of vertically aligned MgO nanowires on a (001)-oriented MgO substrate. The inset shows an image of the gold particles formed by heating the gold film on the MgO substrate to the growth temperature and then cooled down without actual growth of the nanowires. (b) SEM image showing MgO nanowires grown on a (001)-oriented Si substrate for a total deposition period of 60 minutes. The wires grow in random directions exhibiting a basket-weave-like morphology. The inset shows the gold particles formed by heating the gold film on the Si substrate to the growth temperature and then cooled down without actual growth of the nanowires. The marker for both inset images is 100 nm. (Reproduced with permission from ref. [81] .....	43
4.2.2 (a) TEM diffraction pattern and bright field image of a single MgO nanowire grown on the MgO substrate indicating (001) growth direction. (b) MgO nanowire showing a cubic-rod shape morphology; the image to the right has the cube edges highlighted. (c) TEM bright field image of a MgO nanowire with the gold catalyst on top, which has been grown on an MgO substrate. (d) TEM bright field image of MgO nanowires grown on Si substrate. Note the rectangular shape of the nanowires and interconnection of the wires to each other in different directions. This type of interconnection is not evident in the MgO nanowires grown on the	

MgO substrate. (Reproduced with permission from ref. [81]) .....	44
4.2.3 Histograms comparing the diameter of MgO nanowire grown on (a) MgO (001) and (b) Si (001) substrates. (Reproduced with permission from ref. [81]) .....	46
4.2.4 Histograms comparing the size of gold nanoparticles formed using a 1 nm thick gold film on (a) MgO (001) and (b) Si (001) substrates. (Reproduced with permission from ref. [81]) .....	48
4.3.1 SEM images showing different patterned regions of the MgO nanowires. The bright spot on the top of each nanowire is the gold catalyst particle. [(a) and (d)] $0.25\mu\text{m}^2$ , [(b) and (e)] $1\mu\text{m}^2$ , and [(c) and (f)] $4\mu\text{m}^2$ . A blanket gold film of 1 nm thickness is deposited and patterned using e-beam lithography for the selective growth of the nanowires. (Reproduced with permission from ref. [81]).....	50
4.3.2 Histogram of the size distribution of gold nanoparticles formed within the $1\mu\text{m}^2$ patterned regions on an MgO (001) substrate. The average nanoparticle size is 20 nm. (Reproduced with permission from ref. [81]).....	51
4.3.3 SEM images of a single MgO NW (a) Gold dot pattern in 10 x10 arrays. The diameter of dots is approximately 200 nm. (b) Single MgO NW grown within each dot array. The height is around 5-10 $\mu\text{m}$ . ....	52
4.4.1 Schematic of multiferroic nanowire. (a) Template MgO NWs produced by VLS growth mechanism in a typical CVD process. NWs are vertically oriented. (b)-(c) ‘core-shell’ type multiferroic nanowire consisting of ferrite (yellow)-ferroelectric (purple) thin film deposited on the template post of MgO NW by PLD technique. (d) Cross section view of the muliferroic nanowire .....	54
4.4.2 (a) $\theta$ - $2\theta$ X-ray diffraction spectra for a single-phase NFO and BTO film on MgO substrate. Peaks are close to the angular positions of the (004) and the (002) reflection of NFO and BTO. (b)-(c) Rocking curves for NFO and BTO films. The vertical solid lines indicate the bulk NFO and BTO $2\theta$ peak positions. Here, makers, *, ♦, and ♦, indicate MgO bulk peak, NFO and BTO film peaks. ....	55
4.4.3 Phi $\phi$ scans of (311) reflection of bilayers of NFO and BTO films on MgO. Four symmetric peaks spaced 90 degrees apart are observed. ....	56
4.4.4 RHEED patterns along [100] for epitaxial growth of BTO and NFO thin films on (100)-oriented MgO substrate. (a) RHEED image of MgO substrate prior to deposition. (b)-(c) RHEED image of BTO and NFO	

films.....	57
4.4.5 SEM images of nanowires. (a) Template MgO NWs. Gold balls lifted up and positioned on top of MgO NWs during a growth. (b) Single-phase BTO NWs. (c) Single-phase NFO NWs.....	59
4.4.6 TEM images of BaTiO <sub>3</sub> NWs. (a) Bright field TEM image showing single-BTO NW. Insert image shows a diffraction pattern, indicating well crystallized structure. (b) BTO NW has a cubic structure and <001> growth direction same as the template MgO. (c) HRTEM images displaying lattice spacing at the boundary of MgO and BTO layers. (d) EDS analysis indicates presence of Ba, Ti, Mg, and O .....	60
4.4.7 TEM images of NiFe <sub>2</sub> O <sub>4</sub> NWs. (a) Bright field TEM image showing single-NFO NW. Insert image shows a diffraction pattern, indicating well crystallized structure. (b) NFO NW has a cubic structure and <001> growth direction, same as the template MgO. (c) HRTEM image displaying lattice spacing of MgO and NFO layers. The lattice spacing's cannot be resolved because MgO and NFO are isostructural with very similar lattice parameters. (d) EDS analysis indicates presence of Ni, Fe, Mg, and O .....	62
5.2.1 AFM surface topology image of BTO film of thickness 2 nm. RMS roughness of the film is 0.2 nm.....	68
5.2.2 Schematic for generating polarization pattern (a) and a polarized image showing UA logo with an elephant (b). Black color zone is written using a tip voltage, V <sub>tip</sub> = - 3V and white color is zone is written using a tip voltage, V <sub>tip</sub> = + 3V. ....	69
5.2.3 Hysteresis loop corresponding to polarization switching of BTO film. (a) Phase map in degree and (b) amplitude map exhibiting a butterfly loop. ....	70
5.2.4 Schematic illustration for creating different polarization state regions. (a-1) 2μm × 2μm square zone poled by a negative voltage. (a-2) 1 μm × 1μm center region poled by a positive voltage. (a-3) is re-poled area by a positive voltage after 6 hours. (b) PFM image after initial polarization resulting from steps (a-1) and (a-2). (c) Re-read PFM image after step (a-3). ....	71
5.2.5 Schematic of configurations for polarization orientation. (a) Polarization pointing upward by application of a positive sample bias. (b) Current map while scanning the region. (c) Polarization pointing downward by application of a negative sample bias. (d) Current map while scanning the same region. For the measurements the tip is grounded and	

the current is measured using an amplifier. ....	73
5.2.6 I-V curves measured with different polarization states, upward or downward, corresponding to switch 'ON' or 'OFF' state. The black lines represent I-V curves fits using the Brinkman model. Insert shows the TER and ON/OFF ratio. ....	74
5.2.7 I-V curves and TER values measured by DPER 18 (a)-(b), and PtSi (c)-(d) commercial tips at different polarization states, upward or downward, corresponding to switch 'ON' or 'OFF' state. ....	76
5.2.8 Comparison of barrier heights of polarization ON and OFF states due to applied different commercial tips. ....	78
Appendix A1 SEM images of four point contact pads fabricated by using E-beam lithography. (a) First designed pads where four legs are clearly patterned. (b) Secondly designed pads where single NW is successfully placed on the four legs. ....	91

## CHAPTER 1

### INTRODUCTION

Ferroelectric and ferromagnetic oxide materials have been used in a wide range of applications such as sensors, transducers, microwave components, and data storage [1, 2]. Among these applications, ferroelectric random access memory (FRAM) [3] and magnetic random access memory (MRAM) [4] have received a great deal of attention as an alternative to traditional semiconductor-based memory (RAM). These types of memory are capable of non-volatility arising from spontaneous and switchable polarization or magnetization. FRAM offers fast access speed (~5 ns) and lower power consumption, while MRAM has very good data access speed and endurance. As a tradeoff, data destruction in the readout process is a drawback for FRAM because of the displacement current, and writing energy for magnetization switching is a handicap of MRAM [5]. These weaknesses ultimately limit the performance of the memory devices. Therefore, a new type of the memory device is required to provide nondestructive reading and low power consumption in write operations. Multiferroic memory has recently emerged as a potential device because it meets these requirements.

The term “multiferroic” was first used by H. Schmid in 1994 to denote the exhibition of two or more ferroic order parameters, which are ferroelectricity, ferromagnetism, and ferroelasticity in the same phase [6]. A multiferroic material was originally discovered by Röntgen [7], who reported that a moving dielectric became magnetized when placed in an electric field and reverse-polarized in a magnetic field. Debye called this phenomenon the magnetoelectric (ME) effect [8, 9].

The ME effect is achieved by the combination of two different control mechanisms as represented in the symbolic relationships [10]

$$ME_E \text{ effect} = \frac{\text{electric}}{\text{mechanical}} \times \frac{\text{mechanical}}{\text{magnetic}}$$

$$ME_H \text{ effect} = \frac{\text{magnetic}}{\text{mechanical}} \times \frac{\text{mechanical}}{\text{electric}}.$$

In  $ME_E$ , magnetization is controlled by the electric field [11]; when an electric field is applied to a multiferroic composite, the piezoelectric phase changes its direction of electrical polarization resulting in mechanical deformation. It is then transferred to the magnetic phase, producing magnetization. In  $ME_H$ , it is the reversed effect; electric polarization results from a magnetic field [12].

Multiferroic random access memory (MERAM) using the  $ME_E$  control method has been proposed [13] as a novel technique for the practical application of ME effect. This type of memory operates via the combination of electromagnetic polarization and tunneling at an interface between a ferroelectric and ferromagnetic/anti-ferromagnetic film, which provide a multiferroic composite. The memory device writes and reads information bits by using the combination of ferroelectric tunnel junction (FTJ) and magnetic tunnel junction (MTJ) [14], respectively. The FTJ provides low power consumption and high data access speed and MTJ offers nondestructive reading operations in spintronics [15]. Spintronics exploits the phenomenon of magnetoresistance (MR) [16] rather than magnetic induction ( $\vec{B}$ ) for spin rotations owing to scaling down in device areas.

Although MERAM promises a new route to memory devices, practical fabrication of the device remains at an early stage because of technical obstacles. The development of ultrathin

ferroic tunnel barriers, which have stable and switchable polarization for writing information bits at room temperature, is especially challenging because of the disappearance of the ferroic properties below a critical thickness [17]. A few groups have reported that ultrathin ferroelectric films act as tunnel barriers as a key configuration of ferroelectric tunnel junctions (FTJ) in a small number of unit cells [18, 19, 20].

Fabricating multiferroic composites in one dimension (1-D) geometry, which makes it possible to scale down to nanometer size device, presents another challenging obstacle. The geometry may resolve a drawback of two-dimensional (2-D) geometry, which has a large in-plane constraint on clamping condition at the substrate, resulting in poor ME response [21]. It is necessary to configure the low dimensional multiferroic using nano materials such as nanowires/tubes in order to pursue the alternative geometry, but these structures have not yet been realized because of their complexity and technical difficulty in preparation. These challenges require better methods of state-of-the-art multiferroic architecture for new memory devices or other multifunctional applications characterized by the unique properties of multiferroics.

This study has two major objectives. First, we studied a low dimensional multiferroic, which is also referred to as one-dimensional (1-D) heterostructure multiferroic nanowire. This type of geometry would overcome the clamping condition exhibited in 2-D geometry because a reduced volume is expected, leading to minimum constraint at the interface of the films and substrate. Initially, we were strongly motivated by a report of Petrov et al. [22], who presented a theoretical model comparing the ME voltage coefficient for three different geometries: 2-D thin film, nanopillar, and nanowire (NW). They found that a NW structure displays a higher ME voltage coefficient than 2-D thin films because of the reduced volume of the 1-D template

substrate, minimizing the surface-clamping effect at the interface. The NW structures acting primarily as low dimensional elements have gained much attention because of their unique properties. Flexibility and preferable geometry give rise to nano scale devices, logic circuits, and bio-chemical (or medical) sensors [23, 24]. Functional NWs consisting of ferroelectric or ferrite material have also attracted interest because of the polarization/magnetization behavior that offers switchable device applications in memory and sensors controlled by electric and/or magnetic fields [25]. For these reasons, one-dimensional multiferroic NW structures offer opportunities to explore a wide range of applications in nano science.

Secondly, by taking advantage of coupled multiferroic layer architecture [26], which relaxes the composition limitations of material selection by combining ferroelectric/piezoelectric and ferromagnetic materials with a large magnetostriction, we developed coupled multiferroic composites composed of barium titanate ( $\text{BaTiO}_3$ , BTO) and lanthanum manganese ferrite ( $\text{La}_{0.67}\text{Sr}_{0.33}\text{MnO}_3$ , LSMO). These coupled multiferroic composites enabled us to study magnetoelectric tunnel junctions (METJ), [27] combined tunneling magnetoresistance and tunnel electroresistance (TMR-TER). The principal idea comes from tunnel resistance, which is configured in a ferromagnetism (FM)/spacer/ferromagnetism (FM) sandwich structure. Two FM films separated by a spacer layer can lead to magnetoresistance (MR) effect because of a resistance difference between parallel and antiparallel configuration of magnetization. The spacer is an insulator material that serves as a barrier layer. In this study, we selected a BTO ultrathin film because it is widely used as a ferroelectric and piezoelectric material and is a good candidate as a junction barrier, consistent with the principle of ferroelectric tunnel junction (FTJ). We characterized the ultrathin BTO films using scanning probe microscopy to investigate the property of the tunnel barrier and characterize the ferroelectric and piezoelectric properties.

Based on the results of these characterizations, we propose that a novel oxide multiferroic ultrathin film of BTO deposited on ferromagnetic LSMO will be suitable to design novel prototype devices for a wide range of applications, including MERAM, data storage, and magneto-electric field sensors.

To pursue these two objectives, we combined chemical vapor deposition (CVD) and pulsed laser deposition (PLD) techniques to synthesize magnesium oxide (MgO) nanowires as template posts and deposit sheath layers, coupling ferroic thin films onto the nanowires in a core-shell structure [28] to form 1-D structure configuration. Methods of characterization included microscopic images, crystallinity, and histogram of nanowires using scanning electron microscopy (SEM) and transmission electron microscopy (TEM). Based on these results, we propose that the synthesis method is applicable for forming multiferroic nanowires heterostructures.

We designed four-point contact pads using electron beam (e-beam) lithography and placed a single nanowire onto this structure, allowing the measurement of current (resistance) changes of single multiferroic nanowire as a function of externally applied magnetic field. The detail is described in an appendix.

We also used the PLD technique to grow bilayers of ultrathin films, which were then characterized in terms of their crystallinity. Local ferroelectric properties were studied using piezoresponse force microscopy (PFM) and conducting atomic force microscopy (C-AFM) for phase deformation and current-voltage ( $I$ - $V$ ) characteristics of ultrathin ferroelectric films.

This dissertation is divided into six sections including this introductory chapter. Chapter 2 contains a literature review of the physical and engineering aspects of ferroelectric, ferromagnetic, and multiferroic memory as well as a theoretical model for multiferroic

nanowires as the motivation of this study. Chapter 3 is a detailed technical review of fabrication and characterization methods and reviews of selected materials used in this work. Chapter 4 describes the synthesis of template MgO nanowires, BaTiO<sub>3</sub> or NiFe<sub>2</sub>O<sub>4</sub> film-coated nanowires as an intermediate step toward multiferroic nanowires. Chapter 5 describes multiferroic ultrathin films of BaTiO<sub>3</sub> deposited heteroepitaxially on LaSrMnO<sub>3</sub> to form ferroelectric tunnel junctions (FTJ) and investigation of the tunneling properties. Finally, Chapter 6 concludes with suggested future work along with recommendations for the applications of the developed devices for memory and storage.

## CHAPTER 2

### LITERATURE REVIEW

#### 2.1 Memory Devices

##### 2.1.1 Ferroelectric memory

Ferroelectric oxide materials exhibit switchable and spontaneous polarization reversal by an applied electric field, piezoelectric behavior involving conversion of mechanical energy to electric energy, and large static dielectric permeability. These unique material properties make the ferroelectric oxide materials attractive for a wide range of device applications such as data storage, electromechanical transducers like piezoelectric actuators and capacitors [29]. Ferroelectric random access memory (FRAM) is one of the well-known devices offering non-volatile memory. In addition to non-volatility, the memory offers in recent technology generations fast access time (5 ns) and lower power consumption and competes with traditional semiconductor random access memory (RAM).

Some oxides of the perovskite family of compounds can be electrically polarized and are ferroelectric, retaining the polarization when the electric field is removed. When an external electric field is applied across the structure, there is a phase transition from cubic to tetragonal crystal orientation by physical displacement of a transition metal ion up or down in the unit cell along the field axis direction, resulting in non-centrosymmetry of the perovskite structure. A spontaneous polarization is then derived largely due to the dipole moment arising from the shift. Fig. 2.1 illustrates the structural distortion by the movement of a transition metal ion ( $Ti^{4+}$ ) in case of  $BaTiO_3$  and a hysteresis loop corresponding to the phase changes.

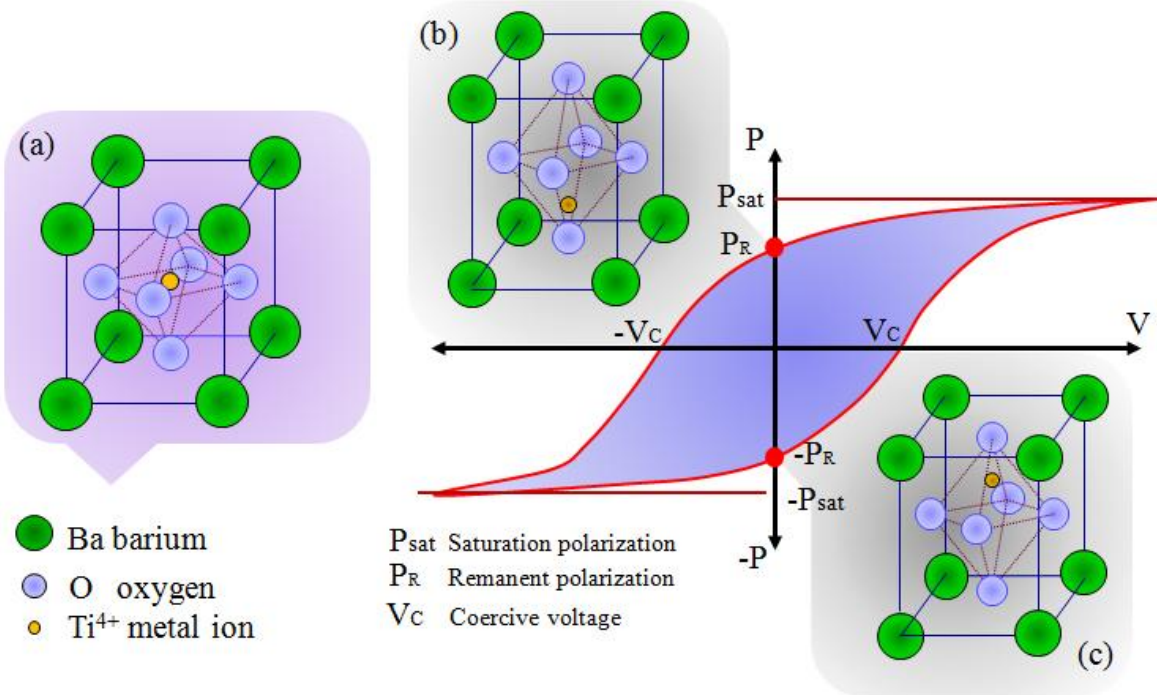


Figure 2.1 Perovskite structure of BaTiO<sub>3</sub> where a small cation (O) at the center of an octahedron of oxygen anions with large cations (Ba) at the unit cell corners, and (Ti<sup>4+</sup>) metal ions placed at a center of the unit cell. (b) and (c) illustration of a transition phase after Ti<sup>4+</sup> movements, Up/Down. Typical hysteresis loop is shown between (b) and (c) (Adapted from ref. [3]).

As described in Fig. 2.1, this polarization behavior makes the FRAM attractive as non-volatility memory.

A ferroelectric tunnel junction (FTJ) utilizes a very thin ferroelectric layer as an active barrier (spacer). In a FTJ, electrons are transported across the insulating ferroelectric barrier from one conductive electrode to another by quantum mechanical tunneling [19]. The concept was first proposed by Frenkel in 1930 [30] and its practical applicability was discussed by Esaki later in 1971 [31]. Fig. 2.2 depicts a schematic of a ferroelectric tunnel junction [32]. As illustrated in Fig. 2.2(a), because of incomplete screening at the ferroelectric barrier-electrode interface, polarization reversal of the barrier may have an effect on the conductance of FTJ, resulting in

tunneling electroresistance (TER) effect (ref. [32]). In addition, two effects can contribute to the tunnel current: a microscopic interface effect because of the shifting transition metal ion and strain resulting from piezoelectric effect, as seen Fig. 2.2(b) and (c), respectively.

In order to achieve the tunneling phenomena, the tunnel barrier should be an ultrathin film; otherwise electrons will not pass through the barrier because of exponentially decreasing tunneling probability with thickness and also scattering effects. Fabricating ultrathin ferroelectric layers is challenging not only because of defect formation but also due to the intrinsic loss of ferroelectric behavior below a critical thickness [33]. There are a few reports that take account of the thickness limit in terms of number of unit cells, above which ferroelectric  $\text{BaTiO}_3$  or  $\text{BiFeO}_3$  ultrathin films display ferroelectric and piezoelectric properties [34, 35].

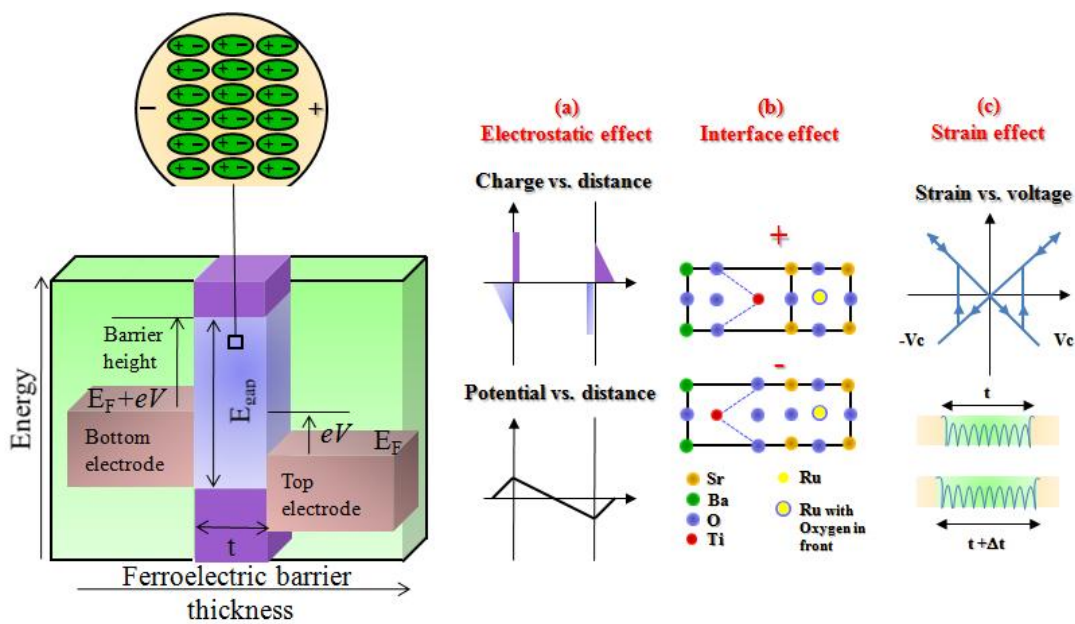


Figure 2.2 Schematic of the principle concept of ferroelectric tunnel junction (FTJ) and three fundamental mechanisms (a-c) that can lead to electric tunnel resistance. (Reproduced with permission from ref. [32]).

## 2.1.2 Ferromagnetic memory

Ferromagnetic oxide materials have been used in a broad range of magnetic-based data storage media, such as recording tapes for audio/video, hard disk head/write drivers, etc., [36] because of their unique properties such as spontaneous magnetization and ferromagnetic behavior. To explain the magnetization and ferromagnetism, Curie-Weiss's law and Stoner band theories generally use the phenomenon of the spin and orbital momentum of electrons developed in quantum physics [37]. Curie-Weiss law states that magnetic susceptibility ( $\chi$ ) at Curie temperature is given by

$$\chi = \frac{C}{T - T_C}, \quad (1)$$

where  $T_C$  is the Curie temperature related to a molecular field and  $C$  is the Curie constant. Below the Curie temperature, the molecular field defined by a magnetic moment enables a substance to be magnetized by a parallel alignment of electron spins to each other. On the other hand, Stoner band theory describes electrons partially coupling 3d and 4s orbital and different band energies required to reverse their state because of narrow (3d) or broad (4s) density of states at the Fermi level, as illustrated in Fig. 2.3. These different densities of state effect the exchange interaction for electrons, predicting easier spin reversal for the increased alignment of spins in 3d than in 4s bands to be ferromagnetic.

The physical understanding of the spin motion of electrons provides the basis of numerous innovations related to magnetic-based recording devices. Initially, write/read heads for hard disks were operated using magnetic induction ( $\vec{B}$ ). However, the induction field is too weak to be used as a signal generator when the storage bit size became smaller. As an alternative, magnetoresistance (MR) techniques were used to produce more sensitive read head component.

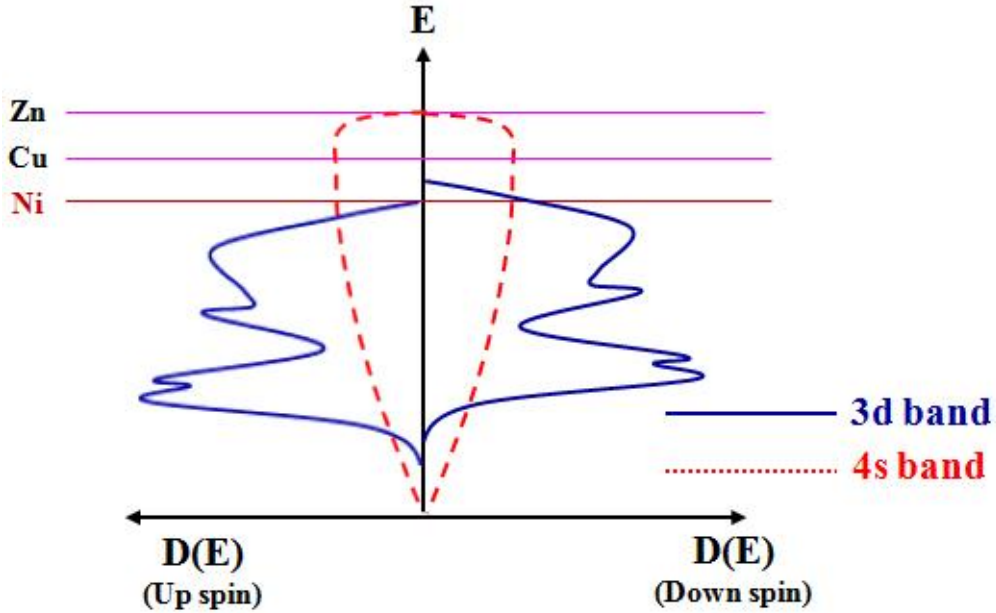


Figure 2.3 Schematic illustration of density of states in different metal oxide materials. 3d and 4s densities in first-row transition metals and electron spin up and down densities of states. The horizontal lines indicate the Fermi levels in ferrite materials, Zn, Cu, Ni, Co, Fe, and Mn. (Adapted from ref. [37]).

The first read head using MR was fabricated by IBM in 1991, which was configured utilizing anisotropic magnetoresistance (AMR), originally introduced by William Thomson in 1856. Since IBM's introduction of MR heads in hard disk drives, the data density of recording media has kept increasing each year. For instance, the data density in 1991 was  $0.1\text{Gbit/in}^2$  and the density in 2003 was  $100\text{Gbit/in}^2$ . Now, recording density of up to  $1\text{Tbit/in}^2$  is available [15]. The discovery of the giant magnetoresistance (GMR) and tunneling magnetoresistance (TMR) in place of AMR triggered this technical trend [38, 39]. The GRM is configured as a sandwich structure where two ferromagnetic electrode layers are separated by a non-magnetic metallic spacer layer. In GMR, the current flowing across the metallic layer varies depending on the relative magnetic configuration of the two ferromagnetic layers because of spin-dependent transport. Fig. 2.4 schematically illustrates resistive changes owing to spin alignment of the two electrodes (Fig. 2.4 adopts the CPP (current perpendicular to the plane) GMR structure). If the

electrodes are magnetized parallel to each other, then current flows more readily across the layer (low resistance), as seen in Fig. 2.4. (a). When the magnetization of the two electrodes are aligned antiparallel, very little current flows (high resistance) as seen in Fig. 2.4. (b) because of enhanced scattering at the interfaces.

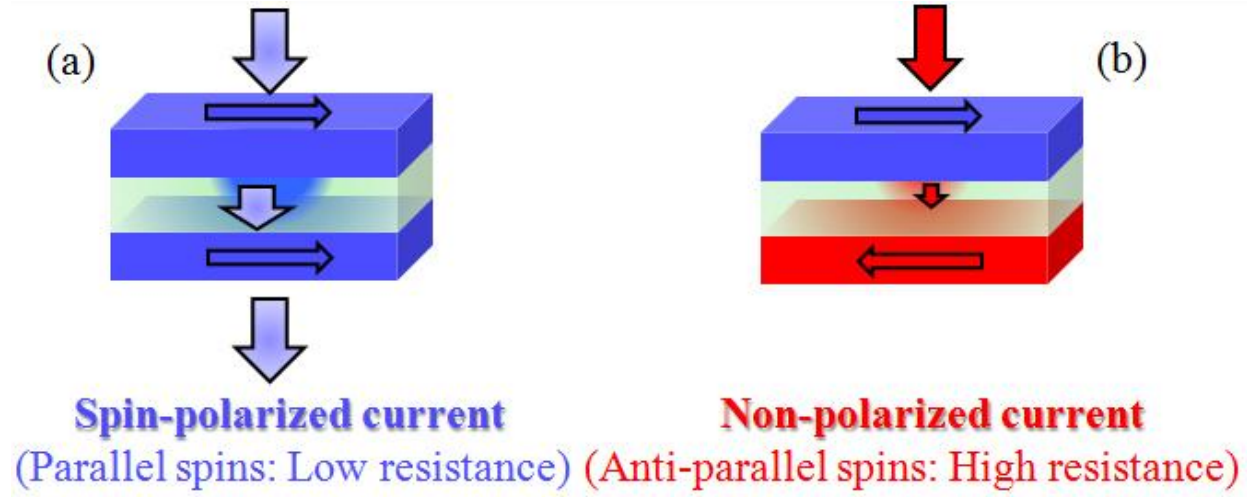


Figure 2.4 Schematic illustrating principle of giant magnetoresistance (GMR) due to the combination of electro spins. (a) Low resistance state with parallel spins direction of the two ferromagnetic layers. (b) High resistance state with anti-parallel spins direction of the two ferromagnetic layers.

A TMR structure is configured similar to GMR CPP excepting that the metallic layer spacer is replaced by a non-metallic insulating layer, thus creating a magnetic tunnel junction, as first proposed by Julliére in 1975 [40]. In TMR, electrons travel across the insulator by tunneling, in which the electron spin is conserved. The TMR structure has significantly advanced the design of magnetic solid state memory devices known as Magnetic Random Access Memory (MRAM). The MRAM promises to provide non-volatility, along with extended endurance and high density. However, the memory device has to overcome the drawback of high current (energy) consumption to control magnetoresistance changes through the spin alignments as part of the

writing information of the bits. The drawback can be more critical when the device size is scaled down to nanometer scale to achieve high data density because the large current, besides high-energy consumption, can be the source of device heating and the destruction of information bits. Therefore, it is a challenge to overcome this limitation.

### 2.1.3. Magneto-Electric Random Access Memory (MERAM)

Multiferroic memory, also referred to as magneto-electric random access memory (MERAM), has emerged as an attractive candidate that provides nondestructive reading and low power consumption in write operations [13]. Zhuravlev et al. first predicted the principle of MERAM utilizing magneto-electric tunnel junctions (METJ) [27], which combines the tunnel electroresistance (TER) and tunnel magnetoresistance (TMR) effects.

MERAM fundamentally consists of a sandwich layer structure as shown in Fig. 2.5. A thin insulating active layer is sandwiched between two ferromagnetic (FM) electrodes. Here, two types of sandwich layer can be chosen. One is a ferroelectric (FE) layer, as shown in Fig. 2.5(a), and the other is a single-phase multiferroic layer with combined properties of ferroelectricity (FE) and ferromagnetism (FM)/antiferromagnetism (AFM), as shown in Fig. 2.5(b). The layer configuration leads to changes in the tunnel current by manipulation of the magnetization parallel ( $R_p$ ) or antiparallel ( $R_{ap}$ ) between the two ferromagnetic electrodes. Moreover, the magnetization of the bottom ferromagnetic electrode can be electrically switched by changing the polarization of the underlying FE layer (ref. chapter 1)

Fig. 2.6 depicts a schematic layer structure of possible MERAM device (ref [13]). First, two ferromagnetic layers, top and bottom (blue color), are separated by a barrier. As expected in the TMR effect, there is a low or high resistance state depending on the magnetization configuration (or spin alignment) of the two ferromagnetic layers, parallel or antiparallel.

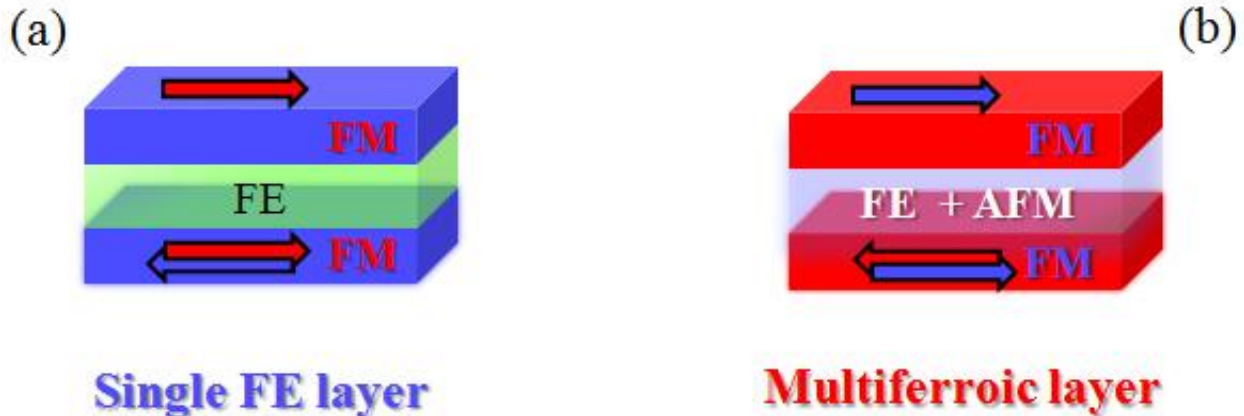


Figure 2.5 Two fundamental layer structures to configure MERAM. (a) Single FE layer is sandwiched by two FM layers. (b) Two FM layers are separated by a single-phase multiferroic with combined properties of ferroelectricity (FE) and ferromagnetism (FM)/antiferromagnetism (AFM).

Secondly, the bottom ferromagnetic layer is positioned on a multiferroic FE/AFM layer. When an electric field is applied across the multiferroic layer, the ferroelectric polarization is reversed. If the magnetoelectric coupling ( $ME_E$ ) (electric control for magnetization response) is strong enough by the reversed ferroelectric polarization field, electron spins rotate to reverse the spin state at the interface of the AFM, causing a magnetization configuration change of the bottom ferromagnetic electrode, with resulting parallel to antiparallel combination of the two ferromagnetic electrodes. The change in magnetization configuration results in a resistance change of the junction from low to high. Here, it is important to note that an electric field is used to manipulate the relative spin alignment (parallel  $\Leftrightarrow$  antiparallel) instead of a larger current, as required in MRAM. This concept of “ferroelectric control of spin polarization” is thus attractive for low energy switching of spintronic devices.

Another concept of ferroelectric control of tunneling was first demonstrated by Garcia et al. in an experiment probing the spin polarization of electrons tunneling between metallic electrodes through a thin ferroelectric  $BaTiO_3$  (BTO) tunnel barrier [41]. To demonstrate this

effect experimentally, they used half-metallic LaSrMnO<sub>3</sub> (LSMO) bottom electrode as a spin detector. Thereby the BTO/LSMO bilayer artificially provides a multiferroic tunnel junction (MFTJ). They measured the TMR effect by manipulating the ferroelectric polarizations and TER behavior through the BTO tunnel barrier at low temperature (4.2K).

The coexistence of TMR and TER effects in the MFTJ offers the potential of MERAM device combined with MRAM and FRAM to read/write binary information. Furthermore, the MERAM device offers a four-state resistance with the combination of two electric polarization ( $\pm P$ ) and magnetization ( $\pm M$ ) states [42].

The key to the success of this type of device is the development of an ultrathin ferroic film acting as the tunnel barrier that retains ferroelectric properties [17]. The recent discovery of ferroelectric properties being retained in ultrathin ferroelectric layers has opened ways to explore this novel layer architecture [43]. Indeed, a few groups have reported the development and characterization of ultrathin ferroic films to demonstrate potential for magnetoelectric random access memory devices [44].

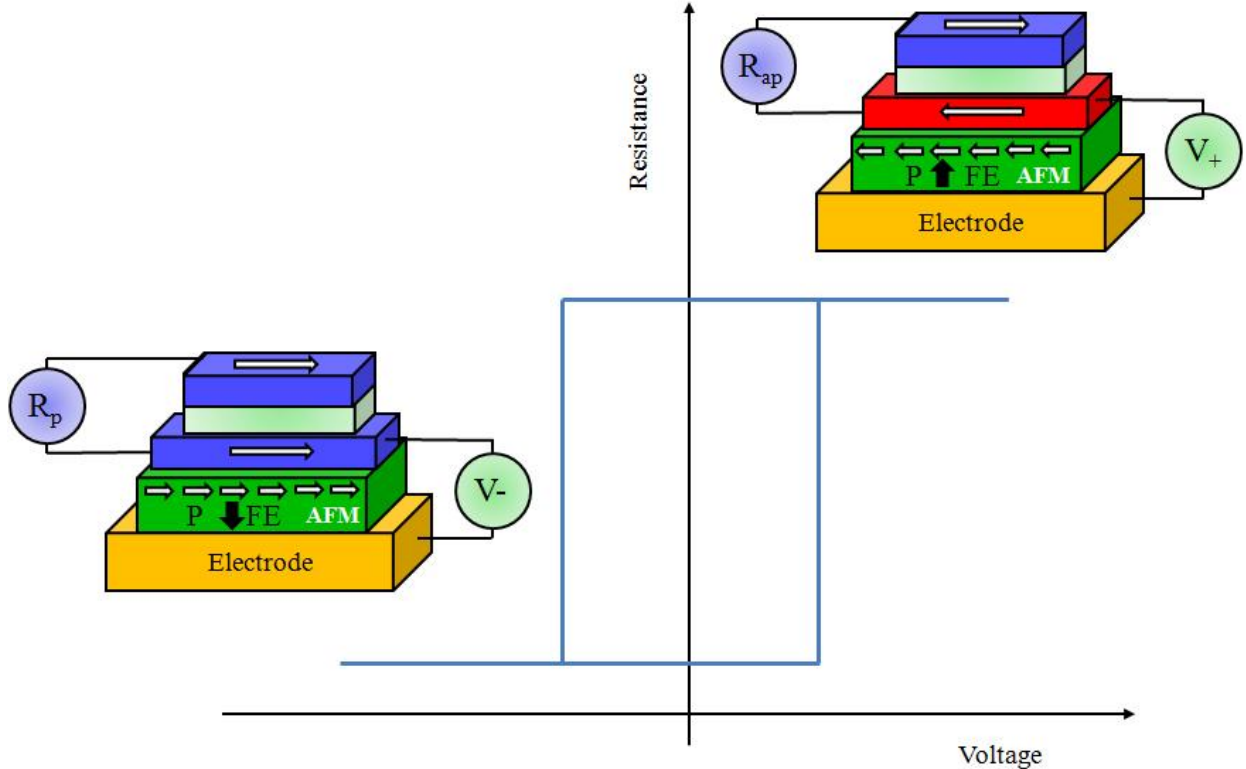


Figure 2.6 Schematic of the layer structures of MERAM. (a) Two ferromagnetic layers (blue color) are aligned. Low or high resistance state owing to the magnetization configuration (parallel or antiparallel) of the ferromagnetic layers. (b) A bottom ferromagnetic layer is on the multiferroic layer. If magnetoelectric coupling ( $ME_E$ ) is strong enough by the ferroelectric polarization in the multiferroic layer the electron spins rotates to reset the magnetization configuration change of the bottom ferromagnetic layer, resulting parallel to antiparallel combination of the two ferromagnetic electrodes (Reproduced with permission from ref. [13]).

## 2.2 Multiferroic compositions

After discovery of the first multiferroic material nickel iodine boracite,  $Ni_2B_7O_{13}I$  [45], various bulk single-phase ceramic multiferroics have been extensively investigated in the 20<sup>th</sup> century. In particular, perovskite-type  $RMnO_3$  oxides, where R is rare-earth materials like Y, Bi, Ho, La, and Nd, Mn=manganites, have received much attention [46]. There are, for instance, yttrium manganite  $YMnO_3$  (YMO) and bismuth Bi-based compounds such as  $BiMnO_3$  (BMO) and  $BiFeO_3$  (BFO), which exhibit ferroelectricity and anti-ferromagnetism.

Such single-phase materials are, however, very limited. The critical issue is that a limited number of single-phase compounds exist in nature because of the inconsistency of coexistence of ferroelectricity requiring an insulator and ferromagnetism needing a non-d<sup>0</sup> transition metal in the same phase at room temperature [47].

As alternative, Van Suchtelen [48] proposed the concept of a two-phase ceramic composite in 1972 and predicted that the ME response of the material could result from elastic coupling between the ferromagnetic and ferroelectric phases. Based on his theory, scientists in Philips Laboratory synthesized the two-phase ceramic composite of BaTiO<sub>3</sub>-Ni(Co, Mn)Fe<sub>2</sub>O<sub>4</sub> [49]. In the early 1990, other two-phase ceramic multiferroics using ceramic composites of ferrites and Pb(Zr·Ti)O<sub>3</sub> (PZT) were studied by typical sintering processes [50]. The experiments motivated theoretical studies [51]. Both experimental and theoretical work encouraged scientists to study various families of bulk two-phase ceramics. However, the two-phase ceramics still have limitations for practical devices because of their drawbacks such as porosity, uncontrolled dispersion or brittle and high eddy current loss at the interface, resulting in low ME effect.

From the last several years, various film techniques like pulsed laser deposition (PLD), sputtering and molecular beam epitaxy (MBE) have been employed to synthesize multiferroic films [52, 53, 54]. BiMnO<sub>3</sub> (BMO), BiFeO<sub>3</sub> (BFO), and YMnO<sub>3</sub> (YMO) films were actively studied [55, 56, 57]. Even though bulk film composites have received considerable attention, there is a significant negative aspect, which is large strain in films because of the much thicker substrate, resulting in a low ME coefficient.

Nanostructured thin films designed by a coupling of ferroelectric (FE) and ferromagnetic (FM) layers have been introduced because the structure can offer more degrees of freedom such as potential porosity, lattice strain and interlayer interaction which were drawbacks presented in

previous multiferroic compositions. As the first successful work, a vertical heterostructure was experimentally reported in a structure of nanopillar geometry and proved theoretically later [58, 59]. The structure was synthesized by a self-assembly method involving magnetic spinel,  $\text{CoFe}_2\text{O}_4$  (CFO), implanted into a ferroelectric perovskite matrix,  $\text{BaTiO}_3$  (BTO), using pulsed laser deposition. The vertical nanopillar structure displayed high remanent magnetic polarization ( $M_r$ ) close to  $300\text{emu}/\text{cm}^3$  and low remanent electric polarization ( $P_r$ ) of approximately  $10\mu\text{C}/\text{cm}^2$ . However, the vertical structure showed a critical drawback, which is leakage through the interfaces of the nanopillar matrix, leading to low resistance. The leakage problem ultimately reduces ME effect, limiting device applications. Years later, a horizontal heterostructure was experimentally and theoretically studied coupling bilayers with ferroelectric, BTO and ferromagnetic,  $\text{NiFe}_2\text{O}_4$  (NFO) or CFO, films [60]. The horizontal structure reduces the leakage problem found in the vertical structure by being a ferroelectric layer acting as insulator to cut off current flow. The structure however exhibits weak magnetoelectric (ME) effect because of clamping condition owing to the large two-dimensional substrate thickness and lattice strain at interface between films and substrate. Therefore, it is still challenging to resolve the weak ME coefficient and the constraint.

As another coupled multiferroic, the combination of ferromagnetic (FM) and dual ferroic order materials combined with ferroelectricity/antiferromagnetism (FE/AFM) has been investigated. Lanthanum barium manganite ( $\text{LaBaMnO}_3$ , LBMO) and yttrium manganite ( $\text{YMnO}_3$ , YMO) have been studied. However, there materials are not very attractive because of the coexistence of the coupled ferroic properties only at low temperatures [16, 61], which is undesirable for practical applications. As another choice, bismuth ferrite ( $\text{BiFeO}_3$ , BFO) has

been extensively studied as a potential candidate because of the appearance of the binary ferroic orders (AFM /FE) at room temperature [62].

These types of multiferroics have received great attention as emerging materials for use in magneto-electro random access memory (MERAM) devices because of the dual principal mechanisms to store and retrieve information by using magneto electric tunnel junction (METJ). However, it is challenging to obtain the strong coupling of ferroelectricity and ferromagnetism (or antiferromagnetism) in an ultrathin film, a few unit cells. A few groups have reported the development and characterization of the coupled multiferroic thin films [35, 44, 63]. Table 2.2.1 briefly summarizes the multiferroics discussed above.

TABLE 2.2.1 Multiferroic compositions

Type	Materials	Properties	Reference
Bulk Ceramic	Single-Phase	RMnO <sub>3</sub> :	Ferroelectricity (T <sub>C</sub> =600-900K, 5.5 μC/cm <sup>2</sup> )
		YMnO <sub>3</sub>	Antiferromagnetism(T <sub>N</sub> <80K),
		BiMnO <sub>3</sub>	Ferromagnetism(T <sub>C</sub> =105K), Ferroelectricity (T <sub>C</sub> =750K)
		BiFeO <sub>3</sub>	Antiferromagnetism(T <sub>N</sub> <653K), Ferroelectricity (T <sub>C</sub> =1083K)
	Two-Phase	BaTiO <sub>3</sub> + Ni (Co, Mn)Fe <sub>2</sub> O <sub>4</sub>	ME coefficient 0.3mV/cm Oe
		CoFe <sub>2</sub> O <sub>4</sub> + Pb(ZrTi)O <sub>3</sub> (PZT)	Easy and cost effective, Lower ME coefficients,
		Ni, Co + (La, Ca)MnO <sub>3</sub>	Low-frequency magnetoelectric (ME)
Bulk Film	Single Phase	BiMnO <sub>3</sub>	Ferromagnetism(T <sub>N</sub> =105K), Ferroelectricity (T <sub>C</sub> =450K)
		BiFeO <sub>3</sub>	High spontaneous polarization at ~60μC/cm <sup>2</sup>
		YMnO <sub>3</sub>	Antiferromagnetism(T <sub>N</sub> =70-130K), Ferroelectricity (T <sub>C</sub> =570-990K).
	Ferroelectricity + Ferromagnetism	Vertical: BaTO <sub>3</sub> +CoFe <sub>2</sub> O <sub>4</sub>	Nanopillar geometry, High Mr, 300emu/cm <sup>3</sup> Low Pr, 10μC/cm <sup>3</sup> , leakage problem
Nano-structured Film		Horizontal: BaTiO <sub>3</sub> + NiFe <sub>2</sub> O <sub>4</sub>	Weak ME effect, Eliminate a leakage problem Clamping effect owing to two-dimensional substrate
Ferroelectricity/ Antiferromagnetism + Ferromagnetism	Horizontal: BiFeO <sub>3</sub> +LaSrMnO <sub>3</sub>	Effective ME <sub>E</sub> - electric controlled for magnetization Exchange bias (EB) is expected	
		61	

### 2.3 Multiferroic nanowires

Two-dimensional (2-D) geometry has been normally used as a substrate template where desired materials are deposited to form multiferroic films. The 2-D structure morphology however results in clamping effect because of the significantly larger volume of the substrate as compared to the film. The clamping effect significantly diminishes the piezoelectric behavior associated with ferroelectricity, which is critical to influencing the magnetization in multiferroic composites. Therefore, it is necessary to reduce or minimize the clamping condition to enhance the magnetoelectric (ME) response.

One-dimensional (1-D) geometry nanostructures, such as nanorods or nanotubes, could be a good candidate as substrate template. Nanowires (NW) and nanotubes (NT) offer significant advantages in novel semiconductor applications including logic circuit devices and memory, field effect switchers, transistors, chemical and biomedical sensors [23]. They can help enhance the sensitivity and array density of nanodevices. Therefore, research has been performed on the synthesis, structure morphology characterization, and integration of NW elements using various materials such as magnesium oxide (MgO) [64], zinc oxide (ZnO), silicon (Si), gallium nitride (GaN), etc [65].

In addition, functional NWs containing ferroelectric or ferrite properties have been receiving much interest recently. The functional NWs offer electric and magnetic device applications with multifunctional properties such as polarization, phase deformation, photoelectricity, etc. Ferroelectric and ferrite functional NWs such as BaTiO<sub>3</sub> and MgO/Fe<sub>2</sub>O<sub>4</sub> core-shell have been reported [66, 67].

Moreover, one-dimensional nanostructures based on template post can open opportunities to explore a wide-range of nanowire material, which encapsulate desired functional

materials in the post [28]. The nanostructure will reduce volume interaction at the interface of films and the substrate, resulting in minimized clamping effect as compared to 2-D structures. For instance, Rao et al. reported a synthesis method to fabricate functionalized nanowires, which have magnetic properties by encapsulating iron (Fe) with carbon nanotubes [68]. Petrov et al. also presented a theoretical model for a multiferroic nanowire consisting of a ferroelectric and ferrimagnetic film on template MgO NW [22]. They showed that the NW composite could exhibit high magnetoelectric (ME) response because of the reduced clamping effect resulting primarily from the reduced substrate volume. The theoretical study motivated us to develop a new geometry of multiferroic structure.

In order to fabricate the multiferroic nanowire structure, there are challenges related to well-controlled growth conditions onto a template NW and high crystalline quality of both ferroelectric and ferrite films without any cracks or defects. Therefore, it requires more studies for successful fabrication of the heterostructure multiferroic nanowires.

## CHAPTER 3

### FABRICATION AND CHARACTERIZATION TECHNIQUES AND REVIEW OF SELECTED MATERIALS

#### 3.1 Fabrications

##### 3.1.1 Pulsed laser Deposition (PLD)

Thin films were deposited by pulsed laser deposition (PLD). In this technique [52] a pulsed laser beam strikes a source material, resulting in species such as ions, electrons, radicals, and molecules to be ejected off in a plasma plume. These active species react over the heated surface of substrate with background gases to nucleate and grow the film. A schematic diagram of PLD system used in this study is depicted in Fig 3.1.1.

The system has a dual vacuum vessel consisting of a load lock and process chamber. The process chamber is usually locked and only unlocked while moving samples through the load lock chamber. Thus our deposition system is maintained under high vacuum (less than  $10^{-6}$  Torr) condition without any significant contamination. A magnetic vacuum chuck is used to load and unload samples. A focused laser beam from a KrF Excimer laser (Lambda Physik, Model Compex Pro., wavelength  $\lambda=248\text{nm}$ ) is directed through a quartz window and ablates a ceramic target material of interest for film growth. The resulting plasma plume transports the ablated species to the substrate placed on a heater maintained at a specific temperature for film growth.

Prior to introduction of the substrate into the process chamber, it is cleaned in a sonicator with organic solvents (acetone and isopropyl alcohol for 10 minutes each) to eliminate any potential organic contamination. Silver paste is used to glue the substrate to the heater plate.

High-density ceramic disk targets of BaTiO<sub>3</sub>, NiFe<sub>2</sub>O<sub>4</sub>, and LaSrMnO<sub>3</sub> are placed in the process chamber and rotated during ablation process to induce uniform removal of material from the selected target material.

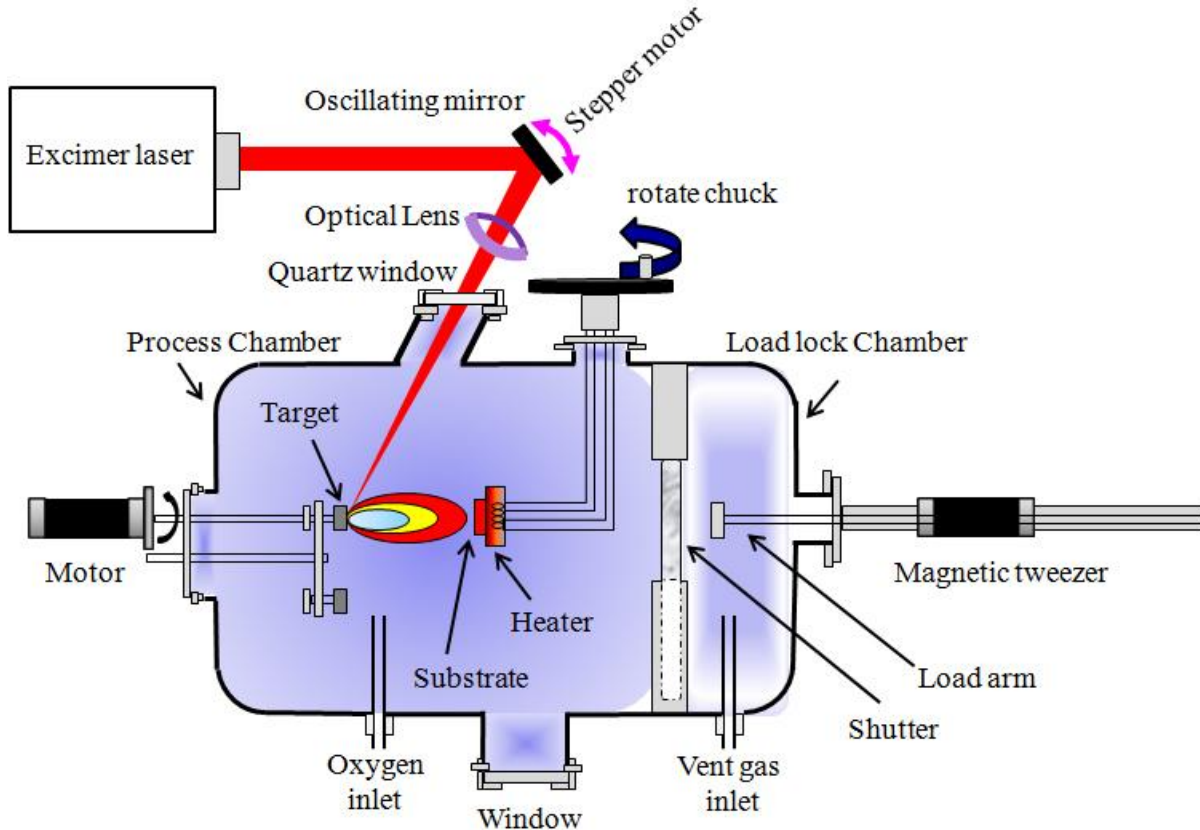


Figure 3.1.1 Schematic of a PLD system used in this study. It consists of a ultra-high vacuum vessel combined with a load lock and process chamber, a circular disk for rotating multiple targets, a load arm to insert a substrate into the process chamber, heating elements, gas delivery ports, optical lens and quartz window to guide Excimer laser beam into the process chamber.

### 3.1.2 Chemical Vapor Deposition (CVD)

Magnesium oxide nanowires (MgO NWs) were synthesized by chemical vapor deposition (CVD). The NWs grow following a gas-phase production method, referred to as vapor-liquid-solid (VLS) mechanism. This method was originally discovered by Wagner and Ellis [69] who produced micrometer-sized silicon (Si) whiskers in the 1960. They found that the vaporized silicon precursor after reduction nucleated on nanosized liquid droplets of Au-Si alloy

that acts as a catalyst. The incoming Si from decomposition of the precursor freezes after entering the liquid. With continuation of the process the alloy droplet is displaced and rides on top of the growing single crystalline Si nanorod. Fig. 3.1.2 provides a schematic of the CVD system used in our study. It consists of a quartz tube as a reaction vessel, a furnace, a temperature controller, and a delivery system to introduce reaction gases. During the process, (001)-MgO substrate is placed downstream from a quartz boat containing the magnesium nitride ( $Mg_3N_2$ ) powder precursor inside the quartz reaction tube. A fixed flow rate of 100 standard cubic centimeter per minute (sccm) ultra-pure argon gas is mixed with a 60 sccm flow of 0.98% Ar/0.02% O<sub>2</sub> mixture and introduced at atmospheric pressure into the reaction tube placed inside the furnace. The furnace temperature is then raised to 925°C, whereby Mg<sub>3</sub>N<sub>2</sub> volatizes and decomposes into its constituent elements. Argon acts as a carrier gas to transfer the elemental magnesium produced by decomposition onto gold catalyst covered substrates for the growth of the MgO NWs by oxidation, as shown in the schematic diagram of Fig. 3.1.3.

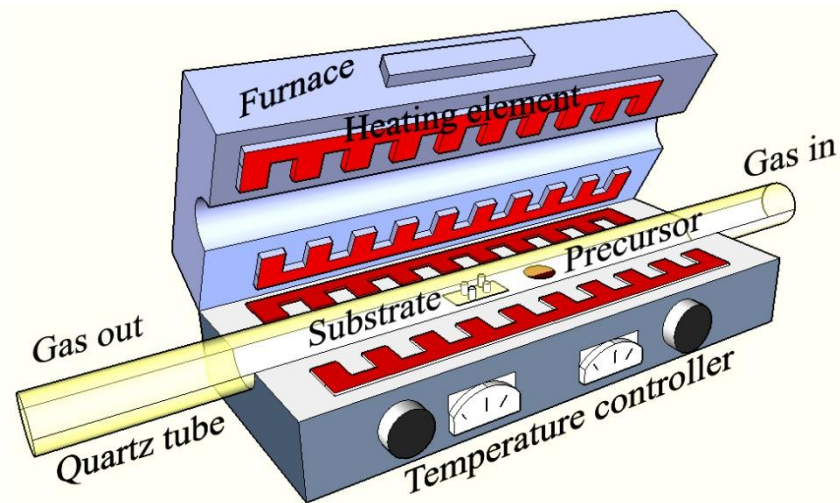


Figure 3.1.2 Schematic of a typical CVD system for synthesizing nanowires (NWs). It consists of a quartz reaction tube, a furnace to provide required high temperature, gas inlet/outlet ports, precursor source and a substrate where NWs are grown.

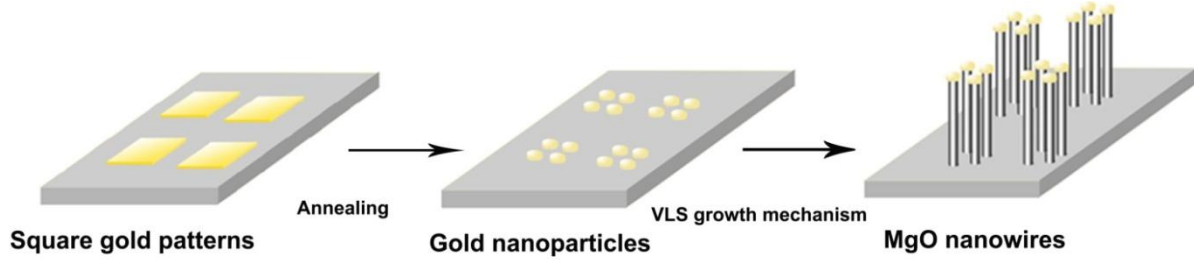


Figure 3.1.3 Schematic diagram illustrating the growth sequence of MgO nanowires. The square gold regions are patterned using e-beam lithography. Gold nanoparticles are formed within the square region at a critical annealing temperature ( $925^{\circ}\text{C}$ ). Single free-standing MgO NWs are grown on the substrate with the gold particles being lifted up. (Reproduced with permission from ref. [81])

### 3.1.3 Electron beam (e-beam) lithography

Electron beam (e-beam) lithography is a widely used technique for patterning nanoscale features that are below the range for optical lithography [70]. When a high resolution e-beam emitted from an electron gun is exposed to a spin-coated resist film (PMMA: Poly(methyl methacrylate), a positive resist), the exposed region will be removed from the wafer after a developing process. (In the case of a negative resist, e.g., Fox-12, the exposed region remains after the developing process). A schematic diagram describing steps in the e-beam lithography process is shown in Fig. 3.1.4.

Exposed regions are patterned in concave or convex shapes depending on the film type; positive or negative resist. Electron beam evaporation or sputtering is used to fill the patterned zone with a desired material (gold thin film is used as a contact element in this work). Then, a lift-off process removes the remaining resist film. Contact patterns ultimately appear as shown in the Fig. 3.1.4(e) after rinsing with acetone, isopropyl alcohol (IPA), and deionized water.

In this study, the e-beam lithography technique was applied to pattern three different square arrays of dimensions  $0.25$ ,  $1$ , and  $4 \mu\text{m}^2$  and  $10 \times 10$  dot arrays a couple of hundreds nanometer in radius. In addition, four-point contact pads for measuring the magneto-electric

response of a single multiferroic nanowire were fabricated. In this study, a JEOL-7000F FEG-scanning electron microscope (SEM) equipped with Nabity electron beam lithography was used to produce these patterns.

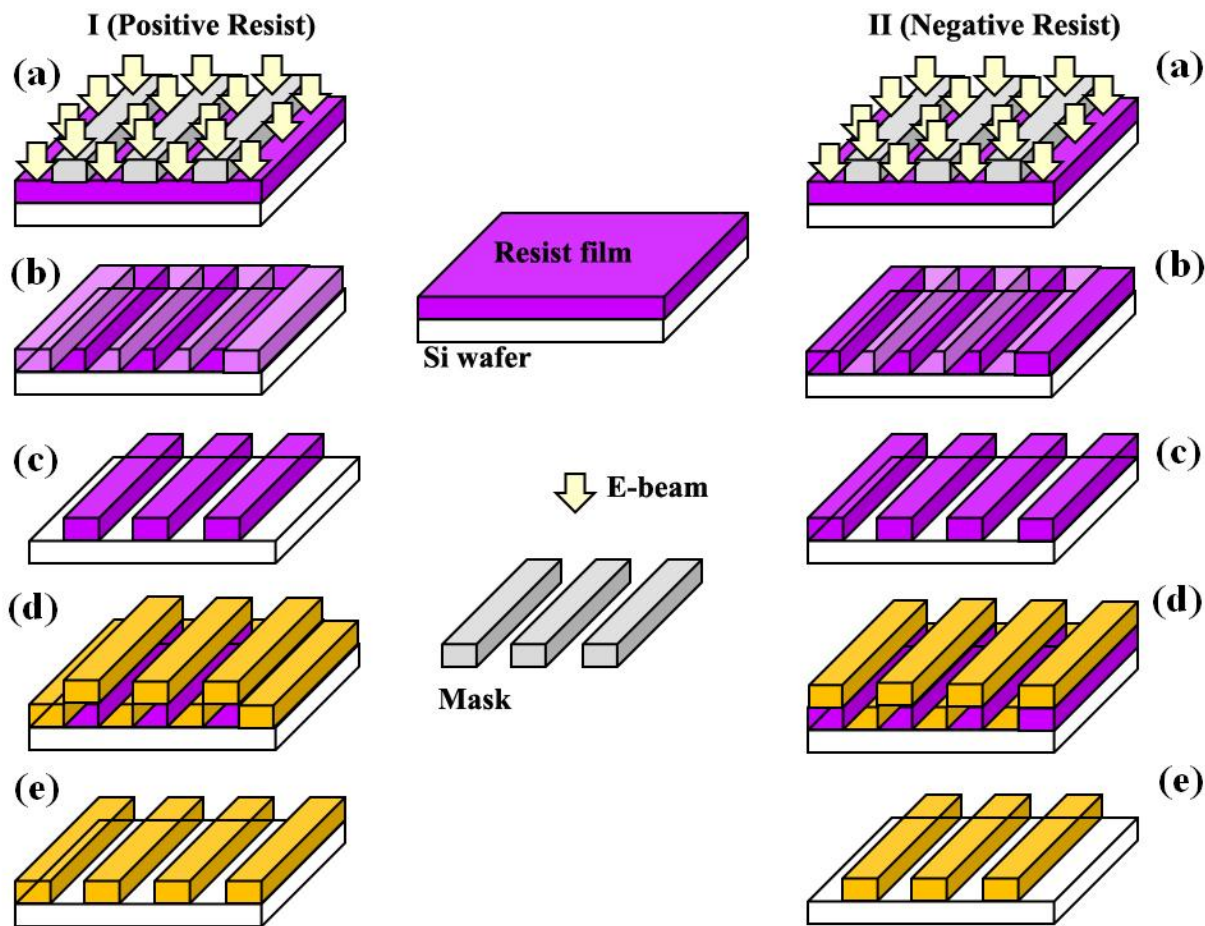


Figure 3.1.4 Schematic illustrating the process of E-beam Lithography. Two kinds of patterning processes are described depending on properties of resists, positive and negative films as shown in case (I) and (II). As an initial preparation, E-beam resist is spin coated on silicon wafer as shown in the middle figure. (a) E-beam penetrates through the pattern mask. (b) Exposed resist changes chemical structure to become more soluble in the developer. (c) After developing, exposed region is removed in the case of positive resist and retained in the case of negative resist. (d) Thin gold film is deposited using e-beam evaporator. (e) After stripping to remove unexposed resist, final patterns with gold thin film remains.

### 3.2 Characterization

#### 3.2.1 X-ray diffraction (XRD)

XRD is a powerful technique for studying crystal properties of samples ranging from powders to thin films [71]. The XRD instrument generally consists of x-ray source and a detector. The x-ray beam emitted from the source strikes a crystal in the  $\theta$ - $2\theta$  plane and produces a diffracted beam following Bragg's law, which describes interference of incident and diffracted x-ray beams at certain angles in the crystal. A schematic diagram describing Bragg's law is provided in Fig. 3.2.1. The x-ray beam enters the regularly arrayed atoms of the crystal and generates diffraction through different travel paths. Analysis of these diffraction beams determines crystal properties such as atomic structure, chemical bonds, and disorders.

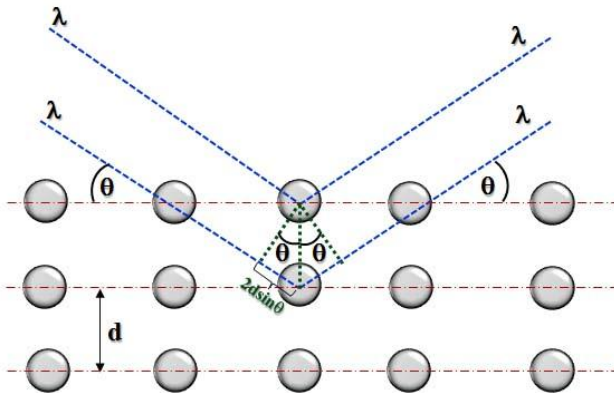


Figure 3.2.1 Schematic diagram illustrating Bragg's law, where  $n$  is an integer,  $\lambda$  is the wavelength of X-ray,  $d$  is the lattice spacing, and  $\theta$  is the diffraction angle.

The condition of interference determined from Bragg's condition is

$$2ds\sin\theta = n\lambda \quad (1)$$

The angle  $\theta$  is obtained from a XRD scan and corresponds to the plane of the crystal, and then the lattice spacing  $d$  can be calculated from the Bragg's equation.

X-ray reflectivity (XRR) is a useful method to estimate thickness of thin films. When x-ray is incident at a small angle to the thin film, intensity oscillations are observed in the reflected beam as shown in Fig. 3.2.2 (a) because of interference of the reflections at the interfaces of air/film and film/substrate. By adopting Bragg's law, eq. (1) can be re-written by forming  $y=m(x)$  as

$$n_x = d\left(\frac{2\sin\theta}{\lambda}\right). \quad (2)$$

The terms are defined such as  $n$  equals  $y$ ,  $d$  equals  $m$ , and  $\left(\frac{2\sin\theta}{\lambda}\right)$  equals  $x$ . In addition,  $n_x$  is

given as the  $n$ th oscillations from XRR as shown in Fig. 3.2.2(a). All critical numbers including  $\theta$  and  $\lambda$  are known except  $d$ , which is given by the slope, i.e., the film thickness as

shown in Fig. 3.2.2 (b). In this instance, the thickness is estimated to be approximately 50 nm.

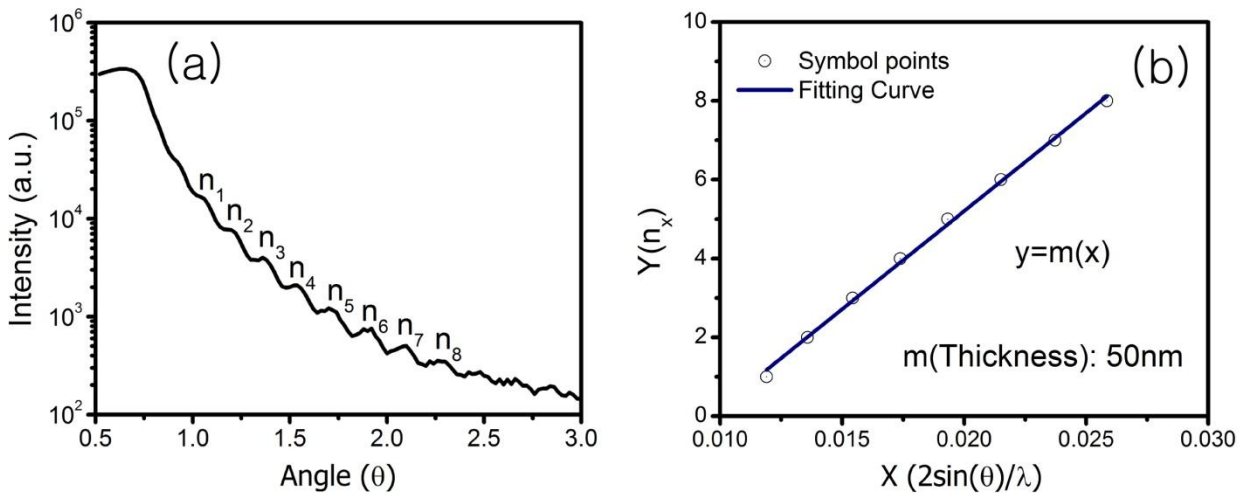


Figure 3.2.2 Theoretical method to determine the film thickness using X-ray reflectivity (XRR) technique. (a) Oscillation curves (b) Symbols indicate the calculated data points using Eq. (2). Linear fit is applied to determine the value of slope, providing the film thickness.

Pole-figure analysis is also a powerful method to investigate the crystal structure. Polar coordinates consisting of a tilt angle psi ( $\psi$ ) ( $\psi < 90^\circ$ ) and rotation angle phi ( $\phi$ ) ( $\phi < 360^\circ$ ) allows one to evaluate epitaxy referring to the crystalline overlayer on a substrate. Fig 3.2.3 shows a schematic diagram describing a way to adjust tilt and rotation angles for a pole-figure measurement.

In our studies, a Philips X' Pert X-ray diffraction instrument equipped with Cu source  $K\alpha$  in a single wavelength,  $1.5405 \text{ \AA}$ , was utilized for the characterizations of thin films.

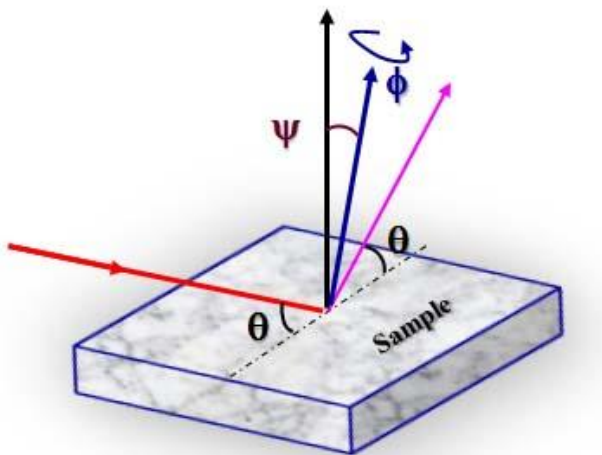


Figure 3.2.3 Schematic providing a view of tilt and rotation angles for pole figure measurement. Here tilt, psi ( $\psi$ ) ranges from  $0^\circ$  to  $90^\circ$ , and rotation phi ( $\phi$ ), ranges from  $0^\circ$  to  $360^\circ$ .  $\theta$  is an incident angle of X-ray beam with respect to substrate surface.

### 3.2.2 Transmission electron microscopy (TEM)

Transmission electron microscopy (TEM) is used to characterize the microstructures of a wide range of materials, including metallic, ceramic and biological samples [72]. The microstructures include the morphological and crystallographic features as well as local chemical composition. A TEM system generally consists of a high voltage electron source ( $>100\text{kV}$ ),

electromagnetic focal lenses, a series of lenses to view TEM images, and a columnar ultrahigh vacuum vessel. The electrons emitted from the source (filament) are accelerated by the high voltage source and focused through the electromagnetic focal lenses onto a specimen. The electron beams are scattered by the specimen and then the diffracted beams are brought to focus by objective lenses on its back focal lens and form a diffraction pattern. Finally, a TEM image or diffraction pattern can be produced on the fluorescent viewing screen by a series of lenses such as an objective, intermediate and projection lens.

The TEM imaging and diffraction techniques include TEM bright or dark field, electron diffraction, high-resolution TEM, and energy-dispersive x-ray spectroscopy (EDS). The bright field (BF) image is formed by the electrons transmitted through an objective aperture, which is inserted at the back focal plane of the objective lens. The BF images are used to determine the size and shape of a specimen. On the other hand, the dark field (DF) image is formed by the electrons diffracted at the objective aperture. The DF image provides better contrast than BF image but suffers from low light intensity. Fig. 3.2.4 shows schematics of both BF and DF TEM imaging modes. The high-resolution (HRTEM) image provides detail information such as a high magnification image of a specimen down to nanoscale and crystallographic features such as lattice spacing of the material specimen. The high-energy electrons in TEM cause electron excitations of the atoms in the specimen. The EDS technique uses the excitation electrons to provide chemical information of the specimen.

A FEI Tecnai F20-200 keV TEM system was utilized to characterize the microstructures of MgO nanowries and BaTiO<sub>3</sub> or NiFe<sub>2</sub>O<sub>4</sub> coated nanowires in our studies.

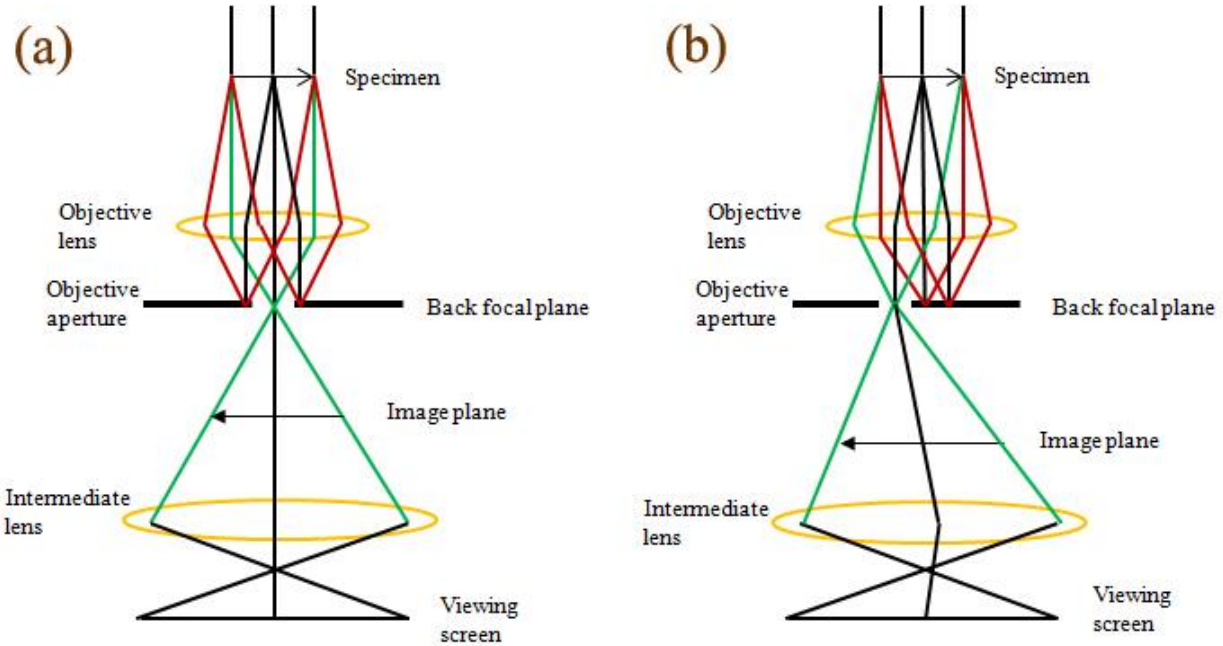


Figure 3.2.4 Schematic of the TEM image modes. (a) Bright-field image mode (b) Dark-field image mode. (Adapted from ref. [72]).

### 3.2.3 Piezoresponse force microscopy (PFM)

PFM is an instrument used to determine local ferroelectric and piezoelectric properties on the nanoscale [73]. This method images the phase angle from  $0^\circ$  to  $180^\circ$  as part of electromechanical response under an externally applied electric field. An AFM tip coated with a conductive material, e.g., platinum (Pt), scans over a piezoelectric film surface in contact mode to sense the phase deformation arising from contraction and expansion of the film as a function of DC bias of the tip. Fig. 3.2.5 is a schematic diagram depicting how the phase deformation is imaged while the tip is scanned over the surface and senses the degree of displacement. The sensing signal detected by a photodiode is transmitted to a lock in amplifier to create PFM images.

Local switching properties are also characterized. For the measurement, a saw tooth-shaped bias is swept while the tip contacts a local point zone. The phase and amplitude hysteresis

loops are obtained owing to local polarization changes corresponding to the sweep voltages.

In this study, MFP-3D (Asylum Research) equipped with conventional atomic force microscopy (AFM) to acquire surface topography was used to observe ferroelectric polarization and local switching characteristics of ultrathin films.

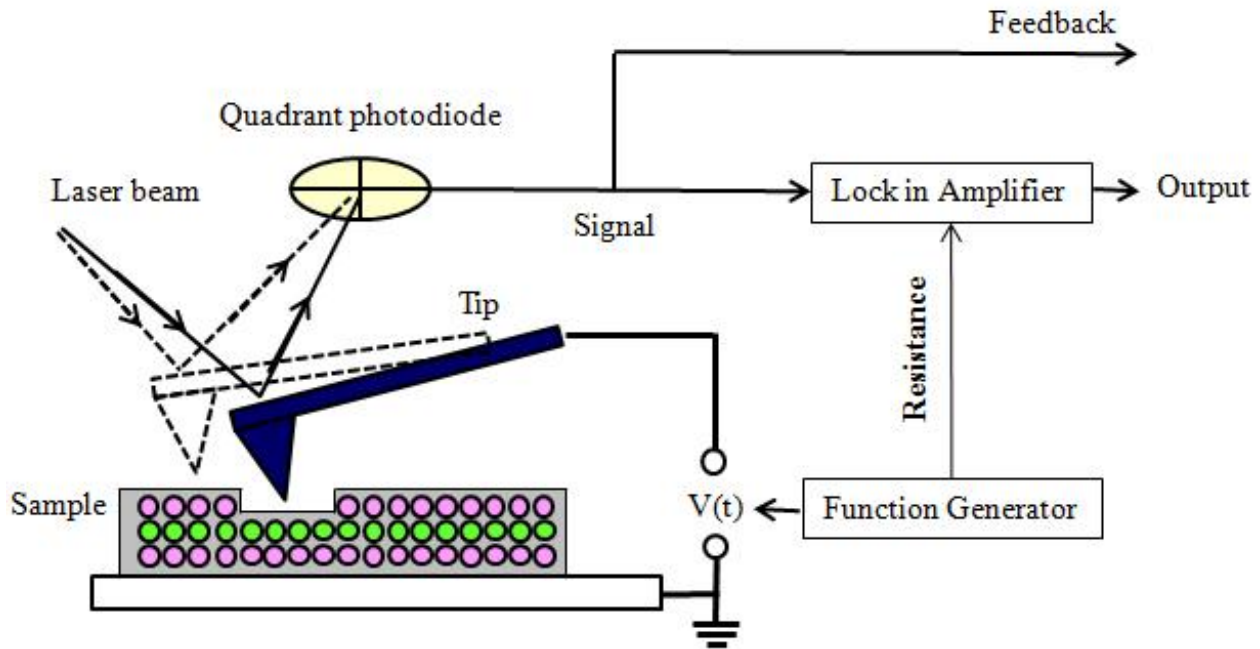


Figure 3.2.5 Schematic of typical PFM measurement system. The phase deformation of a sample is occurred by biased initial tip scans. Then the AFM tip (dashed and solid) indicates the electromechanical displacement while scanning over the surface and visualizes the phase image through imaging processes.

### 3.2.4 Conducting atomic force microscopy (C-AFM)

Conducting AFM (C-AFM) is a technique that provides nanoscale current-voltage ( $I-V$ ) characterization of ferroelectric (FE) ultrathin films. During the measurement, a tip serves as a counter electrode to the bottom metallic electrode so that the basic configuration is tip/FE barrier/metallic electrode, providing an asymmetric electrode configuration. Fig. 3.2.6 depicts a schematic of the C-AFM measurement. As seen in the Fig. 3.2.6 a conductive AFM tip scans the surface of a sample with an applied bias voltage. The tip thereby detects a high or low

conductivity in a scanned zone. Then, the current is obtained using the basic relevant equations

$$\frac{V_{out}}{R_{gain}} = \frac{V_{in}}{R_{sample}} \quad (1)$$

$$V_{out} = R_{gain} \left( \frac{V_{in}}{R_{sample}} \right) \quad (2)$$

$$V_{in} = \frac{V_{out}}{R_{sample}} \quad (3)$$

$$V_{out} = I_{in} R_{gain}. \quad (4)$$

Here,  $R_{sample}$  is the sample resistance,  $R_{gain}$  is the parallel resistance from connection to the current amplifier,  $V_{in}$  is the applied voltage through the sample,  $V_{out}$  is the voltage at readout, and  $I_{in}$  is the current through the sample.

Another use of C-AFM is to measure current ( $I$ ) vs. voltage ( $V$ ) curves to investigate the electrical characteristics of the sample surface. For this purpose, a linear sweep voltage is applied through an ultrathin film. The  $I$ - $V$  curves are then plotted of variable currents as a function of the sweep voltage through the sample. In this study, the  $I$ - $V$  curves were obtained at local regions, which are polarized either down or up, resulting in two different conductive states, low or high.

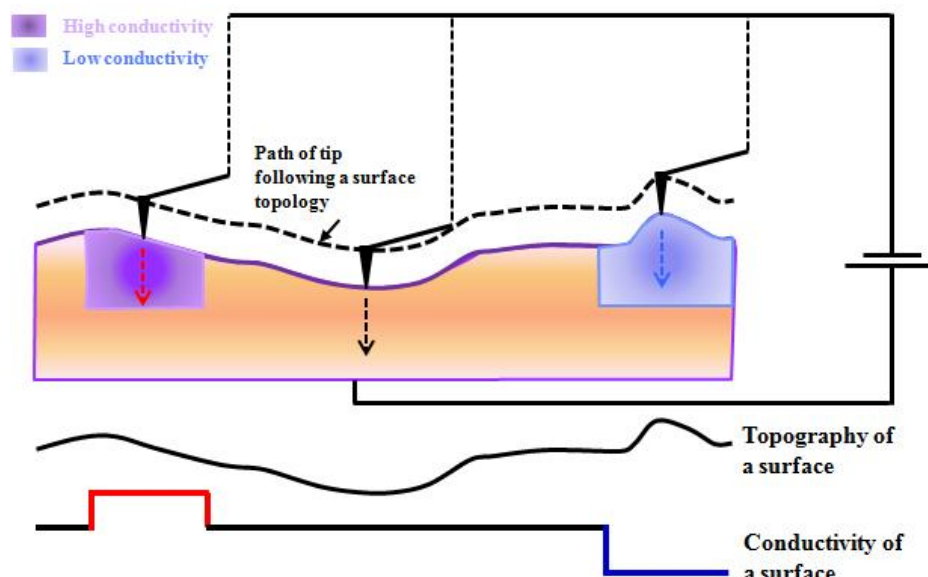


Figure 3.2.6 Schematic diagram for conducting AFM measurement. A conductive tip senses the different conductivity and detects current while scanning the surface of a sample.

### 3.2.5 Other characterization methods

Scanning Electron Microscopy (SEM) is a universal technique for studying surface topology and chemical composition of samples. A SEM system usually consists of an electron source emitted from a filament, a detector, and a vacuum vessel. The operation is based on electron interaction with the surface atoms where secondary and back-scattered electrons are emitted. The detector collects the emitted electrons to visualize images using analysis software. In this study, a JEOL-7000F FEG-SEM was used for observing the morphology and density of nanowires.

Reflection High Energy Electron Diffraction (RHEED) is a powerful technique to investigate the crystal structures of the surface of a sample during film growth. RHEED is especially used to characterize the diffraction (scatter) pattern on the surface owing to wavelike properties of electrons as described by quantum physics. The diffraction images help one determine the crystalline quality of the growing film and growth modes of films, such as layer-by-layer vs. island mode on a substrate. The RHEED system generally consists of an electron gun, a detector screen, and an ultra-clean sample. In principle, the electron gun operated in the range of 10 to 60keV generates electrons, which strike the sample at a low incident angle and the electrons diffract from the atoms at the surface of the sample. The diffracted electrons create a diffraction pattern on the detection screen. Fig. 3.2.7 shows the schematic of the RHEED system. A RHEED system equipped with a 30 KeV electron gun (Staib Instruments) was used to perform the in-situ growth characterization of thin films in our studies.

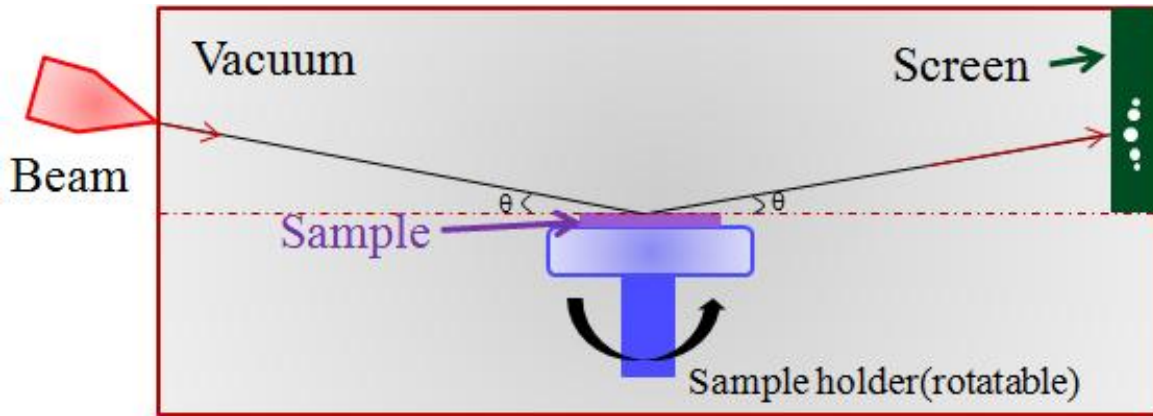


Figure 3.2.7 Schematic of the basic configuration of a RHEED system. An incident electron beam at a shallow angle is diffracted from the sample surface and projects diffraction patterns on the screen. A sample is placed in an ultrahigh vacuum vessel and can be rotated 360 degrees, leading to various diffraction patterns owing to different crystal orientations.

### 3.3 Review of selected materials

#### 3.3.1 Barium titanate ( $\text{BaTiO}_3$ , BTO)

The ferroelectric material barium titanate (BTO) has been studied quite extensively, both as bulk ceramic and thin films, with material synthesized using a variety of physical and chemical methods. BTO undergoes a series of phase transitions from cubic at high temperature to tetragonal below the Curie temperature of 410 K, orthorhombic below 390 K, and rhombohedral below 190 K. In these phase transformations, BTO exhibits ferroelectric property in the tetragonal phase with  $a = b = 3.99 \text{ \AA}$  and  $c = 4.04 \text{ \AA}$  at room temperature and paraelectric behavior in the cubic phase at high temperature [74]. The basic perovskite structure provides a fundamental understanding of ferroelectricity in BTO. Fig. 3.3.1 shows a schematic of the perovskite structure of BTO, in which the material is deformed from a cubic to a tetragonal structure by application of an applied electric field at room temperature.

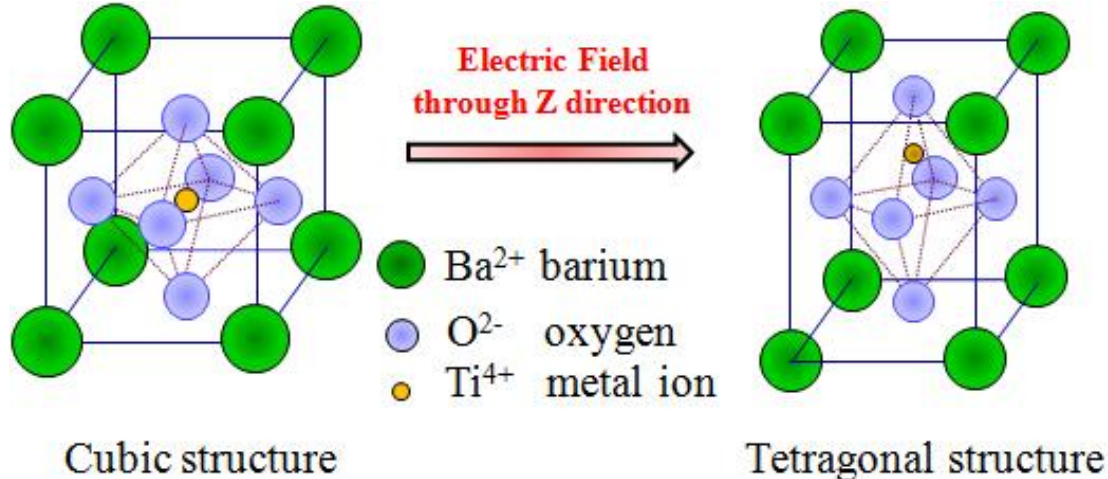


Figure 3.3.1 Schematic of  $\text{BaTiO}_3$  (BTO) crystal structure. The BTO material is deformed from cubic to tetragonal structure by an application of an applied electric field at room temperature.

In the perovskite structure, barium ( $\text{Ba}^{2+}$ ) ions occupy the unit cell corners and are surrounded by 12 nearest neighbor oxygen anions ( $\text{O}^{2-}$ ). The titanium ( $\text{Ti}^{4+}$ ) metal ion is positioned at the center of the structure and has six oxygen anions in octahedral coordination as seen in Fig. 3.3.1(a). When an electric field is applied, the off-center distortion of  $\text{Ti}^{4+}$  gives rise to an electron dipole and phase deformation follows as shown in Fig. 3.3.1(b). Through the structural transition, BTO exhibits a ferroelectric property with a remnant polarization of value of  $26\mu\text{C}/\text{cm}^2$  measured in single crystals.

### 3.3.2 Nickel ferrite ( $\text{NiFe}_2\text{O}_4$ , NFO)

Nickel ferrite (NFO) is a well-known insulating and high permeability magnetic material that is commonly used in transformer cores and microwave applications [75]. The material possesses a cubic structure ( $a=8.34 \text{ \AA}$ ) consisting of tetrahedral 'A' sites whose corners are occupied by oxygen ions and octahedral 'B' sites in which oxygen ions occupy the corners of an octahedron. Fig. 3.3.2 illustrates the structure in the inverse spinel where divalent ions occupy

the 'B' site and trivalent ions are equally split between 'A' and 'B' sites. The net magnetization ( $2\mu_B/\text{f.u.}$  or  $300\text{emu}/\text{cm}^3$ ) in this material is due to the existence of two magnetic sublattices that results in ferrimagnetic behavior.

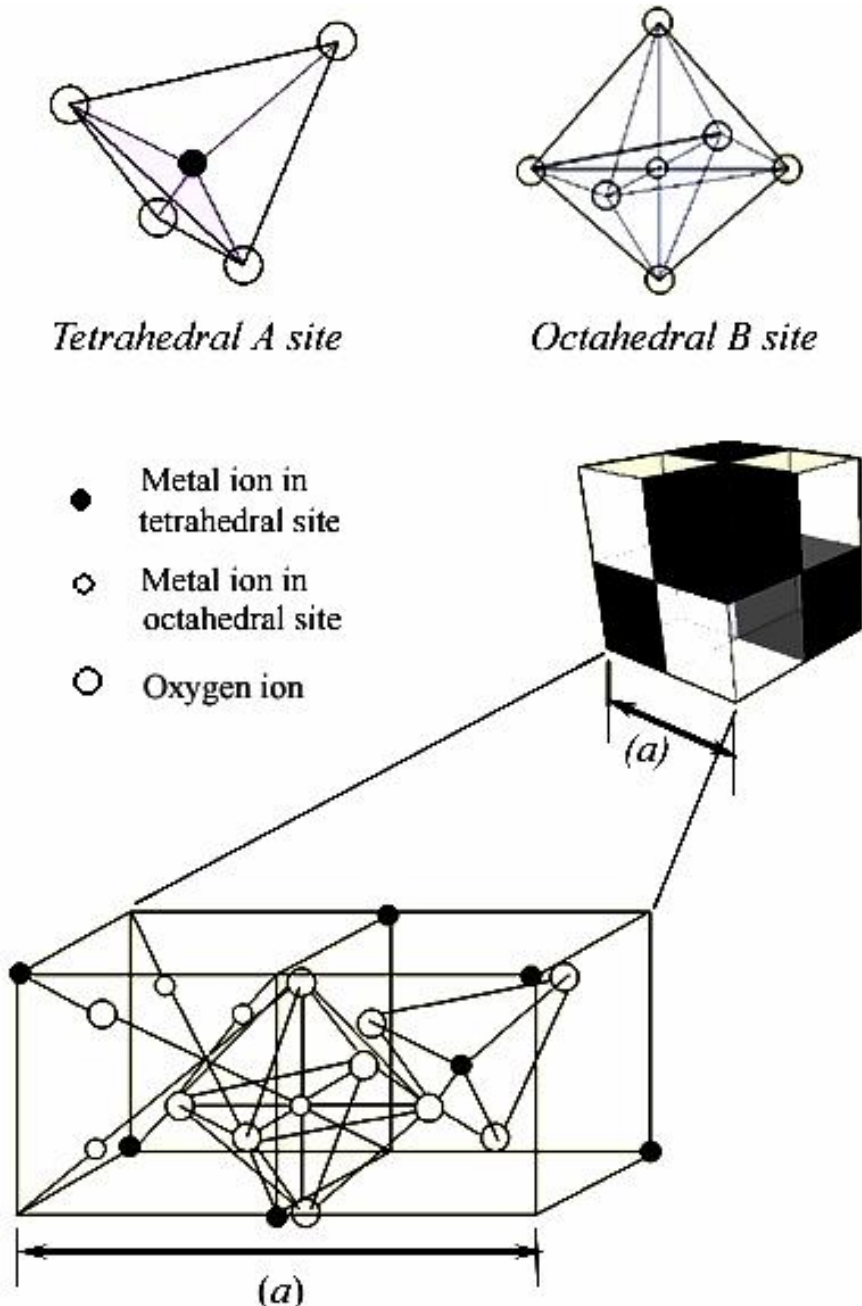


Figure 3.3.2 Schematic of inverse spinel  $\text{NiFe}_2\text{O}_4$  structure consisting of 'tetrahedral A' sites and 'octahedral B' sites. The cubic structure is configured by combining these two sites in a FCC oxygen lattice (Adapted from ref. [37]).

### 3.3.3 Lanthanum strontium manganite ( $\text{LaSrMnO}_3$ , LSMO)

$\text{LaSrMnO}_3$  (LSMO) is a half-metallic ferromagnetic material and has a pseudocubic perovskite structure with lattice parameters  $a=b=c=3.87$  Å. The general formula of the perovskite is  $\text{ABO}_3$ , where 'A' site is occupied La and Sr ions and 'B' site is occupied by Mn ions. The magnetic moment of LSMO is approximately 620 emu/cm<sup>3</sup> at low temperatures. Its half-metallic property allows for conduction of spin-polarized electrons. Therefore, LSMO is widely used a magnetic electrode in combination with an insulating space layer to configure a TMR system in spintronics [76].

## CHAPTER 4

### MAGNESIUM OXIDE (MgO) and MULTIFERROIC NANOWIRES (NWs)

Reproduced in part with permission from [G. Kim, R. L. Martens, G. B. Thompson, B. C. Kim, and A. Gupta, J. Appl. Phys., **102** 104906 2007]. Copyright [2012] American Physics Society.

#### 4.1 Introduction

We have grown single crystalline MgO nanowires (NWs) both on (001)-orientated single crystalline MgO and Silicon (Si) substrates. We selected magnesium oxide (MgO) because of its attractive features for use as the NW template, such as its thermal stability, chemical inertness, and excellent electrical insulating characteristics.

We employed two methods for nanowire growths: a high-density array and patterned arrays. The high density array of NWs is produced using a blanket gold thin film as a catalyst. However, the random placement of the NWs with the high density is a challenge for the subsequent functionalization and selective placement of the NWs. In contrast, array pattern formations, such as square cross-section and single dots, offer control over the density of NWs and have potential for device fabrication. For both the random arrangement and patterned array methods, a 1 nm thin gold film was electron-beam evaporated onto MgO and Si substrates. For patterning the gold layer, a positive resist (polymethyl methacrylate, PMMA) was spin-coated onto the substrate surface. The resist-coated layer was patterned in three different square arrays of dimension 0.25, 1, and 4  $\mu\text{m}^2$  by e-beam lithography. For single dot patterns, a negative e-beam resist (Fox-12) was spin-coated on a thin gold film deposited on silicon wafer then 10 x 10 arrays were patterned by lithography. Post-patterning, the substrates were ion milled to remove

the gold layer except the zone of patterned dot arrays. Final lift-off of the resist on the dots was accomplished using dilute HF (<1%). Afterwards, single gold dots remained, acting as catalyst for MgO nanowire growth.

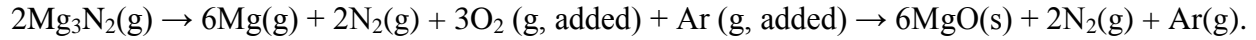
A good correlation was observed between the density, average diameter, and distribution of the NWs with those of the initial Au catalyst islands formed at the deposition temperature. Unlike growth with random orientations and sizes on Si, the wires grew vertically on MgO substrate and exhibited a more uniform size and shape distribution. The latter appear particularly promising for the selective growth of NWs in pre-patterned regions using electron beam lithography. As an ultimate objective, the MgO NWs were used as template posts to form core-shell NWs, BaTiO<sub>3</sub> or NiFe<sub>2</sub>O<sub>4</sub> coated nanowires. The successful coated BaTiO<sub>3</sub> or NiFe<sub>2</sub>O<sub>4</sub> nanowires propose an appearance of multiferroic nanowire heterostructures.

## 4.2 Random arrangement of NWs on MgO and Si substrates

### 4.2.1 Morphologies

The random array of gold nanoparticles generated on the surface of MgO and Si substrates upon heating, along with the subsequent growth of nanowires (NWs) on these surfaces, generates two distinct morphologies of NWs, as seen in Fig. 4.2.1. The NWs grow vertically off from the MgO substrate. In contrast, the NWs on the Si substrate form a ‘basket-weave’ like morphology, being intertwined and at various non-vertical growth directions. The inset images of Fig. 4.2.1 show the morphology and density of gold nanoparticles, which are formed from the ultrathin gold film and act as the catalyst for the vapor-liquid-solid (VLS) growth mechanism of the MgO NWs. These particles form a discontinuous array of semicircular-shaped nanometer-sized particles because of overall reduction of the surface tension at this high temperature. The average length of the MgO nanowire grown on MgO substrate is ~1 μm for a deposition period

of 60 minutes. On the other hand, the wires grown for the same time period on Si substrate are significantly longer. The overall reaction leading to the formation of the MgO nanowires from the precursor can be represented by the chemical reaction



The small added concentration of oxygen with the argon carrier gas is likely adsorbed on the surface of the gold catalyst and reacts with the magnesium vapor to form the initial nuclei that results in the growth of MgO NWs. For Si NWs, Kodambaka et al. [77] have reported that the ambient oxygen concentration reduces the gold diffusion along the sidewalls during growth process enabling the NW to grow longer and have an untapered geometry. On the other hand, Kazuki et al. [78], based on their MgO NW growth experiments using PLD, have suggested that the total ambient pressure (either argon or oxygen) and not the actual oxygen content which gets incorporated into the MgO wires is critical for enhancing the NW growth. Nonetheless, they observed that the oxygen concentration is critical for the degree of crystallinity of the MgO wires. The Au nanoparticle usually ‘rides’ atop the growing structure and its size remains essentially unchanged during the entire process of the wire growth, as has been previously observed in other VLS grown structures [79]. However, under non-optimal growth conditions, the gold catalyst can diffuse away during growth and the wire’s height can be shunted [80]. The SEM images of Fig. 4.2.1 show gold particles at the tip of the longer wires indicating limited gold catalyst diffusion away from the tip of the wire under our operating conditions. TEM images and diffraction patterns, shown in Fig. 4.2.2, indicate that the NWs have a rectangular cross-section with <001> growth direction. This growth direction is to be expected based upon the homoepitaxy between the MgO NW and the MgO (001) substrate at these processing temperatures.

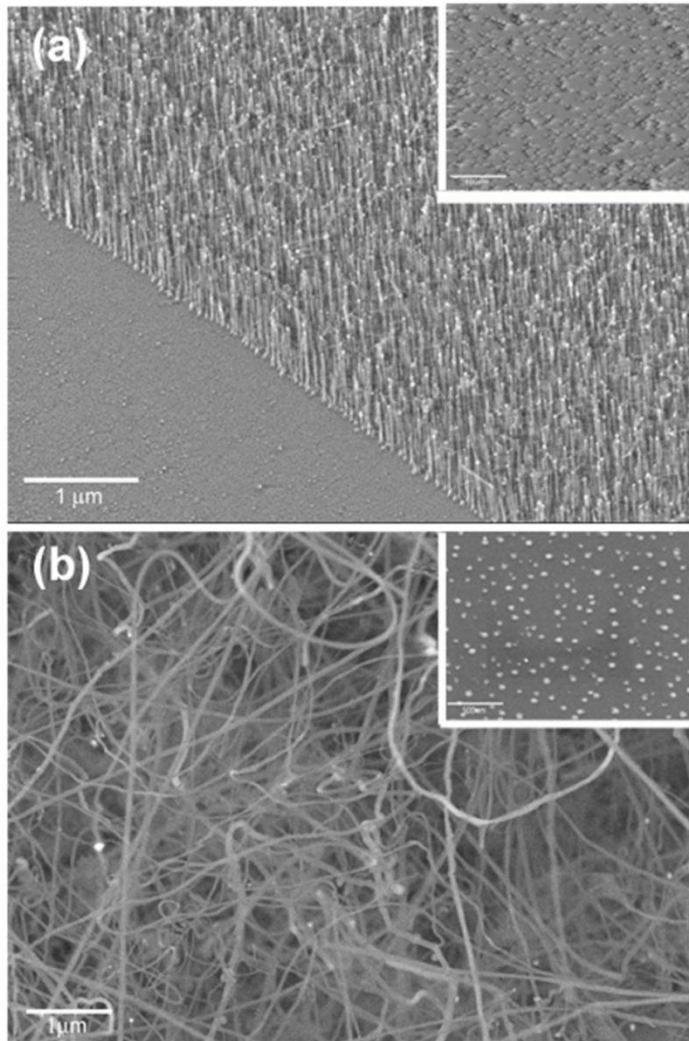


Figure 4.2.1 SEM images showing the growth of vertically aligned MgO nanowires on a (001)-oriented MgO substrate. The inset shows an image of the gold particles formed by heating the gold film on the MgO substrate to the growth temperature and then cooled down without actual growth of the nanowires. (b) SEM image showing MgO nanowires grown on a (001)-oriented Si substrate for a total deposition period of 60 minutes. The wires grow in random directions exhibiting a basket-weave-like morphology. The inset shows the gold particles formed by heating the gold film on the Si substrate to the growth temperature and then cooled down without actual growth of the nanowires. The marker for both inset images is 100 nm. (Reproduced with permission from ref. [81])

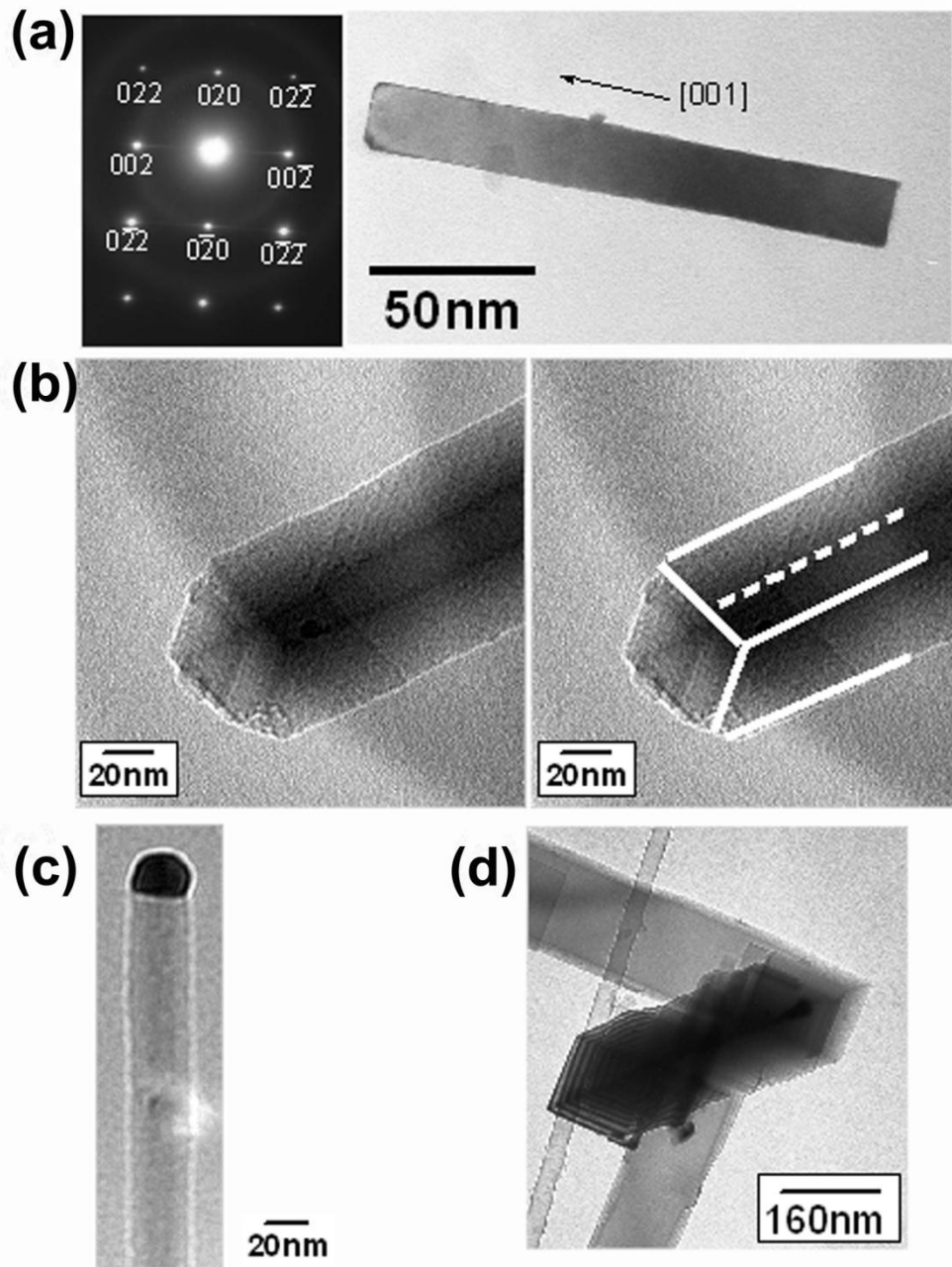


Figure 4.2.2 TEM diffraction pattern and bright field image of a single MgO nanowire grown on the MgO substrate indicating (001) growth direction. (b) MgO nanowire showing a cubic-rod shape morphology; the image to the right has the cube edges highlighted. (c) TEM bright field image of a MgO nanowire with the gold catalyst on top, which has been grown on an MgO substrate. (d) TEM bright field image of MgO nanowires grown on Si substrate. Note the rectangular shape of the nanowires and interconnection of the wires to each other in different directions. This type of interconnection is not evident in the MgO nanowires grown on the MgO substrate. (Reproduced with permission from ref. [81])

Unlike the MgO substrate, the nanowires are not epitaxially anchored onto the (001) Si substrate. Moreover, a pristine Si surface is not presented during the growth since the partial pressure of oxygen, particularly at these processing temperatures, will enhance the natural oxidation of the Si surface. As the MgO wires nucleate and grow in length, the lowest surface energy facets will dominate and preferentially grow in which every direction they are formed. All the NWs that we have imaged, grown to different heights and on different substrates, exhibit the square rod shape. In general, the {001} facets in rock-salt-crystals, such as MgO, have the lowest surface energy [82], allowing the wires to maintain the cubic shape facets perpendicular to the axial growth direction of the wires on MgO substrate. In contrast, since the nucleation of nanowires is not fixed to any particular direction from the Si substrate, as Colli et al. [83] have reported for ZnO nanowires on Si, they grow outwardly in multiple directions and develop the basket-weave morphology.

#### 4.2.2 Histograms of MgO NWs and gold nanoparticles

The cube-length of the rectangular nanowires, termed “diameter,” has been measured from the TEM images. A comparison of the wire diameters in Fig. 4.2.3 shows that the average diameter is  $19 \pm 5$  nm and  $29 \pm 13$  nm for the MgO and Si substrates, respectively. Additionally, the Si substrate shows a greater wire-to-wire diameter variability.

A histogram comparing the initial gold particle sizes between the two substrates is graphed in Fig. 4.2.4. The average gold particle diameters were found to be  $23 \pm 7$  nm and  $51 \pm 11$  nm and for the MgO and Si substrates, respectively. Similar to the wire variability, the Si substrate gold particles show a wider size distribution. This is likely due to differences in the surface tension between liquid Au-Si and liquid Au-MgO interface. Metal films grown on oxide surfaces are known to significantly ‘ball up’ because of the high surface tension [84].

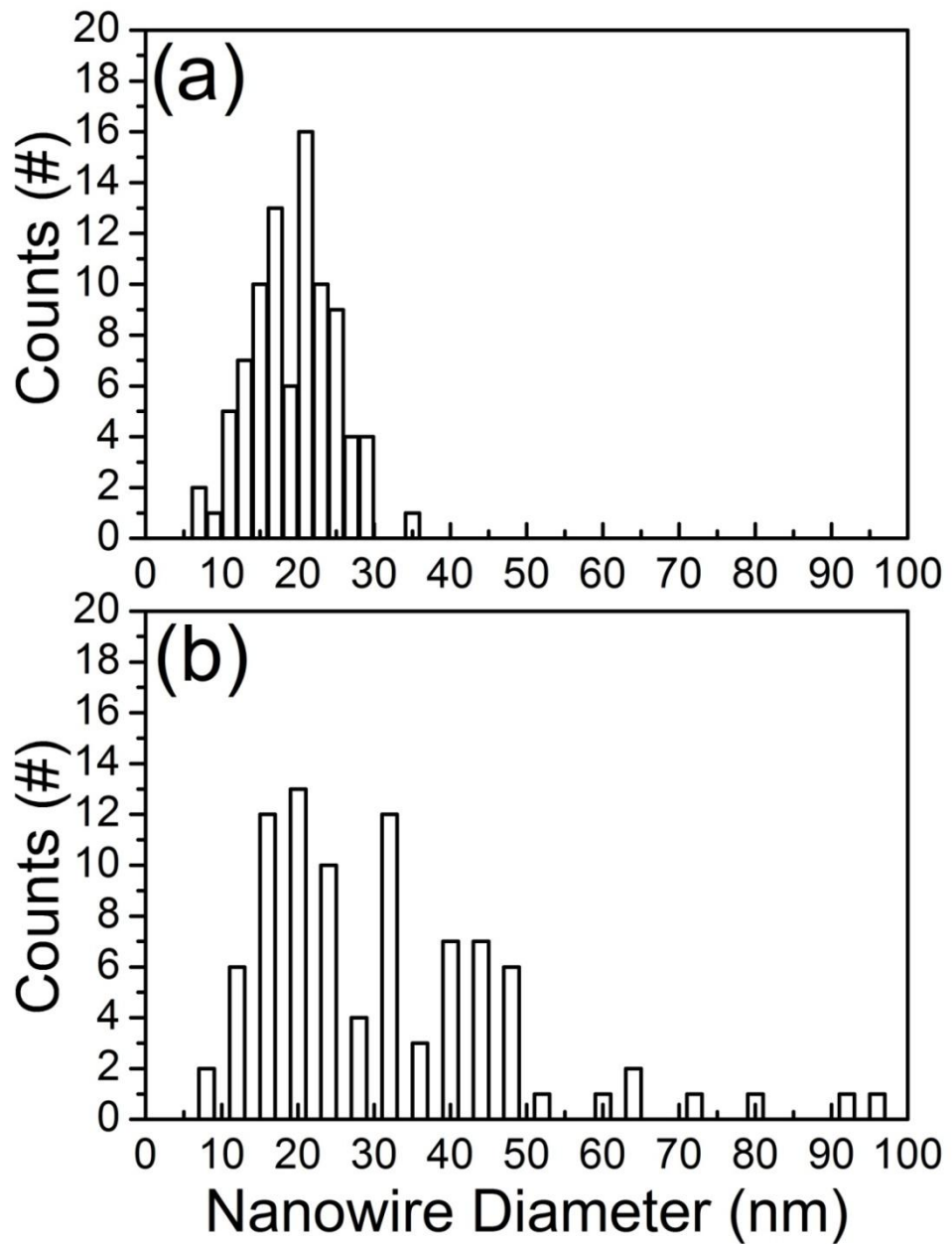


Figure 4.2.3 Histograms comparing the diameter of MgO nanowire grown on (a) MgO (001), and (b) Si (001) substrates. (Reproduced with permission from ref. [81])

By providing thermal energy, as in our growth process, the metal surface mobility is enhanced resulting in both the driving force and mobility to produce small metal particles on the oxide surface that have little variability in the contact angle. The larger average size and larger range of sizes of the gold catalysis particles invariably contribute to the variability in the wire diameters. Additionally, the random basket-weave morphology of the nanowires on Si substrate will hinder uniform growth because of the tortuous diffusion path for transporting the precursors to the growing wires. Collectively, this will contribute to different growth rates for each wire depending upon its location. In contrast, the nearly uniform gold catalyst particle sizes and vertical growth direction of the wires from the MgO substrate provide for more consistent growth conditions and reduced variability in the final wire size. Additionally, for MgO substrate wires, there is no appreciable diameter variation along the  $\sim 1\mu\text{m}$  axial length of the wires. Based on the random array results, we have ruled out Si as an adequate substrate for selectively patterning well-ordered nanowire arrays. The selective patterning has thus only been performed on the MgO (100) substrates.

#### 4.3 Systematic pattern array of MgO NWs on MgO substrate

##### 4.3.1 Square cross-section pattern

A series of gold catalysis regions have been selectively patterned into different regions of 0.25, 1, and  $4\mu\text{m}^2$ . The SEM images, shown in Fig. 4.3.1 (a), (b) and (c), depict different number of freestanding MgO nanowires grown in the various gold pattern regions, respectively. The regions over which the wires grow are approximately 50% larger than the initially patterned square areas. At  $925^\circ\text{C}$ , the liquid-like gold layer has enhanced mobility and is likely to spread out and extend beyond the patterned areas. The density of nanowires at each patterned area is typically in the range of 200 - 250 per  $\mu\text{m}^2$ .

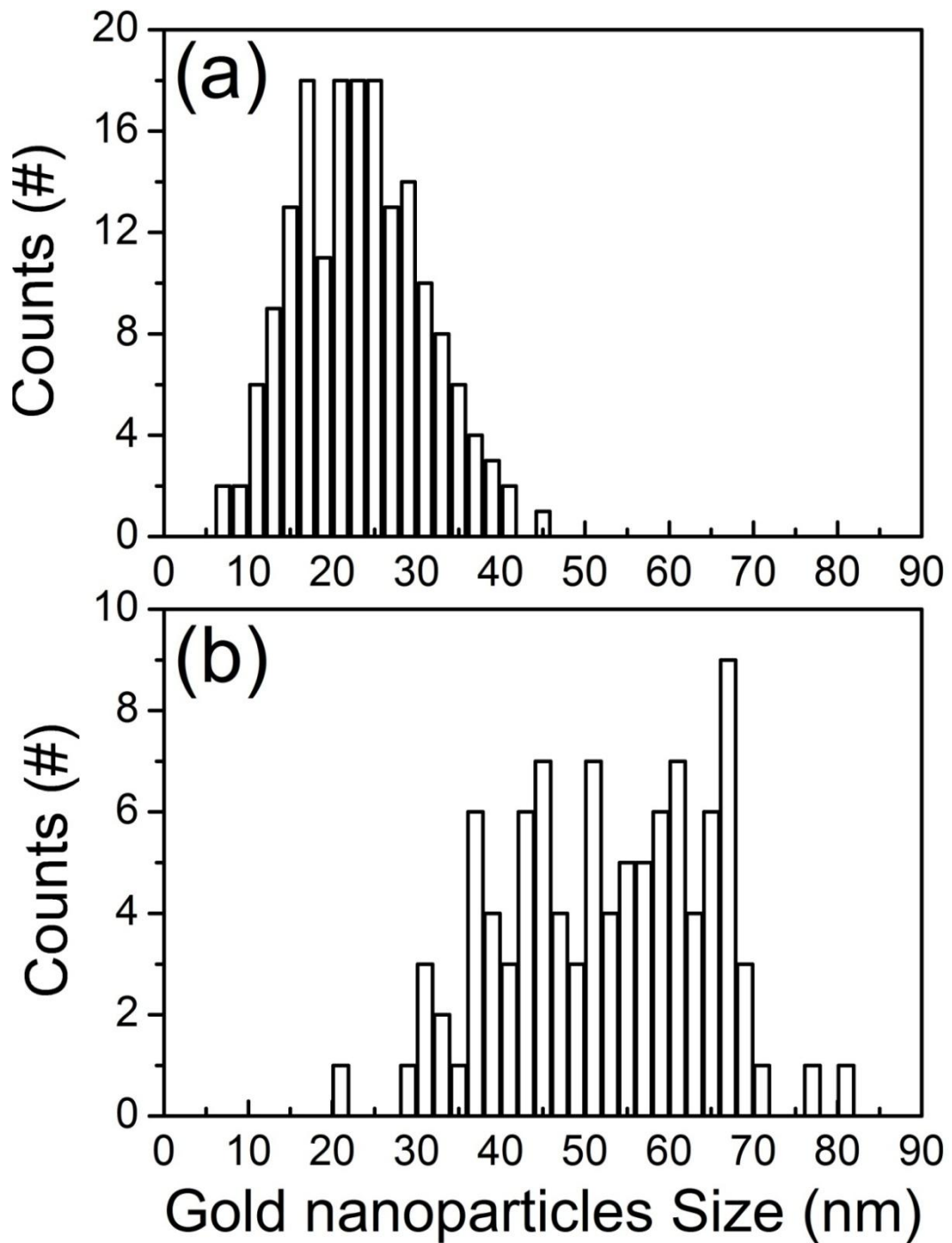


Figure 4.2.4 Histograms comparing the size of gold nanoparticles formed using a 1 nm thick gold film on (a) MgO (001) and (b) Si (001) substrates. (Reproduced with permission from ref. [81])

A histogram comparing the gold nanoparticles sizes formed at the reaction temperature in patterned regions of  $1 \mu\text{m}^2$  is shown in Fig. 4.3.2 (measured at room temperature).

The properties of patterned nanowires are summarized in Table 4.3.1. For each patterned region, the wires exhibit fairly good uniformity in both size and quantity. Additionally, changing the size of the pattern area does not appear to dramatically alter the wires sizes or packing density between the different regions studied. The abilities to selectively pattern wires into specific locations and control the shape, size and density provide the capability to functionalize and manipulate these structures for the fabrication of nanoscale devices.

#### 4.3.2 Single dot pattern

Single free-standing MgO NWs were grown in  $10 \times 10$  dot arrays. In order to carry out this synthesis, e-beam lithography was used to prepare a pre-patterned dot array as seen in SEM image of Fig. 4.3.3(a). Here, each dot size is approximately 200 nm in diameter. Single MgO NWs were grown on the gold dot arrays as seen in Fig. 4.3.3(b). The height of NWs is approximately 5-10  $\mu\text{m}$  and the distance between wires is 1  $\mu\text{m}$ . Since the dot size diameter is bigger than the radius of NWs, two or three NWs were grown within the same gold dot zone in some case. However, our work clearly demonstrates that single vertically arrayed MgO NW can in principle be synthesized at specifically selective points or regions. Thus, this technique appears suitable for well-controlled growth of NWs both in terms of their position and density. This is important to avoid shadowing effect during film deposition on the NWs and provide excellent uniformity and control of a sheath thickness.

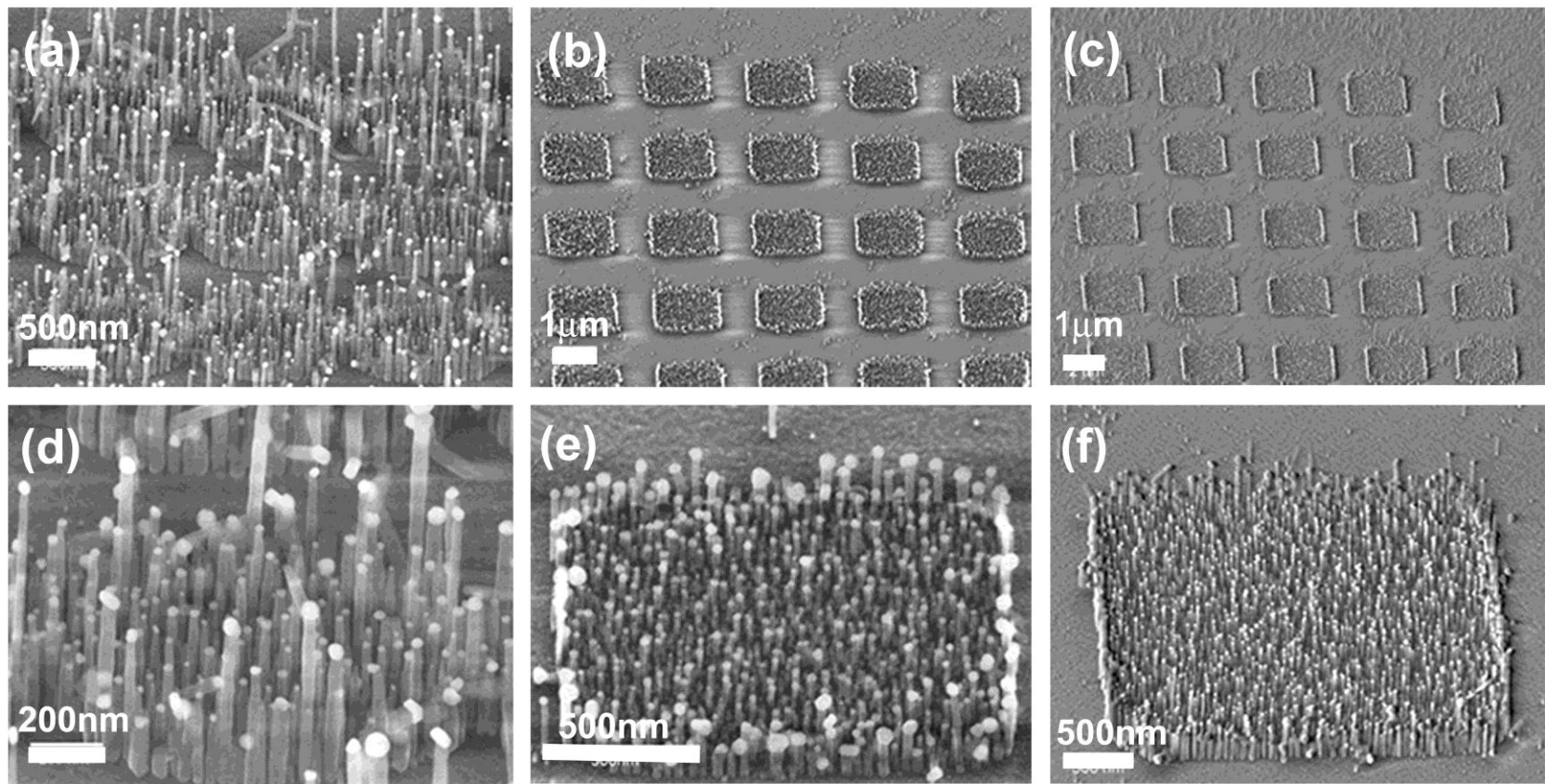


Figure 4.3.1 SEM images showing different patterned regions of the MgO nanowires. The bright spot on the top of each nanowire is the gold catalyst particle. [(a) and (d)]  $0.25\mu\text{m}^2$ , [(b) and (e)]  $1\mu\text{m}^2$ , and [(c) and (f)]  $4\mu\text{m}^2$ . A blanket gold film of 1 nm thickness is deposited and patterned using e-beam lithography for the selective growth of the nanowires. (Reproduced with permission from ref. [81])

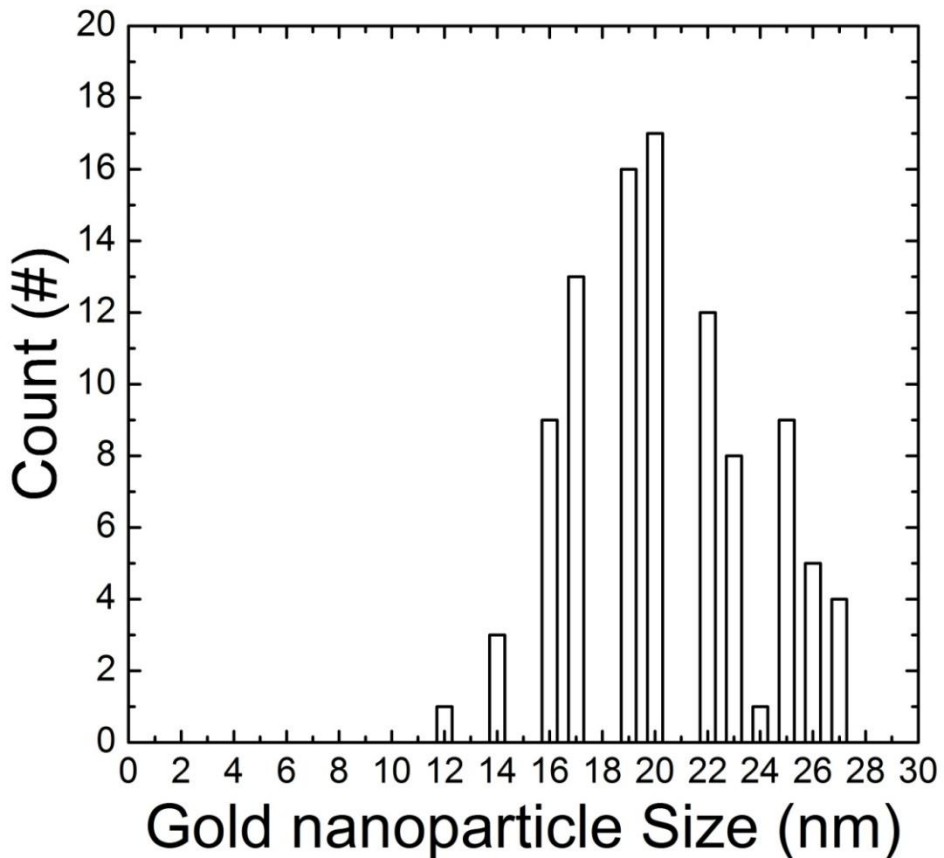


Figure 4.3.2 Histogram of the size distribution of gold nanoparticles formed within the  $1\mu\text{m}^2$  patterned regions on an MgO (001) substrate. The average nanoparticle size is 20 nm. (Reproduced with permission from ref. [81])

TABLE 4.3.1 Tabulation of the absolute number and density of the grown nanowires at different patterned area, along with the number of gold catalyst particles formed at the growth temperature. (Reproduced with permission from ref. [81])

Measurement Square area ( $\mu\text{m}^2$ )	0.55	1.5	6.4
Number of nanowires	124	297	1092
Density of nanowires ( $\mu\text{m}^{-2}$ )	225	198	170
Size of gold nanoparticles (nm)	$19\pm4.9$	$20.4\pm7.2$	$18.4\pm4.2$

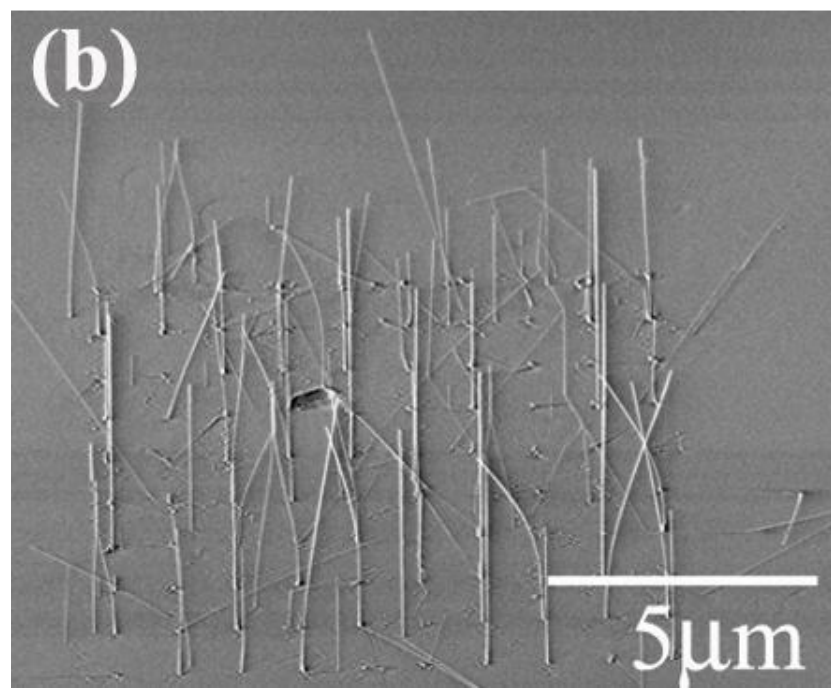
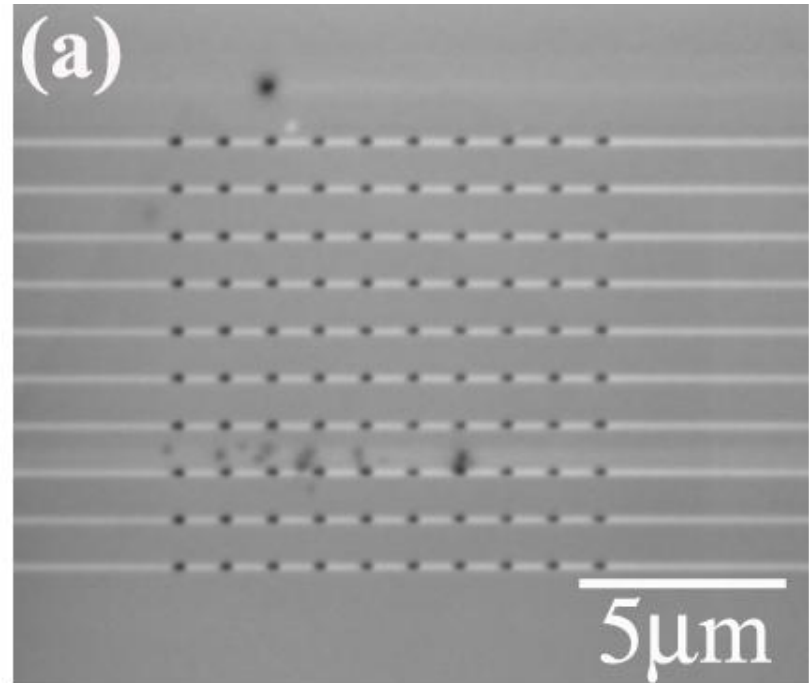


Figure 4.3.3 SEM images of a single MgO NW (a) Gold dot pattern in 10 x10 arrays. The diameter of dots is approximately 200 nm. (b) Single MgO NW grown within each dot array. The height is around 5-10 μm.

#### 4.4 Multiferroic nanowires

Bilayer BaTiO<sub>3</sub> (BTO) and NiFe<sub>2</sub>O<sub>4</sub> (NFO) films deposited on the MgO nanowires can be used as a multiferroic composite with significantly reduced clamping effect as compared to 2D structures. Fig. 4.4.1 illustrates the fundamental concept to form the multiferroic NW composite. Vertical free-standing MgO NWs are initially synthesized as shown schematically in Fig. 4.4.1(a). The pulsed laser deposition (PLD) technique deposits binary thin coatings on to the MgO NWs as shown in Fig. 4.4.1 (b)-(c), where a ferroelectric sheath layer is deposited on the initial ferrite layer. Fig. 4.4.1 (d) shows a cross section of the multiferroic NW. In order to synthesize the coaxially coated multiferroic nanostructures, we have used isolated MgO NWs grown on MgO substrate as templates because of the high thermal stability, lattice match, chemical compatibility, and vertical growth.

Prior to fabricating coaxially-coated NWs, thin BTO or NFO films were deposited as two-dimensional (2-D) structures via PLD. We selected these two materials because of their excellent lattice match with MgO, as shown in table 4. 4.1. The grown films were characterized using Philips X'Per XRD to determine their crystallinity and RHEED for *in situ* monitoring the film growth mode in a real time. The results are promising for the successful film growth on the template MgO NWs to form multiferroic nanowires.

TABLE 4.4.1 Lattice parameter ( $a$ ) and lattice mismatches (%) for each material.

Lattice parameter (Å)			Lattice mismatch $\Delta a/a$ (%)	
MgO	NiFe <sub>2</sub> O <sub>4</sub>	BaTiO <sub>3</sub>	NiFe <sub>2</sub> O <sub>4</sub>	BaTiO <sub>3</sub>
4.2	8.34	3.99	-0.7	-5

$\Delta a/a = (a_{film} - a_{sub})/a_{sub}$  [ $a_{sub}$  is bulk lattice parameter, '-' tensile strain]

Based on the preliminary results of two-dimensional thin films, BTO or NFO coated on MgO NWs (named BTO or NFO NWs) were synthesized. The coated single-phase NWs were characterized using SEM and TEM for investigating their microscopic and crystallographic properties.

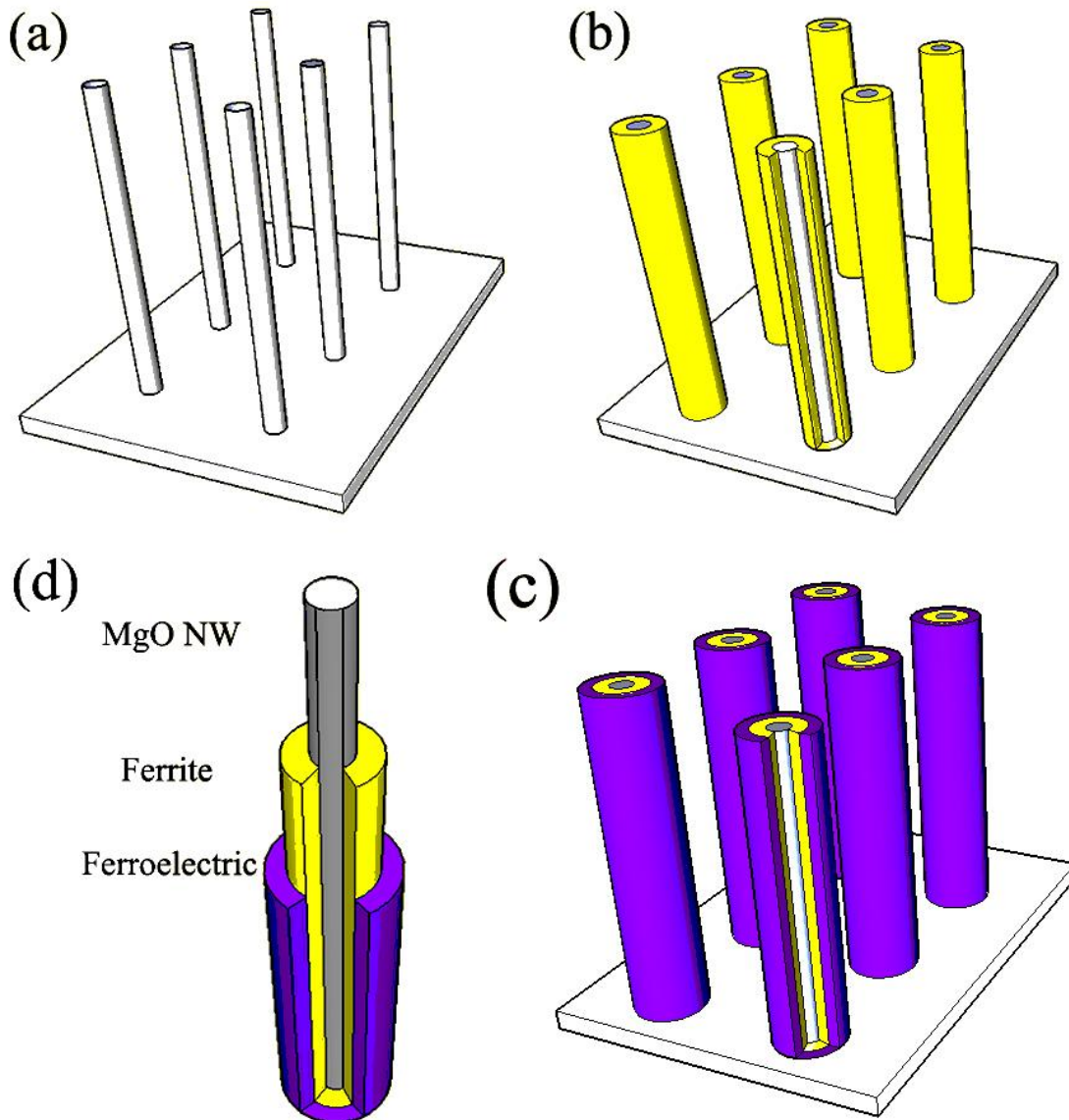


Figure 4.4.1 Schematic of multiferroic nanowire. (a) Template MgO NWs produced by VLS growth mechanism in a typical CVD process. NWs are vertically oriented. (b)-(c) ‘core-shell’ type multiferroic nanowire consisting of ferrite (yellow)-ferroelectric (purple) thin film deposited on the template post of MgO NW by PLD technique. (d) Cross section view of the multiferroic nanowire.

#### 4.4.1 Thin BaTiO<sub>3</sub> and NiFe<sub>2</sub>O<sub>4</sub> films

X-ray diffraction (XRD) measurements, including  $\theta$ - $2\theta$  scans, rocking curve, and pole-figure, were carried out to characterize crystallinity of the 2-D thin films. Fig. 4.4.2(a) shows XRD  $\theta$ - $2\theta$  scans of single-phase NFO and BTO film grown on MgO substrate. The peak position for the BTO film is very close to that for bulk BTO, with a slight shift to the left of the bulk value (somewhat larger out-of-plane lattice parameter). Thus, the BTO film is essentially relaxed. In contrast, the peak position of NFO film shows a significant shift to the right of the bulk value (smaller out-of-plane lattice parameter), indicating an in-plane tensile strain. Rocking curves in Fig. 4.4.2(b) show narrow curves for both BTO and NFO film, indicating excellent crystallinity. The full-width-half-maximum (FWHMs) values are  $0.03^\circ$  and  $0.038^\circ$ , respectively.

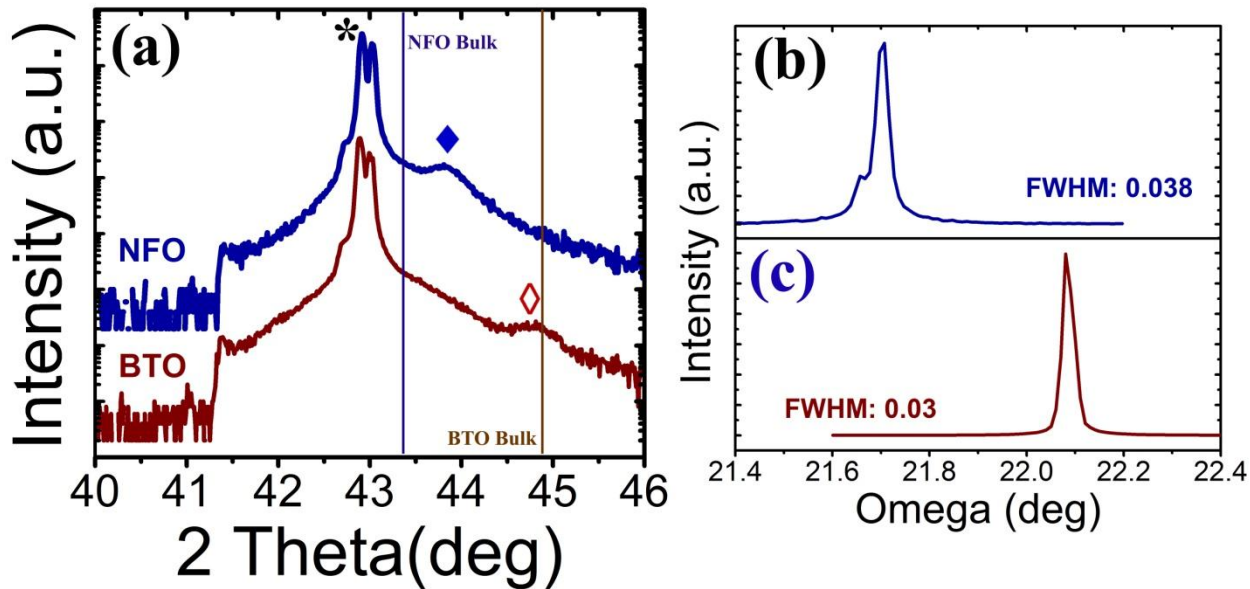


Fig. 4.4.2  $\theta$ - $2\theta$  X-ray diffraction spectra for a single-phase NFO and BTO film on MgO substrate. Peaks are close to the angular positions of the (004) and the (002) reflection of NFO and BTO. (b)-(c) Rocking curves for NFO and BTO films. The vertical solid lines indicate the bulk NFO and BTO  $2\theta$  peak positions. Here, makers, \*, ♦, and ◊, indicate MgO bulk peak, NFO and BTO film peaks.

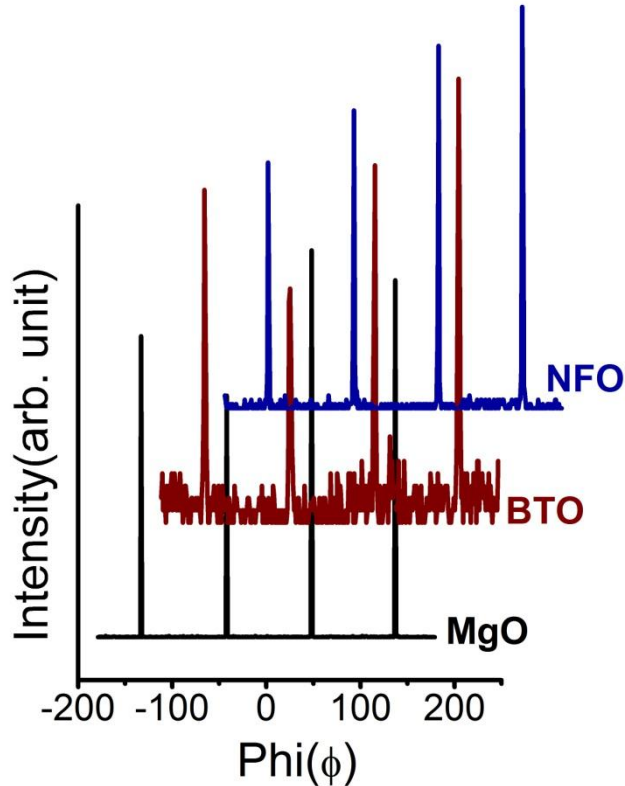


Figure 4.4.3 Phi  $\phi$  scans of (311) reflection of bilayers of NFO and BTO films on MgO. Four symmetric peaks spaced 90 degrees apart are observed.

X-ray Phi scans ( $\phi$ ) were carried out on the off-axis (001) and (311) plane of the films.

Fig. 4.3.3(a) and (b) show the peaks with four-fold symmetry of both the films grown on MgO. The peaks show the same azimuthal  $\phi$  angle, being 90 degrees apart, indicating cube-on-cube growth.

RHEED was used to *in-situ* monitor the crystallinity and initial growth mode of films in real time during PLD deposition. Fig. 4.3.4(a) shows well-defined lattice rods of MgO substrate prior to deposition, displaying a perfect single crystal structure. Fig. 4.3.4(b) and (c) show RHEED patterns of BTO and NFO film grown on MgO substrate. Remarkably streaky RHEED patterns are observed, revealing excellent single crystal structure of both films.

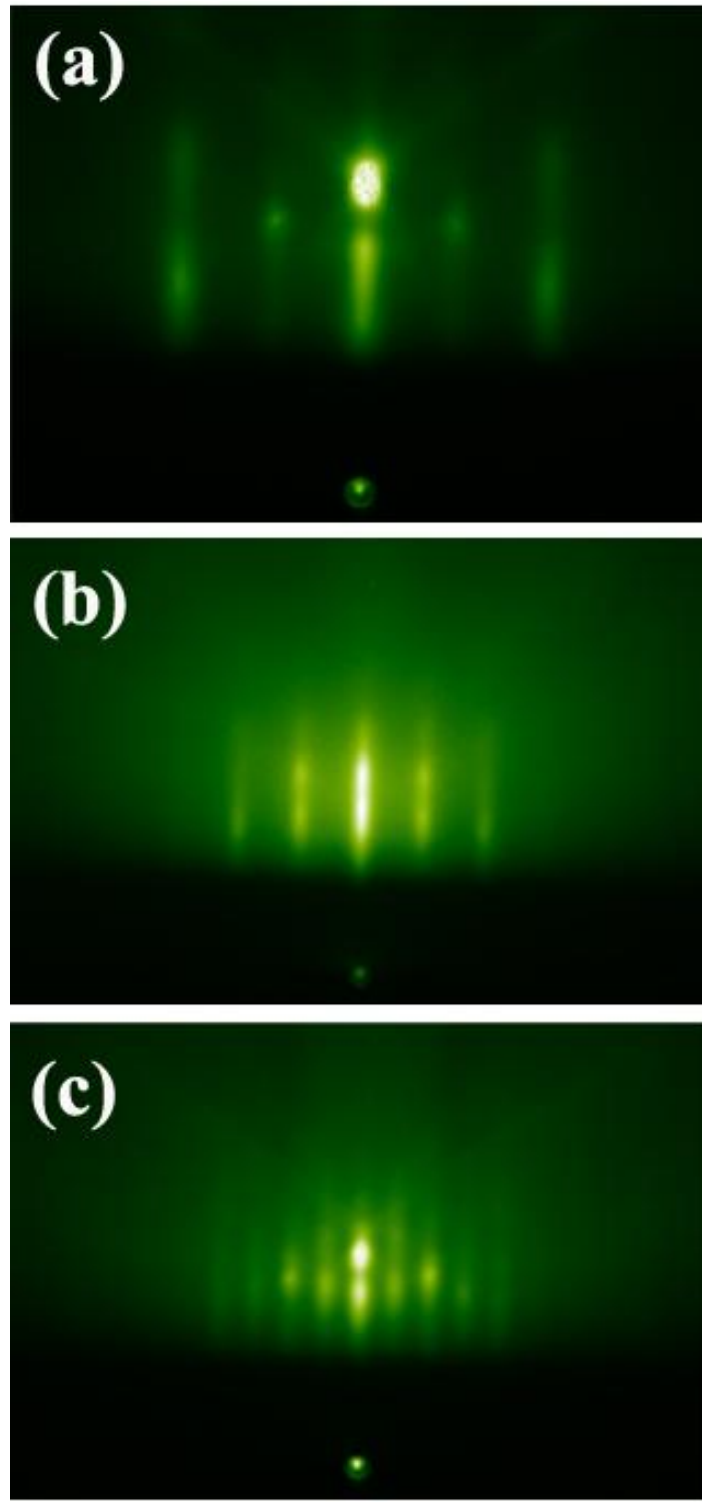


Figure 4.4.4 RHEED patterns along [100] for epitaxial growth of BTO and NFO thin films on (100)-oriented MgO substrate. (a) RHEED image of MgO substrate prior to deposition. (b)-(c) RHEED image of BTO and NFO films.

#### 4.4.2 Single phase BaTiO<sub>3</sub> or NiFe<sub>2</sub>O<sub>4</sub> coated NWs

Ferroelectric or ferromagnetic coated BTO and NFO NWs were characterized using SEM and TEM. The SEM images of template MgO, BTO and NFO NWs are shown in Fig. 4.4.5. The MgO NWs with gold balls on top of the NWs are clearly observed, as seen in Fig. 4.4.5(a) where the NWs are free standing and well separated. In addition, SEM images of coated BTO and NFO NWs are shown in Fig. 4.4.5 (b)-(c). The images clearly show thicker BTO or NFO-coated NWs than the initial MgO NWs and bright contrast because of electron charging effect from the coated NWs, which are insulators.

For investigating the morphologic properties of BTO-coated NWs, TEM characterization was performed. Fig. 4.4.6(a) shows the bright field TEM image of a single BTO NW that is 10  $\mu\text{m}$  in length and 150 nm in diameter. The insert image shows the diffraction pattern of the BTO, indicating a well ordered crystalline structure. The geometry of BTO-coated NW is cubic rod-shaped as shown in Fig. 4.3.6(b). The shape is expected based on the epitaxy relationship with the initial MgO nanowire. The shape also reveals that conformal coating by PLD occurs on the template MgO nanowire. High resolution TEM (HRTEM) images in Fig. 4.4.6(c) shows a highly ordered heterostructure, with <001> growth direction and good crystallization with lattice spacings of 3.98 Å and 4.2 Å. These spacings correspond to the distance between the (001) planes of BTO and the MgO NW, respectively. This provides further evidence of the heteroepitaxial growth of BTO on the template MgO NWs. The drawn white lines clearly demarcate the boundary between MgO and BTO. Excellent lattice stacking and no defects are observed at the interface of BTO and MgO. Energy dispersive x-ray spectroscopy (EDS) analysis clearly shows Ba, Ti, Mg, and O, as shown in Fig. 4.4.6(d), confirming successful growth of coated BTO-NWs.

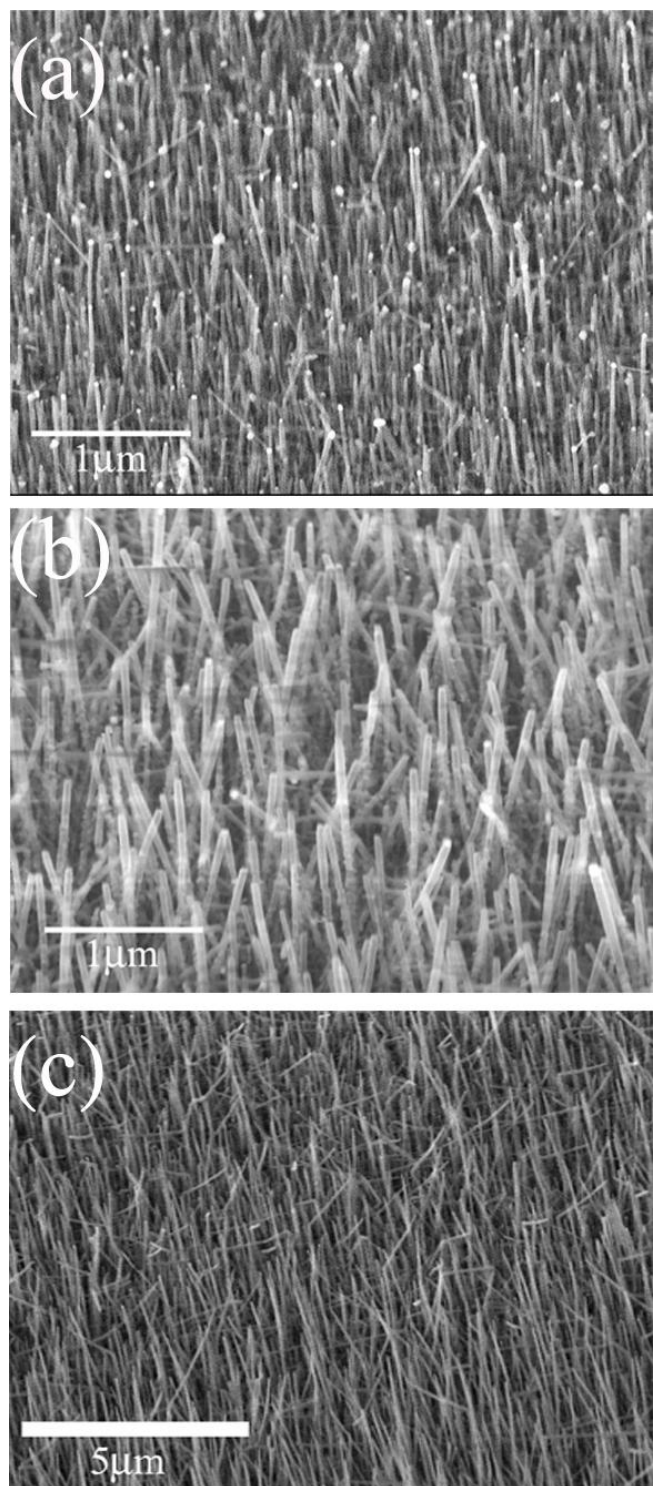


Figure 4.4.5 SEM images of nanowires. (a) Template MgO NWs. Gold balls lifted up and positioned on top of MgO NWs during a growth. (b) Single-phase BTO NWs. (c) Single-phase NFO NWs.

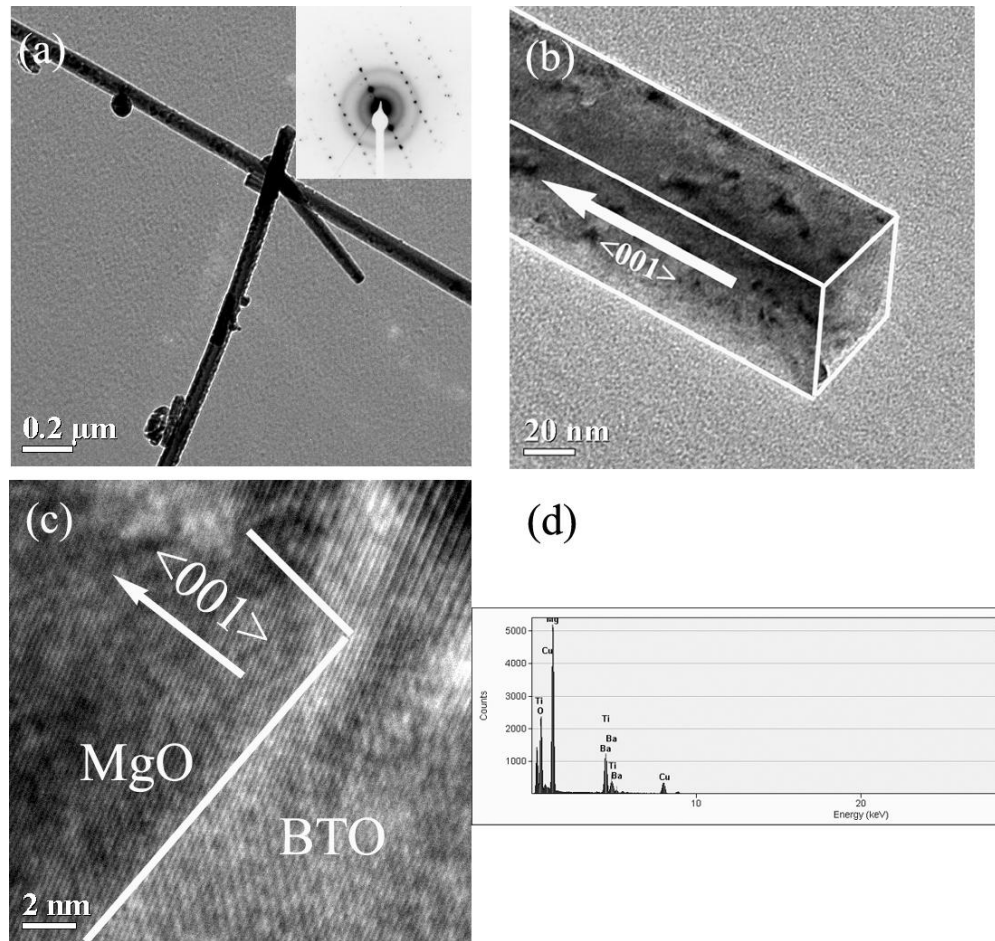


Figure 4.4.6 TEM images of  $\text{BaTiO}_3$  NWs. (a) Bright field TEM image showing single-BTO NW. Insert image shows a diffraction pattern, indicating well crystallized structure. (b) BTO NW has a cubic structure and  $<001>$  growth direction same as the template MgO. (c) HRTEM images displaying lattice spacing at the boundary of MgO and BTO layers. (d) EDS analysis indicates presence of Ba, Ti, Mg, and O.

TEM characterization was also performed on the NFO-coated NWs. Fig. 4.4.7(a) shows a bright field image of NFO-coated NWs. The insert image shows the diffraction pattern of the NW, revealing a well-ordered and crystalline structure. The NFO-coated NWs have cubic rod shape morphology as shown in Fig. 4.4.7(b), which is similar to the BTO-coated NWs. A high-resolution TEM (HRTEM) image in Fig. 4.4.7(c) shows an ordered heterostructure of NFO NW, indicating good crystallinity with lattice spacing of about 4.2 Å. The boundary of NFO and MgO is not very clear because of the similar lattice parameters. The growth direction of NFO-coated NW is [001], the same as the direction of template MgO NWs, revealing heteroepitaxial growth of NFO. Energy dispersive x-ray spectroscopy (EDS) analysis clearly shows Ni, presence of Ni, Fe, Mg, and O, shown in Fig. 4.4.6(d), confirming the successfully coating of NFO on the MgO template NWs. The successful growth of single-phase BTO and NFO coating on MgO NWs shows promise for synthesizing binary NFO/BTO multiferroic heterostructures using PLD.

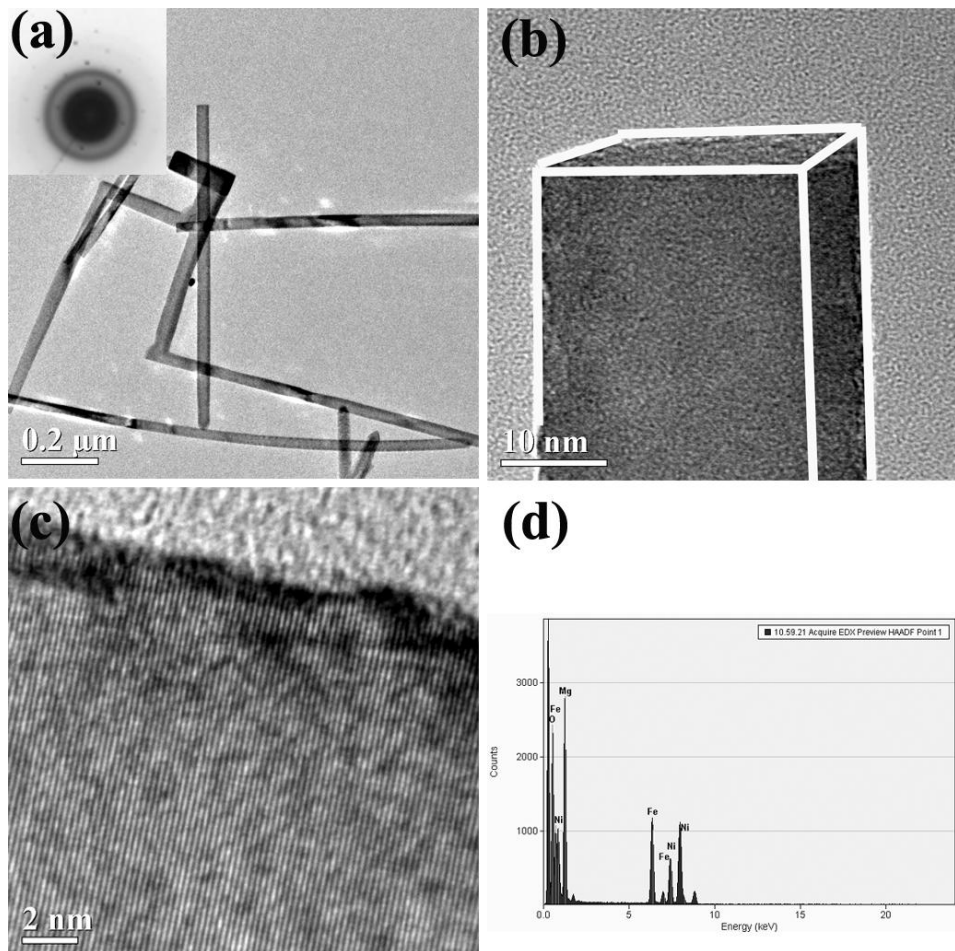


Fig. 4.4.7 TEM images of  $\text{NiFe}_2\text{O}_4$  NWs. (a) Bright field TEM image showing single-NFO NW. Insert image shows a diffraction pattern, indicating well crystallized structure. (b) NFO NW has a cubic structure and  $<001>$  growth direction, same as the template  $\text{MgO}$ . (c) HRTEM image displaying lattice spacing of  $\text{MgO}$  and NFO layers. The lattice spacings cannot be resolved because  $\text{MgO}$  and NFO are isostructural with very similar lattice parameters. (d) EDS analysis indicates presence of Ni, Fe, Mg, and O.

#### 4.5 Summary

MgO NWs have been successfully synthesized using the VLS method. Depending on the substrate and placement of the Au catalyst, the nanowires can have uniform diameter and display position-controlled growth. The size variability of the NWs can be directly correlated with the variability in the size of the gold catalyst particles and the extent of uniformity in the growth morphology. The MgO NWs grow homoepitaxially normal to the MgO substrate, whereas the wires grown on the Si substrate exhibit a variety of different growth directions even though they are all single crystalline. On both MgO and Si, the nanowires exhibit a <001> growth direction, as determined using TEM. Using e-beam lithography, selective synthesis of MgO NWs in square cross-sections has been achieved with control on both the size and density of the wires. Upon annealing the patterned gold film to the growth temperature of the wires, the patterned regions expand beyond the original dimensions but reasonably maintain the original shape. In addition, vertically free standing single MgO NW arrays were successfully grown. The patterning and growth of MgO NWs with control on their placement is attractive for their use as template posts for functionalization and for device fabrication and integration. Single-phase BTO and NFO-coated NWs were fabricated by coating the template MgO NWs. The successful growth promises the binary-coated NW formation, which is going to be a prototypical structure of multiferroic nanowire. Detailed process set up and understanding of the multiferroic NWs remain a future research task.

## CHAPTER 5

### NANOSCALE ELECTRORESISTANCE PROPERTIES OF ALL-OXIDE MAGNETO-ELECTRIC TUNNEL JUNCTION WITH ULTRA-THIN BARIUM TITANATE BARRIER

Reproduced in part with permission from [Applied Physics Letters], submitted for publication.  
Unpublished work copyright [2012] American Physics Society.

#### 5.1 Introduction

Magnetoelectric and Multiferroic Tunnel Junctions (METJs and MFTJs) are an emerging paradigm for device applications [85]. They provide the basis for a new class of solid-state memory devices, which are non-volatile and both electrically and magnetically tunable, and sometimes referred to as magnetoelectric random access memory (MERAM) devices. Fundamentally, METJs combine both tunnel electroresistance (TER) and tunnel magnetoresistance (TMR) effects [13, 15]. While room-temperature TMR effect has been known for almost 20 years, TER effect has only been recently reported, thanks largely to advances in oxide thin-film growth. A giant TER effect was demonstrated on highly strained BaTiO<sub>3</sub> (BTO) barrier layers deposited on thin ferromagnetic La<sub>0.67</sub>Sr<sub>0.33</sub>MnO<sub>3</sub> (LSMO) or SrRuO<sub>3</sub> (SRO) electrode layers [86, 87]. A tunnel effect by current (*I*)-voltage (*V*) measurements were equally presented to exhibit a resistance switching by the polarization directions. Similar results were also reported for BiFeO<sub>3</sub> (BFO) and PbTiO<sub>3</sub> (PTO) [19, 88]. All these experiments verify the earlier theoretical prediction of the TER effect [18, 32, 89]. More recently, proof-of-concept METJ devices have been successfully demonstrated at low temperatures [ref. 86]. These findings

have resolved, or at least alleviated, some of the longstanding concerns about the applicability of ferroelectric materials in devices requiring ultra-thin layers.

To integrate the METJ, such heterostructures consist of an ultrathin ferroelectric or multiferroic material as the active tunneling barrier sandwiched between ferromagnetic electrodes. Here, an ultrathin ferroelectric film of a few unit cell thicknesses is required for the active tunneling barrier; otherwise there is no tunnel current across the barrier because of the scattering effect of carriers. The challenge is to fabricate ultrathin films that retain the robust ferroelectric properties because of the critical thickness limitation, losing the ferroelectric property due to the depolarization by a reverse behavior below the critical thickness [33].

In this study, we investigated the thin-film heterostructure prototype consisting of ultrathin ferroelectric BaTiO<sub>3</sub> (BTO) and ferromagnetic La<sub>0.67</sub>Sr<sub>0.33</sub>MnO<sub>3</sub> (LSMO). We have quantified nanoscale ferroelectric and transport properties of this METJ prototype by using scanning probe microscopy techniques. Through local *I-V* measurements we demonstrate robust TER effect in ultra-thin BTO tunnel barriers of only 1.2 nm thickness, which is thinner than the calculated critical BTO film thickness (2.4 nm) [90]. Combined with earlier experimental reports [87, 91], we show that METJs have the ability to scale down (i.e., retain their functionality) to a level that current spintronics devices can offer.

The La<sub>0.67</sub>Sr<sub>0.33</sub>MnO<sub>3</sub>/BaTiO<sub>3</sub> (LSMO/BTO) heterostructures were deposited on (001)-oriented SrTiO<sub>3</sub> (STO) substrates using the pulsed laser deposition (PLD) technique (Lambda Physik KrF excimer laser,  $\lambda=248$  nm). LSMO thin films of 30 nm thickness were grown with 200 mTorr background oxygen pressure and laser fluence of 1.5 J/cm<sup>2</sup> and 2 Hz repetition rate. Then an ultrathin BTO films were deposited at an oxygen pressure of 10 mTorr at 5 Hz on the LSMO serving as a bottom electrode. The thicknesses of the BTO films as a tunnel barrier layer

range from 1 nm to 2 nm. Both LSMO and BTO films were deposited at an identical substrate temperature of 700°C. Film thickness for all layers was calibrated using an x-ray reflectivity technique.

Measurements were performed using the MFP-3D (Asylum Research) scanning probe microscope (SPM). We used conductive platinum-coated silicon (DPER-18), platinum (Pt)-silicide (Si) (PtSi) and diamond-coated tips (CDT) for the conducting atomic force microscopy (C-AFM) measurements. The tips vary in terms of their resistivity, contact area characteristics and degree of degradation with usage. Table 5.1.1 summarizes the properties of the tips.

Table 5.1.1 Comparison of properties of three different conductive tips.

	Contact Area (nm <sup>2</sup> )	Tip Material	Wear-out Condition	Frequency (kHz)	Force constant (N/m)	Vender
DPER 18	~10 <sup>2</sup>	Platinum coated	High	75	3.5	Mikromash
PtSi	~10 <sup>3</sup>	Platinum and Silicide	Middle	330	42	Nanoworld
CDT	~10 <sup>4</sup>	Highly doped Diamond	Low	400	80	Nanoworld

The SPM was used primarily in the piezoresponse force microscopy (PFM) and conducting AFM (C-AFM) mode. PFM allows us to investigate and control the local ferro- and piezo-electric properties, while the C-AFM was utilized to observe the dependence of the tunneling properties of the barrier on the polarization state as a function of applied bias. To perform the writing operation of different polarization states, the BTO film was poled by applying either a negative or positive tip bias. Reading of the polarization states was achieved by

a conventional PFM imaging method. In addition, local ferroelectric switching properties were characterized by a switching spectroscopy method in which a saw tooth-shaped bias voltage was swept with the tip in a contact mode, while measuring the piezoelectric phase and amplitude.

In order to investigate the local current ( $I$ ) vs. voltage ( $V$ ) characteristics, a linear sweep voltage was applied and then  $I$ - $V$  curves were obtained by measuring the current as a function of sweep voltage for different ferroelectric polarization states.

## 5.2 Experimental results and discussion

### 5.2. Piezoelectric properties of the ultrathin BaTiO<sub>3</sub> films

AFM micrographs of 2 nm BTO films grown on 30 nm LSMO bottom electrode show an atomically-flat surface with root-mean-square (rms) roughness of 0.2 nm as seen in Fig. 5.2.1. The films are essentially free of nanodroplets that are typically associated with the PLD process.

Robust ferro- and piezo-electric properties of the BTO films are observed on patterned polarized regions, as seen in Fig. 5.2.2 (a), (b). The University of Alabama logo has been used to generate the pattern. The pattern was processed by applying a positive or negative bias voltage to generate different polarization states in a white and black zone as seen in Fig. 5.2.2(a). The bias voltage is applied through a conductive tip with the LSMO film serving as the ground electrode. The characteristic piezoelectric response of the film was clearly demonstrated as different color contrasts for the two polarization states, illustrating a clear elephant image as shown in Fig. 5.2.2(b). The dark brown color corresponds to the regions poled by negative bias voltage, while the light brown region reflects the positively poled areas.

Nanoscale ferroelectric properties of the 2 nm BTO film have been quantified using a switching spectroscopy PFM method, [92] as seen in Fig. 5.2.3. We placed a conductive tip on a

single point region and swept the bias voltage over a range larger than the coercive field to obtain fully saturated polarization switching loops. The polarization reflected ferroelectric hysteresis behavior is clearly observed in Fig. 5.2.3(a) along with a butterfly-shaped loop for the phase in Fig. 5.2.3(b). Both hysteresis loops show similar result of hysteresis loops as measured for a 4.8 nm BTO film [87]. However, a complete 180 degree phase reversal is not observed. This is likely due to depolarization behavior, which has previously also been observed for ultrathin films that are close to the critical thickness for ferroelectricity [33]. The depolarization is caused by displacement of  $\text{Ti}^{4+}$  closer to the symmetric central position in the perovskite structure with reduced polarization.

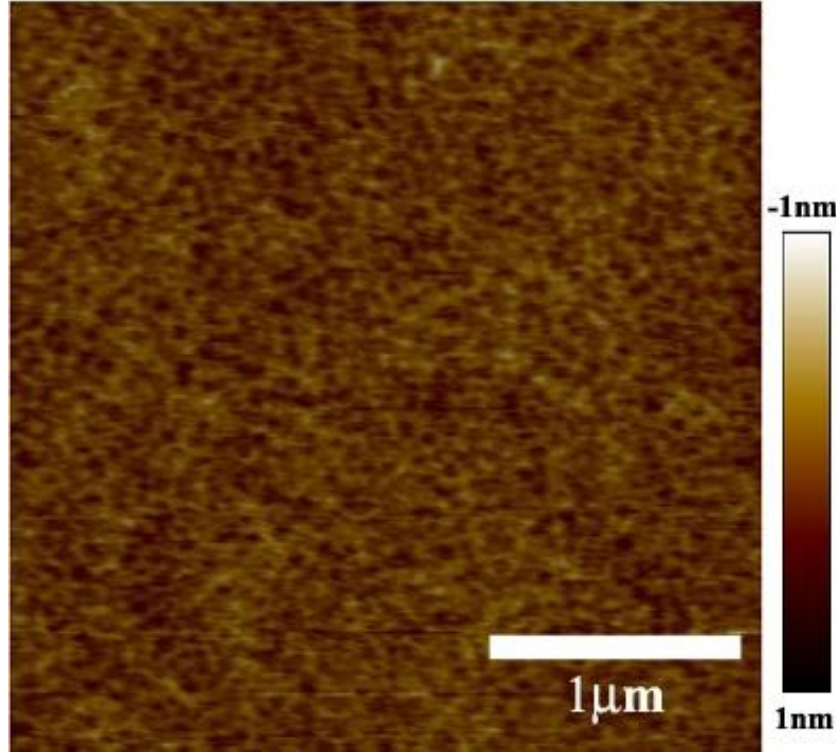


Figure 5.2.1 AFM surface topology image of BTO film of thickness 2 nm. RMS roughness of the film is 0.2 nm.

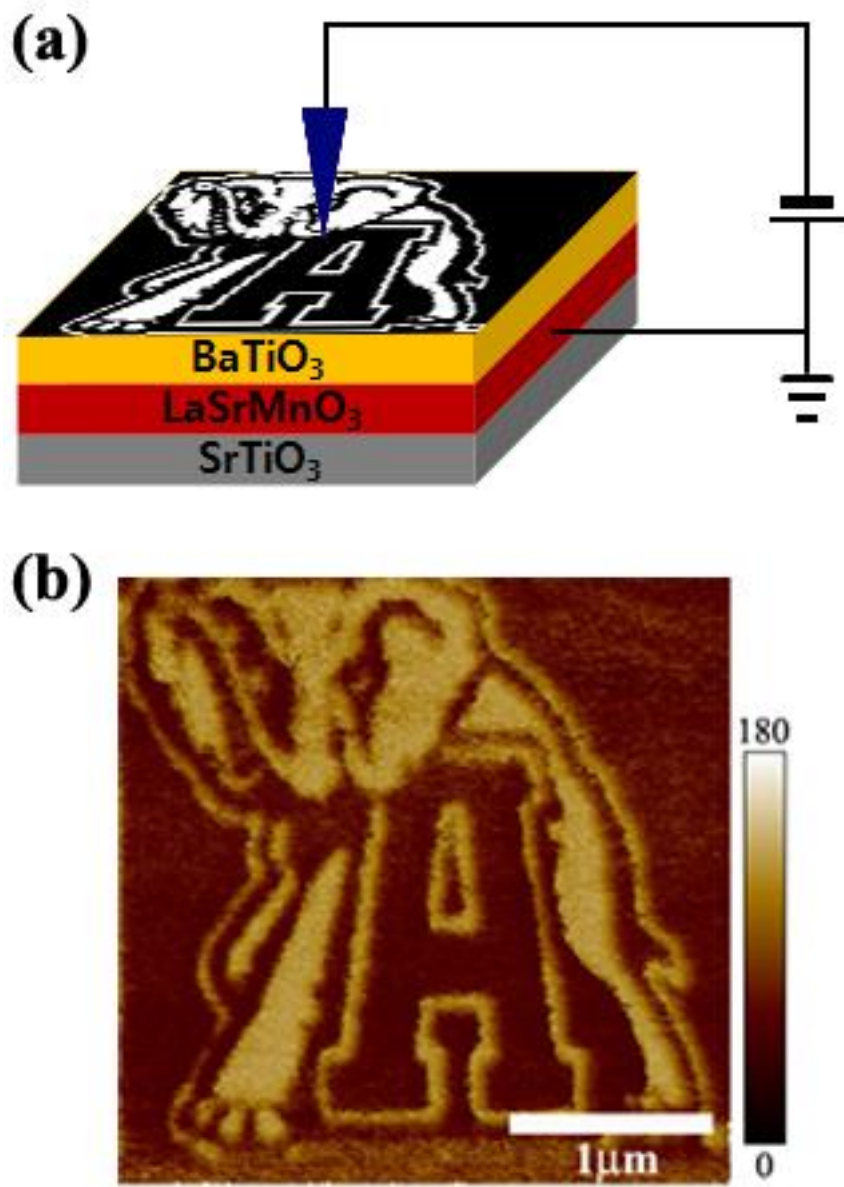


Figure 5.2.2 Schematic for generating polarization pattern (a) and a polarized image showing UA logo with an elephant (b). Black color zone is written using a tip voltage,  $V_{\text{tip}} = -3\text{V}$  and white color is zone is written using a tip voltage,  $V_{\text{tip}} = +3\text{V}$ .

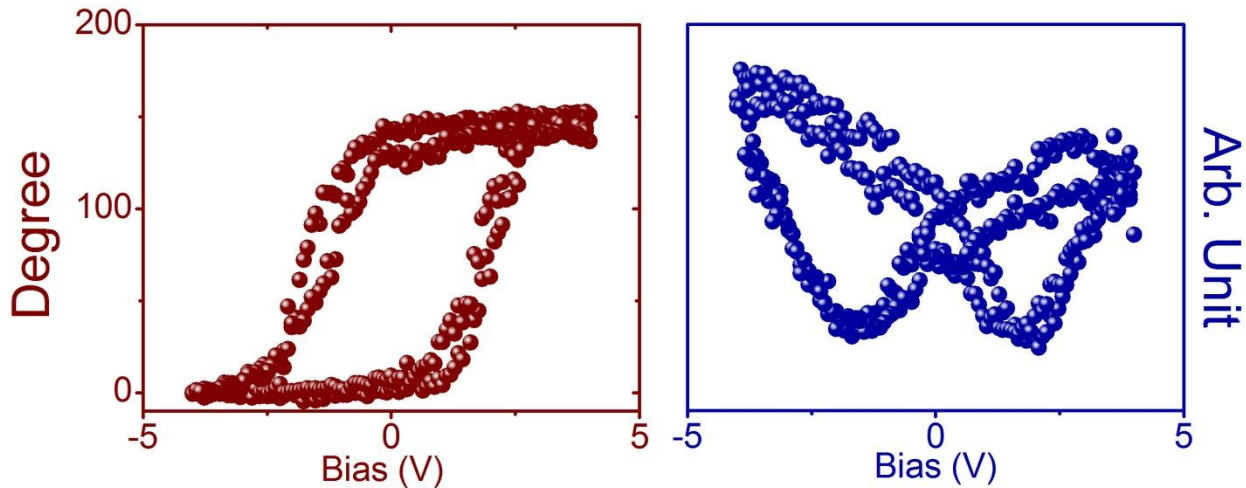


Figure 5.2.3 Hysteresis loop corresponding to polarization switching of BTO film. (a) Phase map in degree and (b) amplitude map exhibiting a butterfly loop.

To systematically control the UP-DOWN polarization states (UP implying polarization vector pointing towards the tip), a  $2 \mu\text{m} \times 2 \mu\text{m}$  square area is first poled in the downward direction using a negative tip bias of -3 V (Fig. 5.2.4(a-1)) and then a  $0.7 \mu\text{m} \times 0.7 \mu\text{m}$  square region in the center is reverse-poled by a positive tip bias of +3 V (Fig. 5.2.4(a-2)). The dark and light PFM contrast of a larger  $3 \mu\text{m} \times 3 \mu\text{m}$  square area (Fig. 5.2.4(b)) shows clearly the different polarization states in the two regions. We further successfully have rewritten a rectangular area in the top region of the polarized pattern by applying a positive bias voltage after the initial patterning process (Fig. 5.2.4(a-3)). The re-read PFM image is seen in Fig. 5.2.4(c). We also confirmed that Fig. 5.2.4 (c) image is retained for at least three days. These results indicate that ultrathin 2 nm BTO films exhibit robust and reproducible piezoelectric/ferroelectric properties. Qualitatively similar results have been obtained with a 1.2 nm (3 unit cells) thick BTO film on LSMO, although the PFM contrast is not as sharp as that for the 2 nm film.

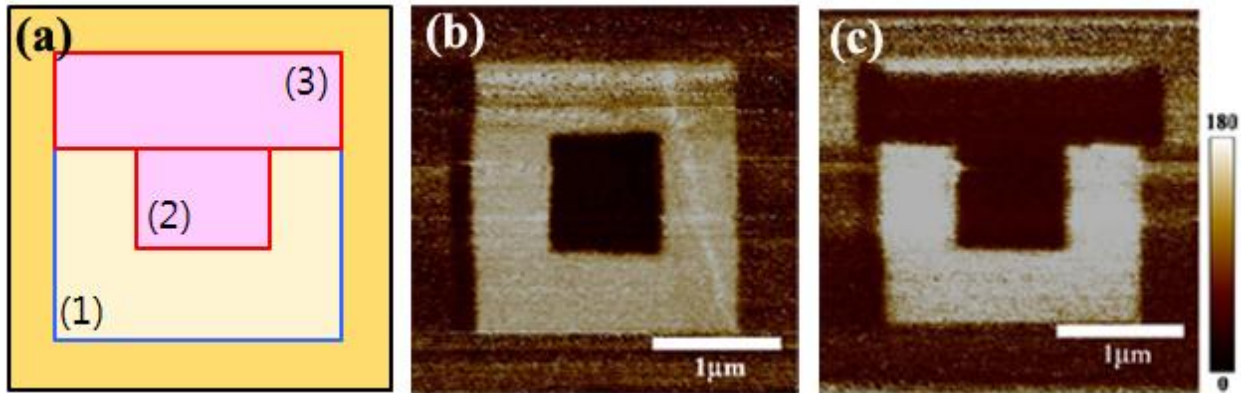


Figure 5.2.4 Schematic illustration for creating different polarization state regions. (a-1)  $2\mu\text{m} \times 2\mu\text{m}$  square zone poled by a negative voltage. (a-2)  $1\mu\text{m} \times 1\mu\text{m}$  center region poled by a positive voltage. (a-3) is re-poled area by a positive voltage after 6 hours. (b) PFM image after initial polarization resulting from steps (a-1) and (a-2). (c) Re-read PFM image after step (a-3).

## 5.2.2 Conductive properties of the ultrathin $\text{BaTiO}_3$ films

Local tunneling properties of ultrathin BTO film have been investigated by measuring the current-voltage ( $I-V$ ) characteristics using C-AFM technique. Measurements shown here are performed on ferroelectric BTO thin films of thickness 1.2 nm. We primarily used commercial conductive diamond coated tips for the C-AFM measurements as they have a large tip area, which gives better contact, while the hardness of diamond provides low degree of tip wear during scans. Firstly, we acquired current-maps where the tunnel current is measured during typical raster-scans while maintaining the tip at 1 Volt (Fig. 5.2.5).

Prior to performing these measurements, an UP (DOWN) polarization state is generated by applying a high positive (negative) voltage through the sample with the tip acting as a virtual ground (Fig. 5.2.5 (a), (c)). In Fig. 5.2.5 (b) and (d), we show a typical current-map of a  $0.5\mu\text{m} \times 0.5\mu\text{m}$  area of the BTO/LSMO heterostructure with upward and downward polarization orientations, respectively. The bright gray (green) color indicates a relatively high (low) tunnel current in the case of polarization pointing upward (downward). This is the TER effect,

described as the change in the resistance of the thin BTO/LSMO heterostructure arises from the switching of the polarization orientation [18]. Even though there are some local variations in the tunnel current, our data clearly shows that the TER effect is robust over large areas of the BTO/LSMO heterostructure.

To further quantify the TER effect, local current ( $I$ ) - voltage ( $V$ ) measurements have been carried out by locally applying a sweep voltage ranging between + 0.5 V to - 0.5 V after creating one of the two polarization states in the sample. As Fig. 5.2.6 clearly indicates, significantly higher current (lower DC resistance) is observed for the UP state as compared to the DOWN state for all bias voltages. We refer to the high current (low resistance) state as the ON state and the low current (high resistance) state as the OFF state. This data, again, confirms the TER effect is robust down to a barrier thickness typically found in commercial hard-drive read-heads with MgO tunnel barrier. Calculation of the resistance ratio between two polarization states reveals a value of up to 60 at low bias (inset of Fig. 5.2.6), which is comparable to the reported values in ref. [86].

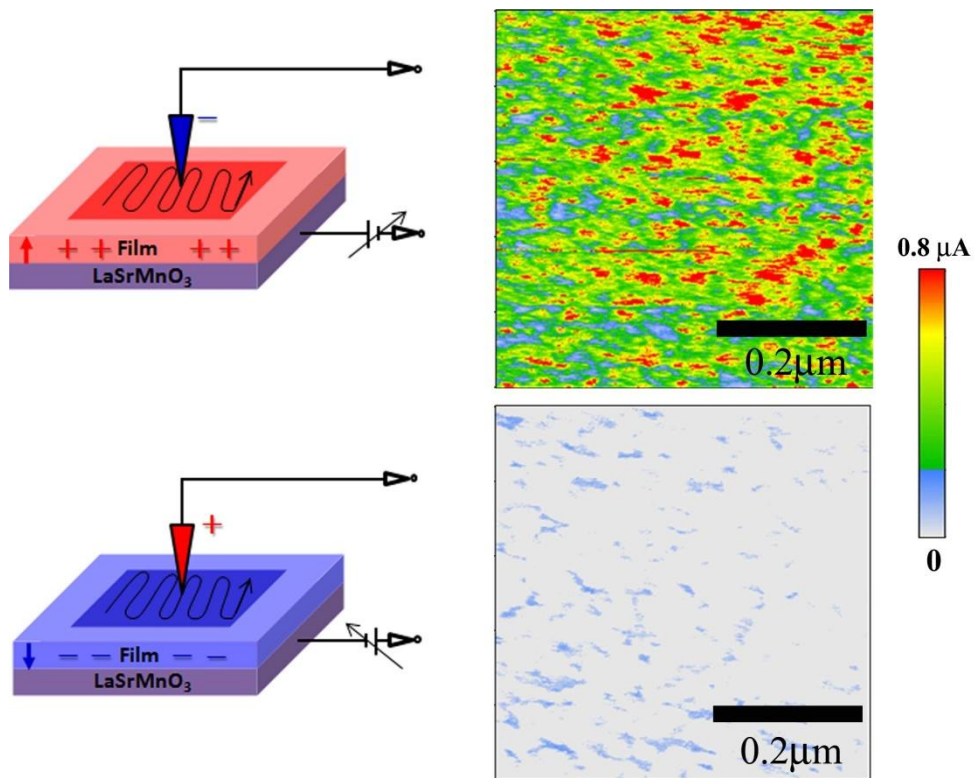


Figure 5.2.5 Schematic of configurations for polarization orientation. (a) Polarization pointing upward by application of a positive sample bias. (b) Current map while scanning the region. (c) Polarization pointing downward by application of a negative sample bias. (d) Current map while scanning the same region. For the measurements the tip is grounded and the current is measured using an amplifier.

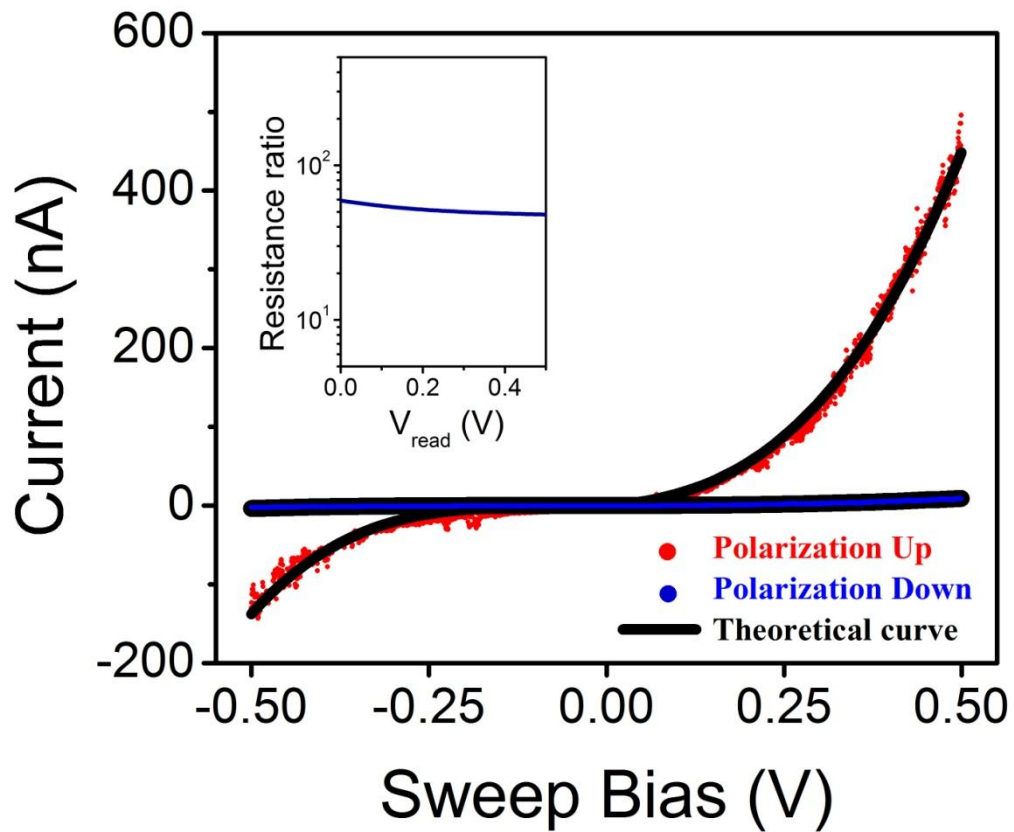


Figure 5.2.6 I-V curves measured with different polarization states, upward or downward, corresponding to switch 'ON' or 'OFF' state. The black lines represent *I-V* curves fits using the Brinkman model. Insert shows the TER and ON/OFF ratio

Detailed characterization of the TER effect has also been performed with two other commercial tips. Both PtSi and DPER-18 tips exhibit lower tunnel current as seen in Fig. 2.5.7 (a) and (c), primarily because of the small contact area ( $\sim 10^2 \text{ nm}^2$ ). The corresponding resistance ratios between the two polarization states as seen in Fig. 5.2.7 (b) and (d) are also substantially smaller as compared to the conducting diamond tip, with values between 10-30 being observed at low bias voltages. We must mention that tip degradation is especially severe during local *I-V* characterization, particularly for the PtSi and DPER-18 tips, and only the few first passes with a brand new tip yield any measurable current. The characterizations shown here are, therefore, confirmed through measurements with numerous tips.

The experimentally obtained *I-V* curves have been fitted with the Brinkman model assuming a trapezoidal potential barrier to obtain information about the average barrier height [93]. The black solid line in Fig. 5.2.6 shows the simulated *I-V* curve. As clear, the experimental points (solid red and blue dots) are well-matched with the theoretical fit (black solid lines). According to the Brinkman model, the conductance is expressed by the polynomial

$$\frac{dI}{dV} = A + BV + CV^2 \quad (1)$$

where  $A$ ,  $B$ , and  $C$  can be evaluated by fitting the experimental I-V curves. Based on the values of the constants  $A$ ,  $B$ , and  $C$ , one can calculate the barrier height ( $\varphi$ ) in eV, barrier asymmetry ( $\Delta\varphi$ ) in eV, and barrier thickness ( $d$ ) in Å

$$I = AV + B\frac{V^2}{2} + C\frac{V^3}{3} \quad (2)$$

$$d^2 = 5.368 \sqrt{\frac{C}{A}} \ln(1.747 \times 10^{-10} \sqrt{CA}) \quad (3)$$

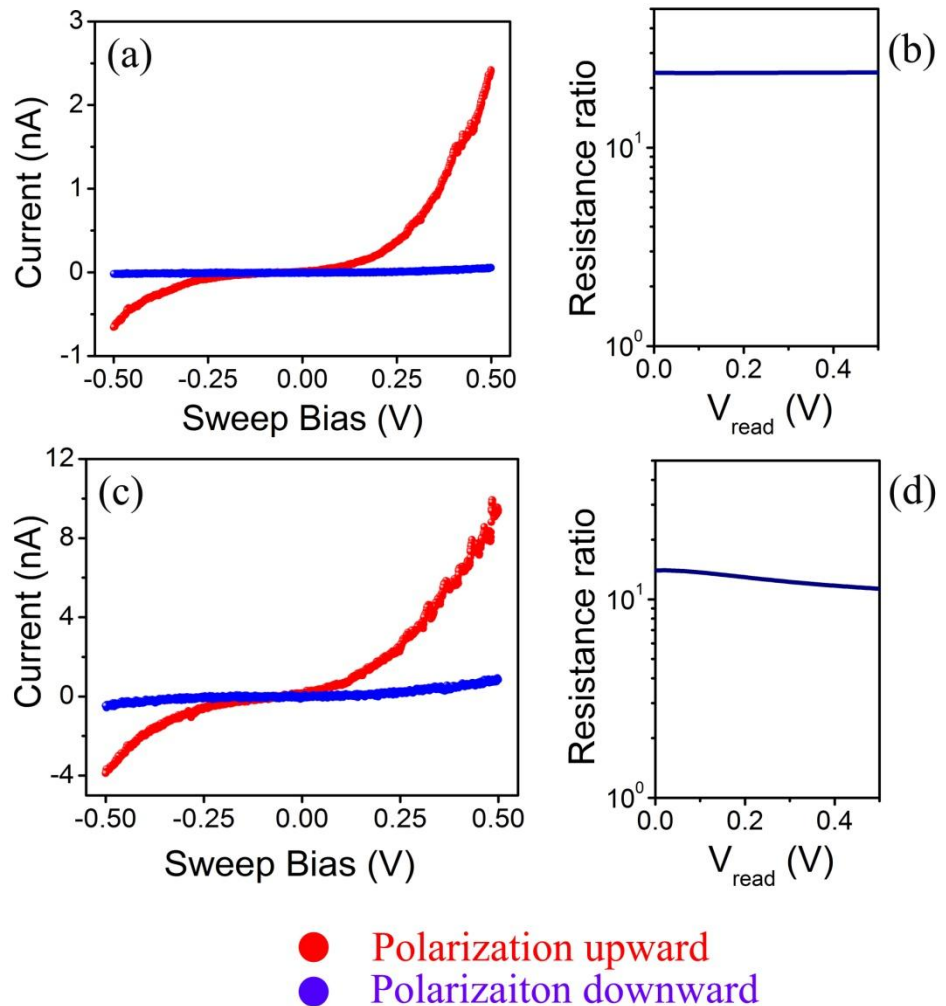


Figure 5.2.7 I-V curves and TER values measured by DPER 18 (a)-(b), and PtSi (c)-(d) commercial tips at different polarization states, upward or downward, corresponding to switch 'ON' or 'OFF' state.

$$\varphi = 0.0328 \left(\frac{A}{c}\right) d^2 \quad (4)$$

$$\Delta\varphi = 23.42 \left(\frac{B}{A}\right) \frac{\varphi^{3/2}}{d}. \quad (5)$$

Using eq. (2-5) for the different polarization states, ON and OFF, we calculated film thickness, barrier height, and barrier asymmetry due to three commercial tips. Table 5.2.1 summarizes the results. The fitted film thickness is between 3-4 nm, which is higher than the experimental film thickness of 1.2 nm. We believe that the discrepancy is due to the simplicity of the theoretical model, which does not consider experimentally involved conditions such as interaction of the tips with the sample, BTO film surface morphology and roughness, and other tip-induced effects during the measurement.

The barrier heights determined using the different tips when fitted with the Brinkman model are compared as shown in Fig. 2.5.8. The CDT and DPER-18 tips provide lower barrier height values for the ON state as compared to the OFF state. The average barrier height values show slight variation with the tip used, but overall in reasonable agreement with previous reports [86, 87]. As expected from tunneling behavior, the average barrier height value are higher for the OFF state than the ON, except for the PtSi tip, which gives a higher barrier height value for the ON state. As equations Eq. (2-5) show, the average barrier height and asymmetry depends only on the ratio of the fit parameters (A, B, C), which takes away any dependence on the current value. In other words, the barrier height from the Brinkman model is related to the shape of the *I-V* curve.

TABLE 5.2.1 Theoretical values calculated by Brinkman equation fit using three different conductive tips.

Polarization state		Ultrathin BTO film (1.2nm)		
		Thickness (d) (nm)	Barrier Height ( $\phi$ ) (eV)	Barrier asymmetry( $\Delta\phi$ ) (eV)
DPER-18	ON	3.8	0.34±0.05	3.2±0.15
	OFF	4.2	0.55±0.1	3.4±0.1
PtSi	ON	2.3	0.7±0.03	3.5±0.15
	OFF	3.2	0.43±0.03	1.6±0.2
CDT	ON	3.1	0.29±0.03	2.4±0.1
	OFF	3.5	0.32±0.03	3.1±0.14

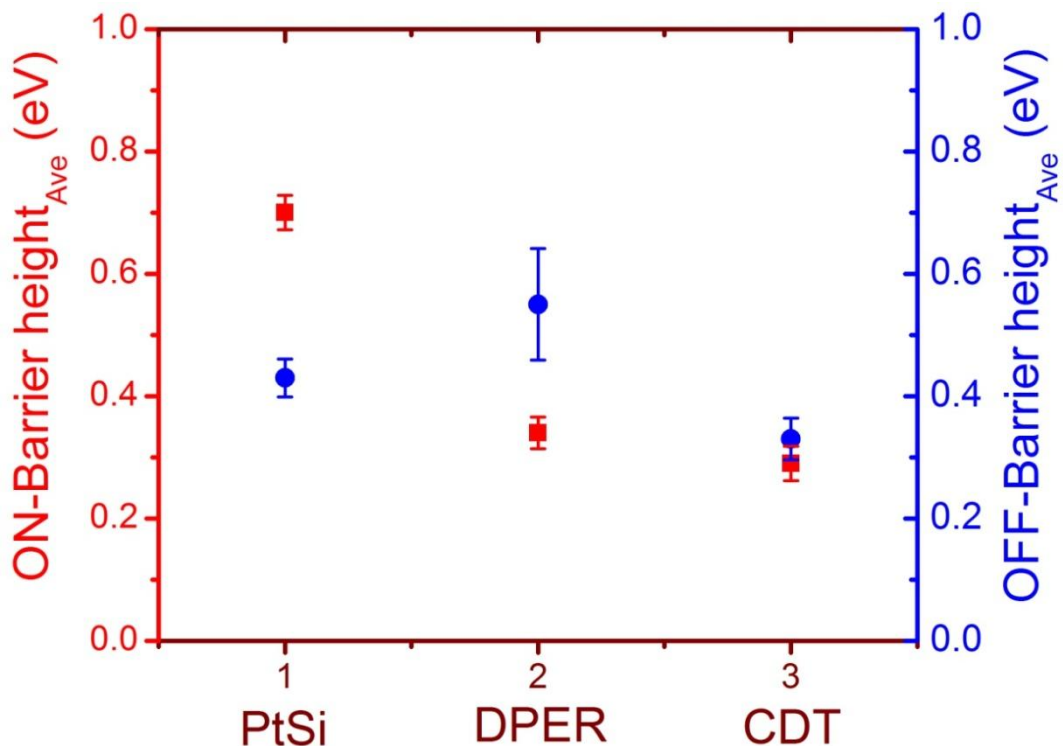


Figure 5.2.8 Comparison of barrier heights of polarization ON and OFF states due to applied different commercial tips.

### 5.3 Summary

We have demonstrated robust tunnel electroresistance effect in BTO/LSMO heterostructures using piezoresponse force and conducting atomic force microscopy. Nanoscale PFM measurements clearly reveal reproducible piezoelectric properties. C-AFM characterizations are performed through current maps and current-voltage (*I-V*) curves. Through these techniques, we demonstrate polarization-dependent and switchable tunneling current, thereby confirming the TER effect in 1.2 nm BTO film. A variety of commercial tips reveals a resistance ratio between the two polarization states between 10-60. Encouraging for commercial purposes is the result that METJs with BTO barrier can be scaled down to a thickness, which is comparable to current spintronics technology.

## CHAPTER 6

### CONCLUSION AND FUTURE WORK

We successfully synthesized MgO template nanowires using a CVD method with controlled placement and formation of vertical free-standing structures. SEM images clearly show vertically standing single MgO NWs. Using TEM we have determined the growth direction to be  $<001>$ , which is the same as the growth direction of the template MgO NWs. Therefore, the MgO NWs grow homoepitaxially on single crystalline (001)-MgO substrates.

We developed processes for the optimized growth of BaTiO<sub>3</sub> (BTO) and NiFe<sub>2</sub>O<sub>4</sub> (NFO) thin films on (001)-oriented MgO substrates via the pulsed laser deposition (PLD) technique prior to applying the process for growth of single-phase BTO or NFO coatings on the NWs. X-ray diffraction measurements indicate that the films undergo tensile stress on MgO substrate. X-ray Phi ( $\phi$ ) scan and RHEED studies clearly demonstrate that both the BTO and NFO films grow heteroepitaxially on MgO.

Utilizing the process conditions for thin film growth, single-phase BTO and NFO-coated NWs were fabricated by coating BTO or NFO via PLD onto the template MgO NWs. The successful growth of the individual layers on the MgO NWs suggests that binary-coated multiferroic NWs of NFO/BTO can be formed.

We deposited ultrathin ferroelectric BaTiO<sub>3</sub> (BTO) films of a few unit cells thickness on La<sub>0.67</sub>Sr<sub>0.33</sub>MnO<sub>3</sub> (LSMO) films serving as bottom electrode on SrTiO<sub>3</sub> (STO) substrate using PLD. The thin BTO film grows heteroepitaxially on top of the LSMO layer and serves as a

magnetoelectric tunnel barrier. Piezoresponse force microscopy (PFM) studies reveal robust piezoelectric properties of the BTO film, exhibiting both phase deformation and hysteresis loops in phase and amplitude. Conducting Atomic Force Microscopy (C-AFM) measurements clearly demonstrate tunneling behavior across the thin BTO barrier based on the non-linear current ( $I$ ) vs. voltage ( $V$ ) characteristics. Furthermore, the  $I$ - $V$  curves reveal low or high conductivity across the barrier based on different polarization states - up (down) by applying positive (negative) bias voltage. From detailed analysis of the  $I$ - $V$  curves, we confirmed the tunneling electresistance (TER) effect in the conducting tip/BTO/LSMO structures with ON/OFF current ratios as high as 60 at low bias for a 3 unit cell (1.2 nm) BaTiO<sub>3</sub> tunnel barrier. The result demonstrates that METJs are scalable down to barrier layer thicknesses comparable to commercial spintronic devices. As a result, because of the reproducible switchable ON and OFF current with applied bias, the heterostructures are attractive for future magnetoelectric random access memory (MERAM) device applications.

Three different conductive tips, DPER-18, PtSi, and CDT, were applied for the  $I$ - $V$  curve measurements. All of the tips successfully demonstrate non-linear  $I$ - $V$  curves and ON/OFF current ratio depending on the polarization states. However, the tips exhibit different levels of tunnel current and the ratio. This phenomenon can arise from the tip variation in terms of their contact area characteristics and different degree of wear-out characteristics. The wear-out eventually modifies the contact area during use. Thus, it is difficult to quantitative interpret the correlation between the measurements and contact area effect.

In order to resolve the difficulty, it is suggested to use a ruthenium (Ru) dot, which can serve as a top electrode. Optical lithography is a routine technique to fabricate such circularly patterned dots. Thin Ru film can be then deposited on the dots using film deposition technique

such as sputtering. The diameter of these dots can be variable from 1 - 5  $\mu\text{m}$ . The measurements will focus on the  $I$ - $V$  curve and ON/OFF current ratio due to the contact area dependence. Indeed, the results could be also useful to design an actual junction prototype with optimal dimensions of the layered structure.

## REFERENCES

1. N. Setter, D. Damjanovic, L. Eng, G. Fox, S. Gevorgian, S. Hong, A. Kingon, H. Kohlstedt, N. Y. Park, G. B. Stephenson, I. Stolitchnov, A. K. Taganstev, D. V. Taylor, T. Yamada, and S. Streiffer, *J. Appl. Phys.* **100**, 051606 (2006).
2. J. Douglas Adam, Lionel E. Davis, Gerald F. Dionne, Ernst F. Schloemann and Steven N. Stitzer, *IEEE Trans. Micro. Theory and Tech.* **50**, 721 (2002).
3. Orlando Auciello, James F. Scott and Ramamoorthy Ramesh, *Physics Today* **51**, 22 (1998).
4. Johan Åkerman, *Science* **308**, 508 (2005).
5. J. F. Scott, *Science* **315**, 954 (2007).
6. Hans Schmid, *Ferroelectrics* **162**, 317 (1994).
7. W. C. Röntgen, *Phys. Math. Cl.* **19**, 264 (1888).
8. P. Debye, “Bemerkung zu einigen neuen versuhen über einen magneto-elektrischen richteffekt”, 300 (1926).
9. Manfred Fiebig, *J. Phys. D* **38**, R123 (2005).
10. Ce-Wen Nan, M. I. Bichuri, Shuxiang Don, D. Viehlan, and G. Srinivasan, *J. Appl. Phys.* **103**, 031101 (2008).
11. Thomas Lottermoser, Thomas Lonkai, Uwe Amann, Dietmar Hohlwein, Jörg Ihringer and Manfred Fiebig, *Nature* **430**, 541 (2004).
12. T. Kimura, T. Goto, H. Shintani, K. Ishizaka, T. Arima, and Y. Tokura, *Nature* **426**, 55 (2003).
13. Manuel Bibes and Agnès Barthélémy, *Nature Materials* **7**, 425 (2008).
14. Claude Chappert, Albert Fert and Frédéric Nguyen Van Dau, *Nature Materials* **6**, 813 (2007).
15. Martin Gajek, Manuel Bibes, Stéphane Fusil, Karim Bouzehouane, Josep Fontcuberta, Agnès Barthélémy and Albert Fert, *Nature Materials* **6**, 296 (2007).
16. Nicola Spaldin, “Magnetic Materials - Fundamentals and Device Applications”, Cambridge (2003).
17. Javier Junquera and Philippe Ghosez, *Nature* **422**, 506 (2003).

18. M. Ye Zhuravlev, R. F. Sabirianov, S. S. Jaswal, and E. Y. Tsymbal, Phys. Rev. Lett. **94**, 246802 (2005).
19. H. Béa, S. Fusil, K. Bouzehouane, M. Bibes, M. Sirena, G. Herranz, E. Jacquet, J.-P. Contour and A. Barthélémy, Jap. J. Appl. Phys. **45**, L187 (2006).
20. V. Garcia, S. Fusil, K. Bouzehouane, S. Enouz-Vedrenne, N. D. Mathur, A. Barthélémy and M. Bibes, Nature **460**, 81 (2009).
21. Ce-Wen Nan, Gang Liu, and Yuanhua Lin, Phy. Rev. Lett. **94**, 197203 (2005).
22. V. M. Petrov, G. Srinivasan, M. I. Bichurin, and A. Gupta, Phys. Rev. B. **75**, 224407 (2007).
23. Matt Law, Annu. Rev. Mater. Res. **34**, 83 (2004).
24. Jia Grace Lu, Mat. Sci. and Eng. **R52**, 49 (2006).
25. Charles M. Lieber, MRS. Bulletin **32**, 99 (2007).
26. R. Ramesh and Nicola A. Spaldin, Nature Materials **6**, 21 (2007).
27. M. Ye Zhuravlev, S. S. Jaswal, E. Y. Tsymbal, and R. F. Sabirianov, Appl. Phys. Lett. **87**, 222114 (2005).
28. Lincoln J. Lauhon, Mark S. Gudiksen, Deli Wang and Charles M. Lieber, Nature **420**, 57 (2002).
29. M. E. Lines and A. M. Glass, “Principles and Applications of Ferroelectrics and Related Materials”, Oxford (1977).
30. Y. Frenkel, Phys. Rev. **36**, 1604 (1930).
31. L. Esaki, IBM Technical Disclosure Bulletin **13**, 2161 (1971).
32. Evgeny Y. Tsymbal and Hermann Kohlstedt, Science **313**, 181 (2006).
33. Nicola A. Spaldin, Science **304**, 1606 (2004).
34. Andre Chanthbouala, Vincent Garcia, Karim Bouzehouane, Stéphane Fusil, Xavier Moya, Julie Allibe, Bruno Dlbak, Julie Grollier, Stéphane Xavier, Cyrile Deranlot, Amir Moshar, Roger Proksch, Neil D. Mathur, Manuel Bibes and Agnès Barthélémy, Nature Nanotechnology **7**, 101 (2012).
35. H. Béa, M. Bibes, S. Cherifi, F. Nolting, B. Warot-Fonrose, S. Fusil, G. Herranz, C. Deranlot, E. Jacquet , K. Bouzehouane, and A. Barthélémy, Appl. Phys. Lett. **89**, 242114 (2006).
36. R. A. McCurrie, “Ferromagnetic Materials: Structure and Properties”, Academic Press (1994).

37. B. D. Cullity, "Introduction to Magnetic Materials", Addison-Wesley (1972).
38. S. S. P. Parkin, *Annu. Rev. Mater. Sci.* **25**, 357 (1995).
39. H. Béa, M. Gajek, M. Bibes and A. Barthélémy, *J. Phys.: Condens. Matter.* **20**, 434221 (2008).
40. M. Julliére, *Phys. Lett.* **54 A** 224 (1975).
41. V. Garcia, M. Bibes, L. Bocher, S. Valencia, F. Kronast, A. Crassous, X. Moya, S. Enouz-Vedrenne, A. Gloter, D. Imhoff, C. Deranlot, N. D. Mathur, S. Fusil, K. Bouzehouane, A. Barthélémy, *Science* **327**, 1106 (2010).
42. Julian P. Velev, Chun-Gang Duan, J. D. Burton, Alexander Smogunov, Manish K. Niranjan, Erio Tosatti, S. S. Jaswal and Evgeny Y. Tsymbal, *Nano Lett.* **9**, 427 (2009).
43. A. V. Bune, V. M. Fridkin, Stephen Ducharme, L. M. Blinov, S. P. Palto, A. V. Sorokin, S. G. Yudin and A. Zlatkin, *Nature* **391**, 874 (1998).
44. Michael Hambe, Adrian Petraru, Nikolay A. Pertsev, Paul Munroe, Valanoor Nagarajan and Hermann Kohlstedt, *Adv. Funct. Mat.* **20**, 2436 (2010).
45. E. Ascher, H. Rieder, H. Schmid, and H. Stössel, *J. Appl. Phys.* **37**, 1404 (1966).
46. W. Prellier, M P Singh and P Murugavel, *J. Phys.: Condens. Matter.* **17**, R803 (2005).
47. Nicola A. Hill, *J. Phys. Chem. B* **104**, 6694 (2000).
48. J. Van Suchtelen, *Philip. Res. Repts.* **27**, 28 (1972).
49. J. van den Boomgaard and R. A. J. Born, *J. Mat. Sci.* **13**, 1538 (1978).
50. Jian-ping Zhou, Hong-Cai He, Zhan Shi, Gang Liu, and Ce-Wen Nan, *J. Appl. Phys.* **100**, 094106 (2006).
51. Ce-Wen Nan, *Phy. Rev. B* **50**, 6082 (1994).
52. Douglas B Chrisey, Graham K Hubler, "Pulsed Laser Deposition of Thin Films", Wiley-Interscience (1994).
53. I. Fina, N. Dix, L. Fàbrega, F. Sánchez, J. Fontcuberta, *Thin Solid Films* **518**, 4634 (2010).
54. Shigeto Shouriki, Eisuke Tokumitsu and Hiroshi Ishiwara, *Jpn. J. of Appl. Phys.* **37**, 6497 (1998).
55. A. Moreira dos Santos, S. Parashar, A.R. Raju, Y.S. Zhao, A.K. Cheetham, C.N.R. Rao, *Solid. State. Comm.* **122**, 49 (2002).

56. J. Wang, J. B. Neaton, H. Zheng, V. Nagarajan, S. B. Ogale, B. Liu, D. Viehland, V. Raghavan, D. G. Schlom, U. V. Waghmare, N. A. Spaldin, K. M. Rabe, M. Wuttig, and R. Ramesh, *Science* **299**, 1719 (2003).
57. Norifumi Fujimura, Tadashi Ishida, Takeshi Yoshimura, and Taichiro Ito, *Appl. Phys. Lett.* **69**, 1011 (1996).
58. H. Zheng, J. Wang, S. E. Lofland, Z. Ma, L. Mohaddes-Ardabili, T. Zhao, L. Salamanca-Riba, S. R. Shinde, S. B. Ogale, F. Bai, D. Viehland, Y. Jia, D. G. Schlom, M. Wuttig, A. Roytburd, and R. Ramesh, *Science* **303**, 661 (2004).
59. Gang Liu, Ce-Wen Nan, Z K Xu and Haydn Chen, *J of Phys.D.: Appl. Phys.* **38**, 2321 (2005).
60. Chaoyong Deng, et al., *J of Appl. Phys.*, 102 074114 (2007); Yi Zhang, et al., *Appl. Phys. Lett.* **92**, 062911 (2008).
61. V. Laukhin, V. Skumryev, X. Martí, D. Hrabovsky, F. Sánchez, M. V. García-Cuenca, C. Ferrater, M. M. Varela, U. Lüders, J. F. Bobo, and J. Fontcuberta, *Phy. Rev. Lett.* **97**, 227201 (2006).
62. Gustau Catalan, and James F. Scott, *Adv. Mater.* **21**, 2463 (2009).
63. S. M. Wu, Shane A. Cybart, P. Yu, M. D. Rossell, J. X. Zhang, R. Ramesh and R. C. Dynes, *Nature Mater.* **9**, 756 (2010).
64. Song Han, Li, Ziqin Liu, Bo Lei, Daihua Zhang, Wu Jin, Xiaolei Liu, Tao Tang, and Chongwu Zhou, *Nano Lett.* **4**, 1241 (2004).
65. Zhong Lin Wang, “Nanowires and Nanobelts: Materials, Properties, and Devices”, Springer (2006).
66. Jonathan E. Spanier, Alexie M. Kolpak, Jeffrey J. Urban, Ilya Grinberg, Lian Ouyang, Wan Soo Yun, Andrew M. Rappe, and Hongkun Park, *Nano Lett.* **6**, 735 (2006).
67. Daihua Zhang, Ziqin Liu, Song Han, Chao Li, Bo Lei, Michael P. Stewart, James M. Tour, and Chongwu Zhou, *Nano Lett.* **4**, 2151 (2004).
68. C. N. R. Rao and Rahul Sen, *Chem. Commun.* 1525 (1998).
69. R.S. Wagner and W.C Ellis, *Appl. Phys. Lett.* **4**, 89 (1964).
70. Siegfried Schiller, Ullrich Heisig, and Siegfried Paner, “Electron beam technology”, Wiley-Interscience (1982).
71. B. D. Cullity, “Elements of X-ray Diffraction”, Addison-Wesley (1978).
72. David B Williams and C. Barry Carter, “Transmission electron microscopy”, Spring Science (1996).

73. A. Gruverman and M. Alexe “Nanoscale Characterisation of Ferroelectric materials”, Springer (2004).
74. R. Clarke, J. Appl. Cryst. **9** 335 (1976); H. F. Kay, P. Voudsen, Philosophical Magazine Series **7** **40**, 1019 (1949).
75. Ulrike Lüders, Manuel Bibes, Jean-François Bobo, Matteo Cantoni, Riccardo Bertacco, and Josep Fontcuberta, Phys. Rev. B. **71**, 134419 (2005).
76. M. Bowen, M. Bibes, A. Barthélémy, J.-P. Contour, A. Anane, Y. Lemaître, and A. Fert, Appl. Phys. Lett. **82**, 233 (2003); Y. W. Yin, M. Raju, W. J. Hu, X. J. Weng, X. G. Li, and Q. Li, J. Appl. Phys. **109**, 07D915 (2011).
77. S. Kodambaka, J. B. Hannon, R. M. Tromp and F. M. Ross, Nano Lett. **6**, 1292 (2006).
78. Kazuki Nagashima, Takeshi Yanagida, Hidekazu Tanaka and Tomoji Kawai, J. Appl. Phys. **101**, 124304 (2007).
79. Y. Xia, P. Yang, Y. Sun, Y. Wu, B. Mayers, B. Gates, Y. Yin, F. Kim, and H. Yan, Adv. Mater. (Weinheim, Ger) **15**, 353 (2003).
80. T. Yanagida, K. Nagashima, H. Tanaka, and T. Kawai, Appl. Phys. Lett. **91**, 061502 (2007).
81. G. Kim, R. L. Martens, G. B. Thompson, B. C. Kim, and A. Gupta, J. Appl. Phys. **102**, 104906 (2007),
82. E.G. Wolff and T. D. Coskren, J. Am. Ceram. Soc. **48**, 279 (1965).
83. A. Colli, A. Fasoli, P. Beecher, P. Servati, S. Pisana, Y. Fu, A. J. Flewitt, W. I. Milne, and J. Robertson , J. Appl. Phys. **102**, 034302 (2007).
84. C. T. Campbell, Surf. Sci. Rep. **27**, 1 (1997).
85. M. Ye. Zhuravlev, S. S. Jaswal, E. Y. Tsymbal, and R. F. Sabirianov, Appl. Phys. Lett. **87**, 222114 (2005).
86. André Chanthbouala, Arnaud Crassous, Vincent Garcia, Karim Bouzehouane, Stéphane Fusil, Xavier Moya, Julie Julie Allibe, Bruno Dlubak, Julie Grollier, Stéphane Xavier, Cyrile Deranlot, Amir Moshar, Roger Proksch, Neil D. Mathur, Manuel Bibes, and Agnès Barthélémy, Nature Nanotechnology **7**, 101 (2012),
87. A. Gruverman, D. Wu, H. Lu, Y. Wang, H. W. Jang, C. M. Folkman, M. Ye. Zhuravlev, D. Felker, M. Rzchowski, C.-B. Eom and E. Y. Tsymbal, Nano Lett. **9**, 3539 (2009).
88. A. Crassous, V Garcia, K. Bouzehouane, S. Fusil, A. H. G. Vlooswijk, G. Rispens, B. Noheda, M. Bibes and A. Barthélémy, Appl. Phys. Lett. **96**, 042901 (2010).
89. H. Kohlstedt, N. A. Pertsev, J. Rodríguez, and R. Waser, Phys. Rev. B. **72**, 125341 (2005).

90. Javier Junquera and Philippe Ghosez, *Nature* **422**, 506 (2003).
91. V. Garcia, S. Fusil, K. Bouzehouane, S. Enouz-Vedrenne, N. D. Mathur, A. Barthélémy and M. Bibes, *Nature* **460**, 81 (2009).
92. S. Jesse and H. N. Lee, S. V. Kalinin, *Rev. Sci. Instrum.*, **77** 073702 (2006).
93. W. F. Brinkman, R. C. Dynes, and J. M. Rowell, *J. Appl. Phys.*, **41** 1915 (1970).

## BIBLIOGRAPHY

### **PUBLICATIONS**

1. G. Kim, D. Mazumdar, and A. Gupta, “Nanoscale electroresistance properties of all-oxide magneto-electric tunnel junction with ultra-thin barium titanate barrier”, Appl. Phys. Lett., Submitted (2012).
2. J. X. Ma, D. Mazumdar, G. Kim, H. Sato, N. Z. Bao, and A. Gupta, “A robust approach for the growth of epitaxial spinel ferrite films”, J. Appl. Phys., **108**, 063917 (2010).
3. G. Kim, R. L. Martens, G. B. Thompson, B.C. Kim, and A. Gupta, “Selective Area Synthesis of Magnesium Oxide Nanowires”, J. Appl. Phys., **102**, 104906 (2007).
4. R. L. Martens, G. Kim, G. B. Thompson, B. C. Kim and A. Gupta, “Fabrication and Characterization of Selectively Patterned MgO nanowires”, Microscopy and Microanalysis Proceedings, **13**(2), 772-773CD (2007).

### **PRESENTATIONS**

1. G. Kim, Arunava Gupta, Alexander Tatarenko, and Gopalana Srinivasan, “Fabrication and Properties of Multiferroic Nanowire Heterostructures”, DG-07, 53<sup>rd</sup> Magnetism and Magnetic Materials Conference, Austin, TX, November (2008).
2. G. Kim, R. L. Martens, G. B. Thompson and A. Gupta, “Fabrication and Properties of Multiferroic Nanowire Heterostructures”, 3<sup>rd</sup> International PFM Workshop, Oak Ridge National Lab., TN, October (2008).

## Appendix A: Nanofabrication of four-point contact pads using e-beam lithography

One of feasible plans is to fabricate micrometer pads where the single multiferroic nanowire (NW) will be electrically contacted. The electrical measurements made using the pads help one to demonstrate magnetoelectric properties of an individual NW in the presence of a magnetic field (magnetic control of electric property,  $ME_H$ ) and provide a platform for subsequent device fabrication. In this appendix, the contact pads are briefly described.

The four point electrical contact pads were fabricated using e-beam lithography. In order to fabricate the pads, the coated nanowires were dispersed on a silicon oxide layer. Then the position of an individual wire was recorded before the e-beam lithography process. A positive PMMA resist was spin coated with 400 nm resist thickness on the silicon oxide layer. E-beam lithography with e-beam dose,  $240nC/cm^2$ , was applied. The detail e-beam steps are described in chapter 3. SEM images of a four-point contact pad on a single coated nanowire with the gold contact thin film are seen in Fig. A1 SEM image in Fig A1(a) shows successfully patterned contact pads. In a zoom-in image, the four legs of width 1 micron meter ( $\mu m$ ) with  $1\mu m$  space between legs are clearly visible. To reduce any electric perturbation between large square patterns in  $100 \mu m^2$  area a second pad pattern was designed. Fig. A1(b) shows images of the pads and of a single NW placed on the four legs. Here, the length of the NW is  $7 \mu m$  and the spacing between the legs is  $0.5 \mu m$  and the width of the legs is  $1 \mu m$ . As seen in Fig. A1(b), there is sufficient space between the contact pads thus we do not expect any electrical perturbation during a measurement. In addition, we observe that the NW is well attached under the legs coated with gold contact thin film. The SEM images clearly demonstrate the reliable

lithography process and encourage advanced circuit configuration for the practical measurements. Detailed measurements using the pads, which is suggested for the future, will address the potential for the  $\text{ME}_\text{H}$  measurement of individual multiferroic NWs.

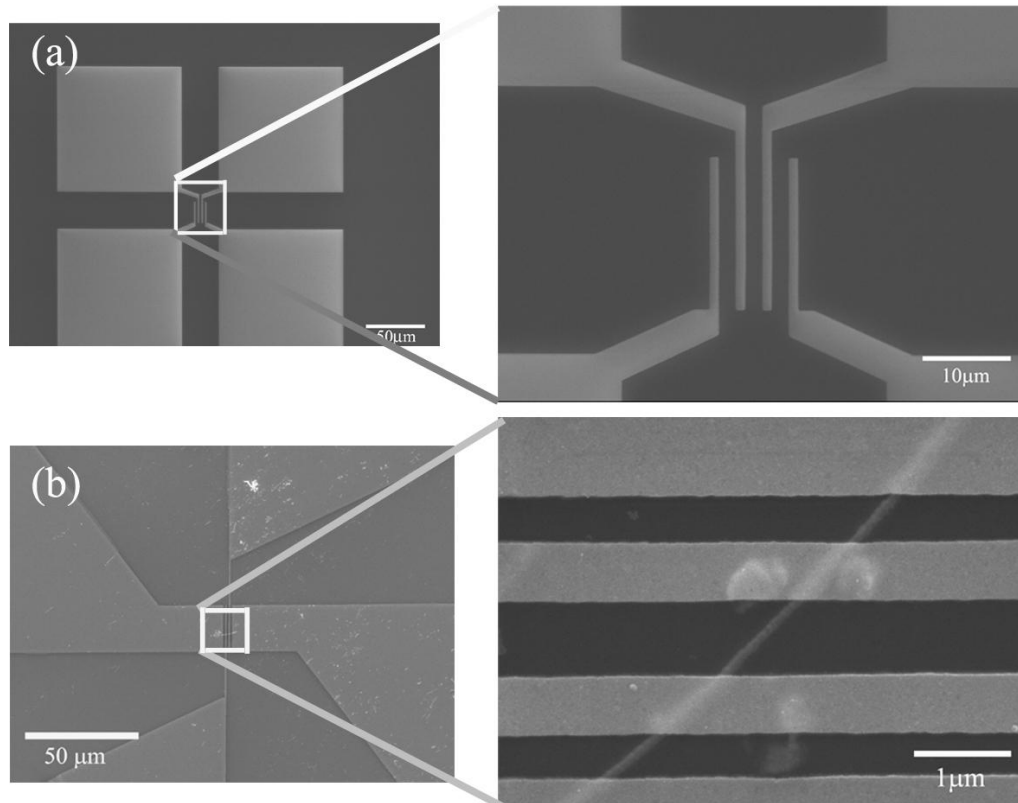


Figure A1 SEM images of four point contact pads fabricated by using E-beam lithography. (a) First designed pads where four legs are clearly patterned. (b) Secondly designed pads where single NW is successfully placed on the four legs.